

Robot-Assisted Endodontic Treatment Based on Force-Guided Alignment and File Feedrate Control

Yi-Chan Li

Advisor: Cheng-Wei Chen

Graduate Institute of Electronics Engineering

National Taiwan University

Taipei, Taiwan

June 2021

Abstract

Advancements in robot-assisted surgery invigorate the application of robotic technologies in dentistry. This thesis aims to develop a robotic system in assisting endodontic treatment procedures. Considering the workspace and the extreme precision in endodontic treatment, a six degrees of freedom robotic manipulator – DentiBot – forms the basis of the developed system. Due to the lack of visual feedback in endodontic treatment, the DentiBot is integrated with a force and torque sensor, whose measurements guide the robot's motion during surgical procedures. The most critical two factors causing the failures of root canal treatment, namely incomplete root preparation and instrument fracture, are addressed. First, force-guided alignment based on admittance control techniques is proposed to adjust the surgical path and compensate for the patient's movement in real-time. Second, file federate control is proposed to protect endodontic files from fracturing, particularly when the file gets stuck in the root canal. These two functions are combined to achieve high performance in the root preparation procedure. Experimental results have demonstrated the performance of force-guided alignment and file feedrate control. The feasibility of robot-assisted endodontic treatment is verified by the pre-clinical evaluation performed on acrylic root phantoms.

Keywords: *Endodontic treatment, Robot-assisted system, Admittance control, Force-guided alignment, File feedrate control, Instrument fracture*

Contents

Abstract	i
List of Figures	v
List of Tables	ix
1 Introduction	1
1.1 Motivation	1
1.2 Previous Work and Problem Definition	2
1.3 The Proposed Method	6
1.4 Main Contributions of the Thesis	7
2 State-of-the-Art	11
2.1 Surgical Robots Applied in Dentistry	11
2.2 Robot-Assisted Endodontic Treatment	15
3 Design and Analysis of the Dental Surgical Robot - DentiBot	21
3.1 Requirement and Specification	21
3.2 Design of the DentiBot	21
3.3 Kinematics Analysis	25
3.4 Tool-tip Coordinate	34
4 Force-Guided Robot Alignment	41
4.1 Problem Definition and the Proposed method	41

4.2	Integration of F/T sensor	43
4.3	Dragging Mode	51
4.4	Self-Alignment Mode	56
4.5	Parameter Selection	61
5	File Feedrate Control	65
5.1	Problem Definition and the Proposed Method	65
5.2	Inverse Rotation Control	69
5.3	Feedrate Control	72
5.4	Automated Endodontic Treatment	74
6	Experiment Results	79
6.1	Experimental Setup	79
6.2	Force-Guided Alignment	86
6.3	Pre-Clinical Evaluation	104
7	Conclusions and Future works	109
7.1	Conclusions	109
7.2	Discussion and Future Works	110
Apppedix		113
A	Forward Kinematics	113
B	Jacobian Matrix	114
Reference		119

List of Figures

1.1	The endodontic treatment procedure	3
2.1	Dental robot designed by the University of Hong Kong	12
2.2	Implant robot designed by Chosun university, Korea	13
2.3	Implant robot designed by Yokohama National University, Japan .	13
2.4	Commercial implant robot - YOMI (Neosis, Miami, Florida, USA)	14
2.5	Patient tracking system of YOMI	15
2.6	Project of micro robot for endodontic treatment proposed by professor Janet Dong	16
2.7	Dimension of the endodontic micro Robot	17
2.8	Endodontic micro robot with micro actuators, a tool change mechanism, and a hydraulic system	18
2.9	Z-axis actuator with tool change mechanism.	19
3.1	The DentiBot and an acyclic tooth model	22
3.2	Dental handpiece and modified handpiece composed of a servo motor, a coupler and the front part of dental handpiece	23
3.3	Coordinate definition of the DentiBot. Frame{0} to frame{6} represent each frame of axes of Meca500, frame{S} represents the frame of ATI-mini40 and frame{H} represents the frame of the handpiece tooltip frame.	25

3.4 Schematic diagram for tool center point (TCP). The translation vector ${}^6p_{H_{org}}$ denotes the origin position relative to the frame{6}.	35
3.5 Four points method. Align a fixed point with four different poses.	37
3.6 Schematic diagram for obtaining the tool vector.	38
3.7 Illustration of finding the rotation matrix with the tool vector	39
4.1 Data analysis of F/T sensor.	43
4.2 Control scheme. f_d denotes the desired forces and torques vector. f_s denotes the real value detected by F/T sensor and is also a forces and torques vector. \dot{x} denotes $[\dot{x}, \dot{y}, \dot{z}, \dot{\theta}_x, \dot{\theta}_y, \dot{\theta}_z]$. J_g denotes the geometric Jacobian matrix. $\dot{\theta}$ denotes $[\dot{\theta}_1, \dot{\theta}_2, \dot{\theta}_3, \dot{\theta}_4, \dot{\theta}_5, \dot{\theta}_6]$. θ denotes $[\theta_1, \theta_2, \theta_3, \theta_4, \theta_5, \theta_6]$	53
4.3 Illustration of changing reference frame from {S} to {T}. f and m respectively denote a force and a moment measured at point p.	58
4.4 Illustration of changing reference frame from {S} to {T}.	59
4.5 Control scheme. M , B , K are all diagonal positive definite matrices, whose diagonal indexes are respectively related to $x, y, z, \theta_x, \theta_y, \theta_z$. M , B are related to the inertial and damping respectively, and K is a proportional gain.	61
4.6 Reference point A in Dragging Mode. Reference point B and holding points G_1, G_2 in Self-Alignment Mode.	64
5.1 The illustration of an endodontic file	66

5.2	Endodontic files with different diameters	67
5.3	The prototype of DentiBot. A single z-axis manipulator with a modified handpiece	70
5.4	Motion planning of Inverse Rotation Control with the prototype of DentiBot.	71
5.5	Control scheme of Feedrate Control with the DentiBot.	73
5.6	Flow chart of Feedrate Control with the DentiBot. <i>f</i> represents force vector	74
5.7	Methods of Automated Endodontic Treatment	75
5.8	Algorithm for robot-assisted endodontic treatment	76
6.1	Communication protocol – EtherCAT. Master device is RT-target and slave devices are robot arm, F/T sensor and modified handpiece.	80
6.2	Graph user interface with LabVIEW 2018	80
6.3	Experimental setup with Dentibot, a motion capture system, and a Stewart platform	81
6.4	Flow charts for force-guided alignment experiment. The left and top figure is inserting without file rotation. The right and top figure is inserting with file rotation. The bottom figure is inserting with file rotation and file feedrate control.	87
6.5	Position command of Stewart platform for force-guided alignment experiment	88

6.6 Exp 1-1: The position of handpiece and root and their relative distance	91
6.7 Exp 1-2: The position of handpiece and root and their relative distance	92
6.8 Exp 1-3: The position of handpiece and root and their relative distance	93
6.9 Patient moving simulated by the Stewart platform	94
6.10 Exp 1-1: The force vs the velocity	96
6.11 Exp 1-1: The force vs the velocity	97
6.12 Exp 1-1: The force vs the velocity	98
6.13 Zoom-in of Force vs Velocity on Z-axis from 80th to 90th second .	99
6.14 Exp 1-2: The force vs the handpiece position	100
6.15 Exp 1-2: The force vs the handpiece position	101
6.16 Exp 1-2: The force vs the handpiece position	102
6.17 Algorithm for robot-assisted endodontic treatment	104
6.18 Acrylic root phantom used in operative technique practice	105
6.19 Exp 2: Roots before and after drilling for two times. T_{des} were set 40 in A,B,C and 50 in D,E,F	106

List of Tables

3.1	Denavit-Hartenberg parameters of Meca500	26
4.1	Comparison of arc-functions	50
4.2	Moving commands in Meca500	54
4.3	Parameters setting of Admittance control.	63
6.1	Specifications of the hardware and software environments	83
6.2	Technical specifications of the robot arm - meca500	84
6.3	Technical specifications of the F/T sensor - mini40	85
6.4	Parameters setting of admittance control in Experiment 1.	89
6.5	Results of pre-clinical evaluation	107

Chapter 1

Introduction

The robot-assisted system for endodontic treatment - DentiBot is presented in this thesis. The definition of a robot-assisted system in the thesis refers to be a dental assistant, which means we wish DentiBot could help dentists perform better clinical results and reduce the risks associated with free-hnad surgery. This chapter will give brief introductions of the endodontic treatment, previous work, problem definition, and the proposed method.

1.1 Motivation

A qualified dentist with a certification can operate an endodontic treatment. They accumulate their experience, thereby increasing the success rate of surgery. With enough clinical experience, the dentist can acquire an endodontist license. According to statistics from the Ministry of Health and Welfare, R.O.C. (Taiwan) [1], the number of dentists in Taiwan is 15,178. However, according to The Academy of Endodontology, R.O.C. (Taiwan) [2], there are only 238 dentists to acquire an endodontist license. Thus, performing an endodontic treatment requires the dentist's self knowledge and expertise of endodontics. The performance of endodontic treatment depends on a dentist's long-term clinician experience and

skill.

Besides, root canal treatment is a tedious and time-consuming surgery for a dentist due to different intricate conditions of each tooth. A patient who suffered from an infected tooth spends countless hours see a dentist. Endodontic treatment takes at least two to three rounds of treatments, even more than two months in the worst case.

Therefore, our team looks forward to designing a robot-assisted system to accomplish a root canal treatment. With the robot, we wish it can reduce times for entire treatment, increase the success rate of root canal treatment for dentists, and provide patients safer surgery.

1.2 Previous Work and Problem Definition

First, we introduce the endodontic treatment and its detailed procedure.

Endodontic treatment, also known as root canal treatment and nerve extraction, is performed to cure an infected tooth. The main procedure of endodontic treatment is divided into three parts - Opening, Cleaning, and Filling shown in Figure 1.1.

An infected tooth arises from periodontal disease, attrition, trauma, or decay. Once the dental pulp is infected, it causes an irreversible inflammation and lets patients confront a root canal treatment. Figure 1.1 shows an infected tooth and its dental pulp, which consisted of blood vessels, nerves, connective tissues, and lymphatics. In the "Opening" step, an experienced dentist drills the crown of the infected tooth to remove the dentin and expose the infected pulp inside the

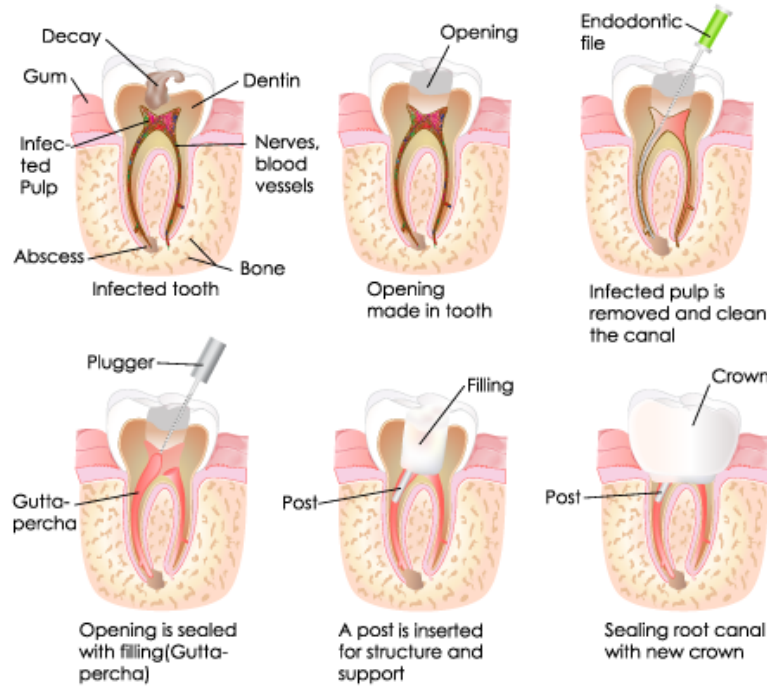


Figure 1.1: The endodontic treatment procedure [3]

canal to the air. Next, in the "Cleaning" step, the dentist uses an endodontic file, a superelastic root reamer, to remove the infected pulp. It is necessary to ensure that there is no remained infected pulp. Then, in the "Filling" step, the dentist uses a dental plugger to fill the empty root canal with Gutta-percha, a plastic substance. "Filling" can prevent cross-infection between root canals because the cured tooth remains many invisible and inaccessible pulp tissue. Finally, the dentist seals the root canal with a new crown to protect cured root canal.

As stated above, "Cleaning" is of paramount importance in a whole treatment because cleaning improperly will result in pulp necrosis, apical abscess, periodontal ligament inflammation, or even cellulitis. If there are many remained infected pulp

after root canal treatment, the surgery should be operated on again. The "Cleaning" procedure is a big challenge in and of itself. Therefore, we should figure out how to enable the robot to assist dentists and perform the root canal treatment.

Previous Work

There are more and more robots which applied to specific surgery. In the dental field, the majority of robotic applications are in implant surgery. The researchers in Chosun University built a dental implant robot [4], a remote center of motion (RCM) mechanism. Li, J. et al. designed a robotic system using a soft bracing technique to drill teeth [5]. Also, there is the first commercial implant robot, YOMI, developed by Neosis [6]. However, there was one and only one robot for the endodontic treatment. The domestic researcher Janet Dong and his team proposed a microrobot performing root canal treatment with the assistance of a 3D computer model system [7]. However, the study using 3D model belongs to pre-operation. If a patient or an image error causes a movement, it will not be easy to reschedule the motion planning because the root canal in a tooth is unseen by a camera from any angle. Besides, once an endodontic file enters into a root canal, it is hard to obtain the tool tip position due to its flexibility. The endodontic file will bend when it bears a force. Once we lose the position of the endodontic file, it may lead to perforation, overpreparation, and underpreparation. Therefore, a problem reveals - how the robot know the path of a root canal without visual feedback?

On the other hand, instrument fracture is the other concern during the therapy.

If an endodontic file suffered excessive usage, it would unpredictably break. The leading causes of fractured files are torsional fracture and flexural fatigue, which account for 55.7% and 44.3% separately [8]. Removal of broken files is technically tricky, so it is essential to reduce the probability of the instrument fracture. Therefore, our robot should prevent the instrument fracture by some detection. In addition, the root canal treatment also requires repeatedly drilling to clean the canal thoroughly and motion planning to avoid perforation. This repetitive action of root canal treatment is tedious and time-consuming. Therefore, we decide to design an automatic endodontic robot. It can improve time efficiency and prevent instrument fracture in endodontic treatment.

Problem Definition

To sum up, there are three main problems.

1. How to assist dentists to perform the root canal treatment including motion planning, especially in the second procedure - cleaning?
2. How to overcome the problem that the root canal cannot be visually observed, and how to clean well in any complex conditions?
3. How to protect the endodontic file from fracturing during the surgery?

1.3 The Proposed Method

To assist dentists in accomplishing an endodontic treatment, a robot-assisted system – DentiBot is developed to provide more precise and safer surgery. DentiBot consists of a 6-DoF robot arm, a 1-DoF modified end effector, and a 6-DoF force/torque sensor. The proposed 7-DoF robotic manipulator enables to manifest various motions such as drilling and reciprocation. Therefore, DentiBot can assist dentists in performing the second procedure – Cleaning.

Due to the lack of visual feedback in endodontic treatment, force-guided alignment based on admittance control techniques is proposed to guide the robot's motion. Force-guided alignment enables our system to adjust the surgical path and compensate for the patient's movement in real-time. That means the Dentibot could align the root canal path by force feedback without vision feedback. Hence, force-guided alignment could solve the first failure factor – incomplete root preparation.

To protect endodontic files from fracturing particularly when the file gets stuck in the root canal. Inverse rotation control and file feedrate control are proposed. These two functions are both based on torque control. Inverse rotation control could remove debris and prevent files from getting stuck. File feedrate control utilizes the measured file torque to regulate the file feedrate. These two proposed approaches are combined to protect endodontic files and achieve high performance in the root preparation procedure.

A new idea that combines all proposed functions – force guided alignment,

inverse rotation control, and file feedrate control will be presented.

1.4 Main Contributions of the Thesis

To build an appropriate robot system for endodontic treatment, it is necessary to contemplate requirements and specifications comprehensively from technical and clinical perspectives. There are four subjects of the proposed robot-assisted project.

Prospect

1. Dentist could move the DentiBot to the infected tooth.
2. The DentiBot could search all root canals of the infected tooth.
3. The DentiBot could do repetitive drilling and clean thoroughly.
4. The DentiBot continues drilling until detecting the apex of the root canal.

Main Contributions

The thesis is the beginning of the project and focus on the first and the third part of the project. In conclusion, there are three main contributions of the thesis.

1. Integrate a 6-DoF robotic manipulator with 6-DoF F/T sensor for performing endodontic treatment.
2. Develop a framework for robot alignment regarding the position and orientation of root canal.

3. Protect the endodontic file from fracturing by controlling file rotation speed.

Organization of the Thesis

In Chapter 2, The state-of-the-art of dental robots for implant placement and endodontic treatment are surveyed and summarized. Four implant robots including a commercial robot are reviewed and an endodontic robot is dissected.

Our proposed robot- DentiBot is highlighted in chapter 3. Technical solutions to system integration with a robot arm are presented. The kinematics of the robot arm is derived. Moreover, the problem of how to find the tool center point (TCP) and tool angle is explained.

Chapter 4 demonstrates how to solve the system integration problem when combining a robot arm and an F/T sensor. Gravity compensation and reference frame changing issues are clarified first. Moreover, admittance control based on F/T sensor is presented. Subsequently, Force-guided alignment approach is described.

The proposed approach for protecting an endodontic file from fracturing is shown in Chapter 5. File property is discussed and the methods for estimating torque are interpreted. Inverse rotation control and file feedrate control which are used to prevent instrument fracture are defined. Ultimately, the most important thing is that an algorithm for robot-assisted endodontic treatment is proposed.

Experiment results are shown and analyzed in Chapter 6. Technical and pre-clinical experiments are conducted. Force-guided alignment is confirmed by the first experiment and the proposed algorithm including all functions is proven by the second experiment. In the end, Chapter 7 makes a summary and lists future

work for this thesis.

Chapter 2

State-of-the-Art

To comprehensively contemplate requirements of an endodontic robot such as workspace, payload, clinical problems, works of literature in the dental field are involved. Recent literatures have revealed that researchers have seen the use of dental robot [9][10][11], Most largely, implant surgery is widely discussed[12][13]. In this chapter, the pieces of literature about dental robots for implant placement and endodontic treatment will be reviewed.

2.1 Surgical Robots Applied in Dentistry

Advancements in robot-assisted surgery invigorates researches on robotics in the dental field. However, the majority of robotic applications are in implant surgery.

The research team in Hong Kong designed a dental manipulator with tendon-sheath mechanism and bracing actuator [5]. The tendon-sheath mechanism drove the whole machine to move and provided flexible manipulations. The soft bracing actuator at the end effector held the handpiece stably due to its stiffness and satisfied the requirement of workspace in a patient mouth. The objective of this robotic system is to perform from operative caries removal, crown preparation, filling, to

Orthodontia. However, pre-clinical tasks had not been proven yet.

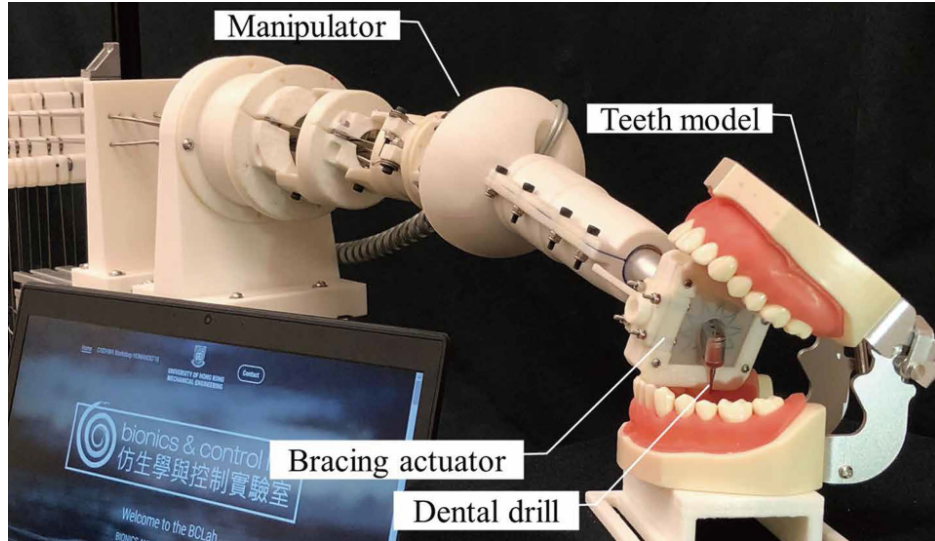


Figure 2.1: Dental robot designed by the University of Hong Kong [5].

G. Kim *et al.* proposed an implant robot based on a double parallelogram mechanism [4]. The manipulator is shown in Fig 2.2. With the double parallelogram mechanism, the entry point would be constrained at a fixed point and form a remote center of motion (RCM). Besides, a force and torque sensor was integrated to design an admittance type of cooperative manipulator. The manipulator used torque values in the x and y-axis to calibrate the bias caused by drilling. However, it seemed that the prototype of robot did not meet the requirement of dimension and workspace.

T. Iijima *et al.* proposed a master-slave dental system [14]. The serial-parallel hybrid mechanism provided remote center of motion (RCM) as shown in Fig 2.3. A reaction force observer (RFOB) was integrated to obtain force information. Acceleration based bilateral control was implemented to communicate master with

slave.

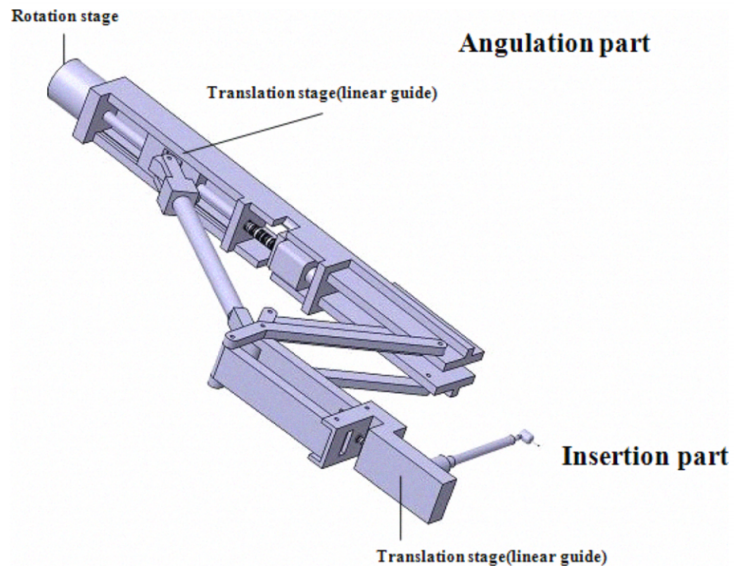


Figure 2.2: Implant robot designed by Chosun university, Korea [4].

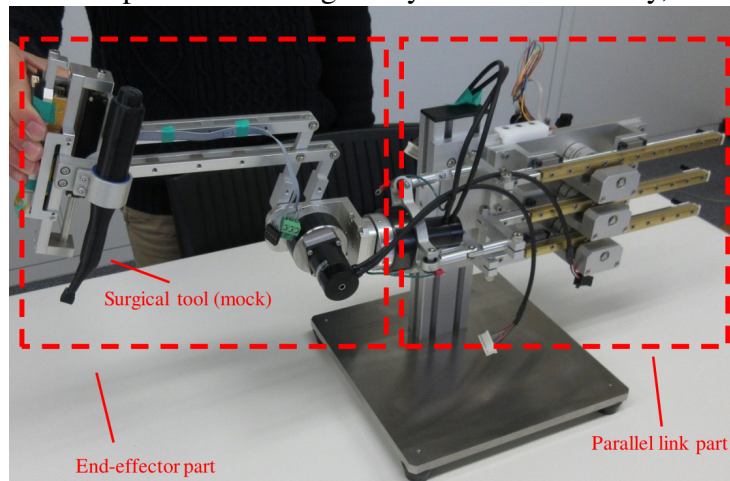


Figure 2.3: Implant robot designed by Yokohama National University, Japan [14].

There is a commercial robot, YOMI (Neosis, Miami, Florida, USA) [15][16], which is a robot-assisted system for minimally invasive implant surgery shown in Fig 2.4. YOMI provides precise physical and haptic guidance to perform implant

placement because it constrains the drilling position, direction, orientation, and depth. Dentists can design the surgical plan in advance with pre-planning software and adjust it intraoperatively. Undoubtedly it could increase the accuracy of drilling and decrease the surgery time. Also, once the tool approaches the danger zones such as nerves and sinus cavities, it will alert the dentist to take appropriate measures.



Figure 2.4: Commercial implant robot - YOMI (Neosis, Miami, Florida, USA)

An additional robot arm is connected to the intraoral splint which is mounted on patient mouth shown in Fig 2.5. It enables the robot to keep track of the position information [17] . If the patient moves, YOMI will detect it and alignment immediately to retain the accuracy of the drilling position. Furthermore, it visualizes a 3-D preoperative CT scan and real-time information on the screen to show the updated anatomical features such as drilling entry and bone quantity. YOMI has

received the clearance from FDA and has performed more than 2,700 surgeries in the USA. In the pandemic of Covid-19 in 2020, YOMI provided non-contact surgery between dentists and patients due to its automatic robotic system.



Figure 2.5: Patient tracking system of YOMI[6][17].

2.2 Robot-Assisted Endodontic Treatment

Endodontic treatment requires a higher precision and accuracy than implant placement. There was a domestic team dedicating to develop an endodontic

robot. In Intelligent Micro Robot Development for Minimum Invasive Endodontic Treatment [7][18][19], their team proposed a complete project, which involves whole endodontic treatment including "Opening", "Cleaning", and "Filling".

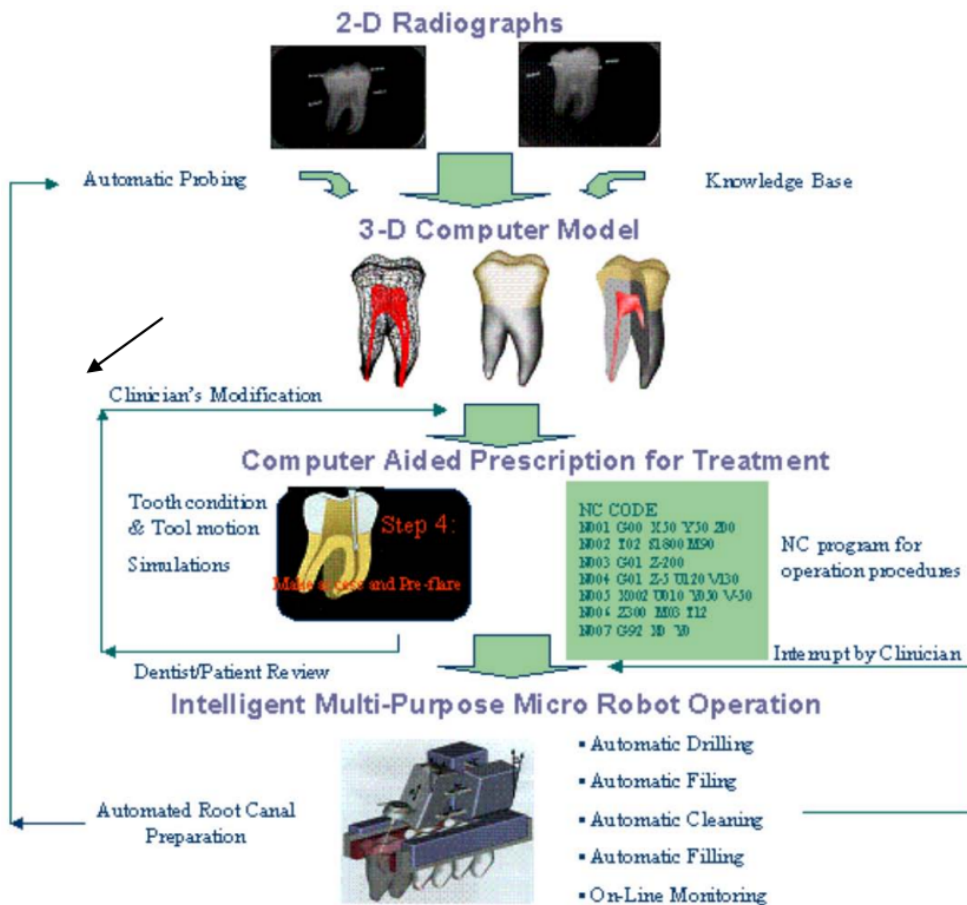


Figure 2.6: Project of micro robot for endodontic treatment proposed by professor Janet Dong [18]

The aim of this project was taken apart of several parts as shown in Fig 2.6.

Before starting surgery, it utilized a 2-D X-ray image to build a 3-D computational model and designed the corresponding surgical path by computer-aided treatment procedure planning which is widely used in industry. Intraoperatively a micro-

machine with a tool change mechanism was built to drill and fill. Then, an ultrasonic cleaning tool was interfaced to remove the cutting chips and pulps. However, the study using a 2-D X-ray image to build a 3-D model belongs to pre-operation. Any accident during surgery would destroy the ideal pre-planned path.

Also, a micro robot was developed to perform root canal treatment. It was small enough to be mounted on several teeth within a mouth as shown in Fig 2.7. Therefore, it reduced the patient's inconvenience because it allowed the patient to close their mouth during the surgery.



Figure 2.7: Dimension of the endodontic micro Robot [7]

A multi-purpose micro-machine was designed for automatic endodontic treatment as shown in Fig 2.8. A parallel bracket was installed on the teeth and the micro-machine was mounted on it. There were three radiopaque reference points inside the bracket. The patient with brackets was taken CT scan, and then three radiopaque points were obtained. With three points, a reference frame was built.

Therefore, The machine mounted on bracket would recognize the infected tooth.

The micro-machine had 6-DoF including five axes and a drilling tool, they were driven by micro actuators.

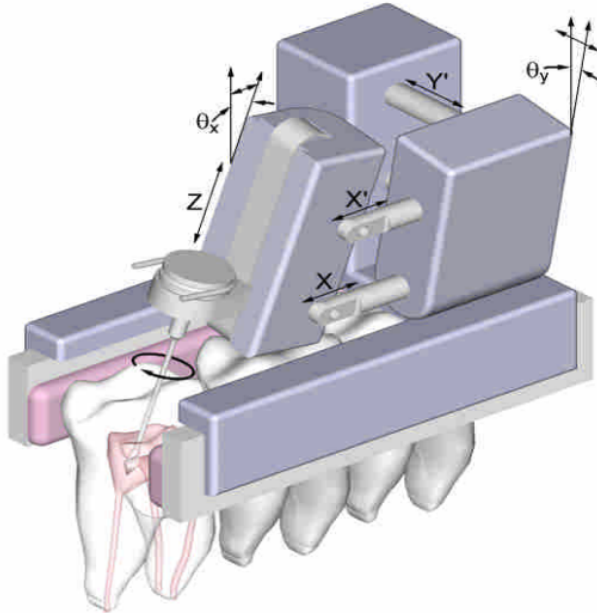


Figure 2.8: Endodontic micro robot with micro actuators and a hydraulic actuator

[7]

A tool change mechanism was illustrated in Fig 2.9. Because there were several procedures during surgery and different tools were used in different phase. If the machine can hold all types of tools without calibration, the surgery time would decrease dramatically. Moreover, a hydraulic system was integrated to provide enough drilling force for "Opening" procedure.

However, despite that using 2-D or 3-D image is a appropriate approach to design a surgical path, it belongs to pre-operation. There are many factors to

disrupt the surgical path such as uncertain tooth condition and image error. It is not easy to reschedule the motion planning because the root canal in a tooth is unseen by a camera from any angle. Besides, once an endodontic file enters into a root canal, it is hard to obtain the tool tip position due to its flexibility.

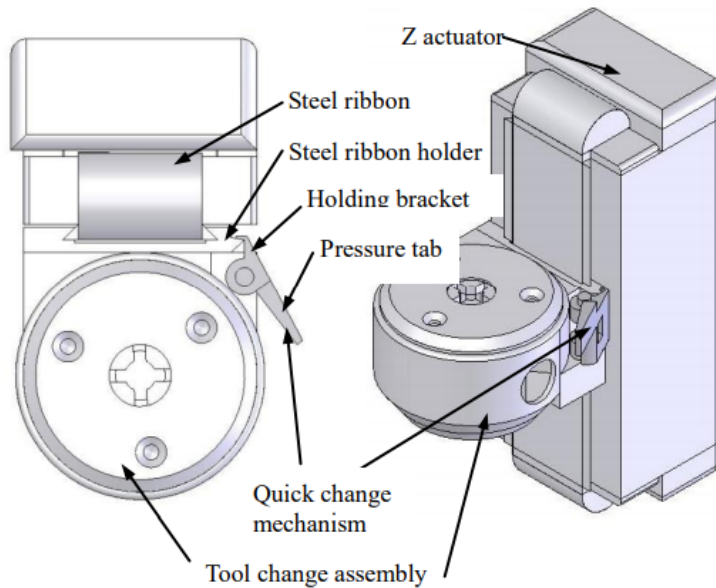


Figure 2.9: Z-axis actuator with tool change mechanism. [19]

Chapter 3

Design and Analysis of the Dental Surgical Robot - DentiBot

3.1 Requirement and Specification

The dental surgical robot should enable dentists to perform delicate and complicated surgery operations because the average diameter of a root canal is $0.28(\pm 0.08)$ mm [20]. Therefore, our system should have a high resolution of movement. Next, an appropriate workspace is required. In dental anatomy, teeth are located on the maxillary (lower jaw) and the mandibular (upper jaw). To perform surgery with both sides, we should rotate the end effector at least 180 degrees. Also, there is a previous research, which shows the average range of maximum mouth opening is $50.3 \text{ mm} \pm 6.26 \text{ mm}$ [21]. Hence, the end effector of our system should be less than this range.

3.2 Design of the DentiBot

As discussed in the previous section, we decide to build a system composed of a robot arm, an F/T sensor, and a modified handpiece. Why choosing a robot arm

and an F/T sensor is because we want to mimic the dentist's clinical behaviour. Due to the 6-DOF robot arm, the DentiBot can achieve the action with less hardware restriction. The DentiBot can easily move to almost desired positions and rotate more than 180 degrees to drill tooth in both sides of mouth. Also, with the 6-DoF F/T sensor, the real-time force and torque feedbacks are obtained and serve as a haptic feedback. The DentiBot can take reaction with the F/T sensor such as a dentist touch and sense something in the surgery and do the corresponding reaction. Besides, by modifying the existing handpiece, which is a handheld dental electric device, there is no doubt that the workspace and dimension in the mouth are satisfied. Also, there are two adapters designed to assemble these devices.

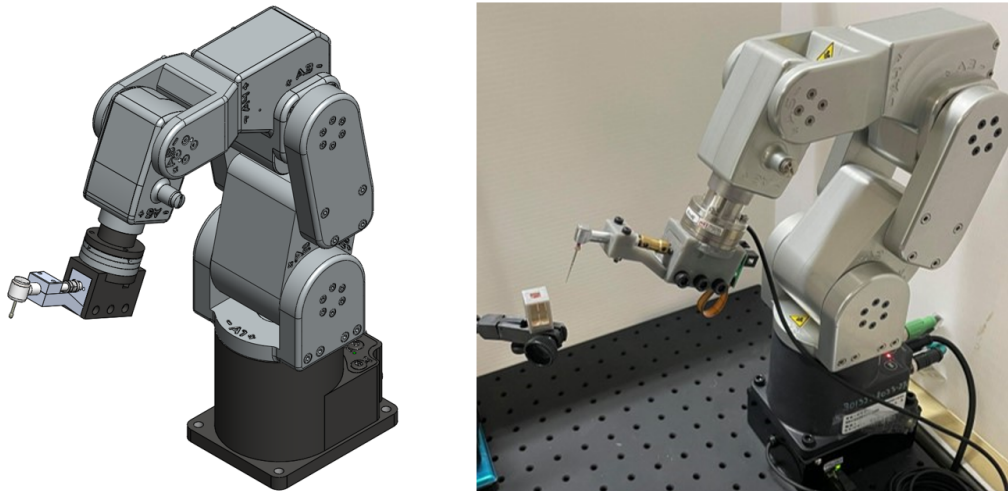


Figure 3.1: The DentiBot and an acyclic tooth model

To meet the requirement of workspace and dimension, we have to select appropriate devices according to those requirements. As shown in Fig 3.1, We choose Meca500 manufactured by Mecademic Inc. as our 6-DOF robot arm [22]

. Its feature is high repeatability (precision: 5 μm), and it is equipped with zero-backlash speed reducers. In addition, it is compact and portable for laboratory investigation. Second, Mini40 manufactured by ATI Inc. is the corresponding F/T sensor with three force and three torque detections [23]. As for the end effector, we modify an existing dental handpiece that equips a file exchange mechanism shown in Fig 3.2.

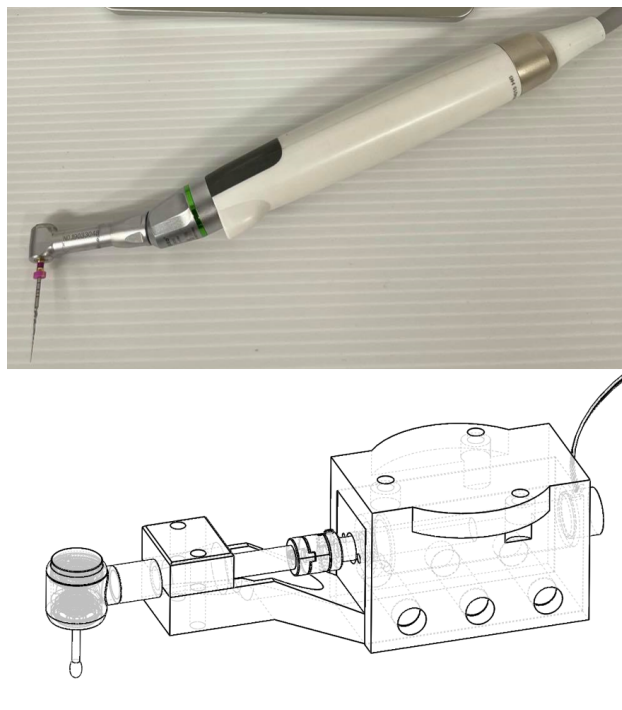


Figure 3.2: Dental handpiece and modified handpiece composed of a servo motor, a coupler and the front part of dental handpiece

A coupler connects the existing handpiece and a servo motor so that the rotation of endodontic file is driven by the servo motor. There is a concern about assembly error because the coupler cannot maintain the motor and the existing hadnpiece

in a straight line. The modified handpiece with a motor total weighs around 139 grams including the adapter used to assemble the F/T sensor and the handpiece. The weight of the modified handpiece is acceptable for the overloads of the F/T sensor and the robot arm.

In conclusion, DentiBot totally has seven degrees of freedom. Six degree of freedom come from Meca500, and the other is from the motor inside our modified handpiece. The rotation of the root canal file is driven by a servo motor, whose maximum rotation speed is around 200 rpm. The maximum rotation speed - 200 rpm is lower than the typical standard for endodontic treatment - $300 \sim 600$ rpm. However, the clinical outcome of our proposed algorithm with 200 rpm is acceptable. It will be proven in Chapter 6. If needed, the rotation speed can be more faster by changing a higher quality motor.

3.3 Kinematics Analysis

The purpose of this section and section 3.4 is to serve as a tutorial and provide some imperative approaches when combining a robot arm and an end effector. The forward and inverse kinematics are evaluated in section 3.3 and the Jacobian matrix is derived in section 3.3.

Coordinate Definition

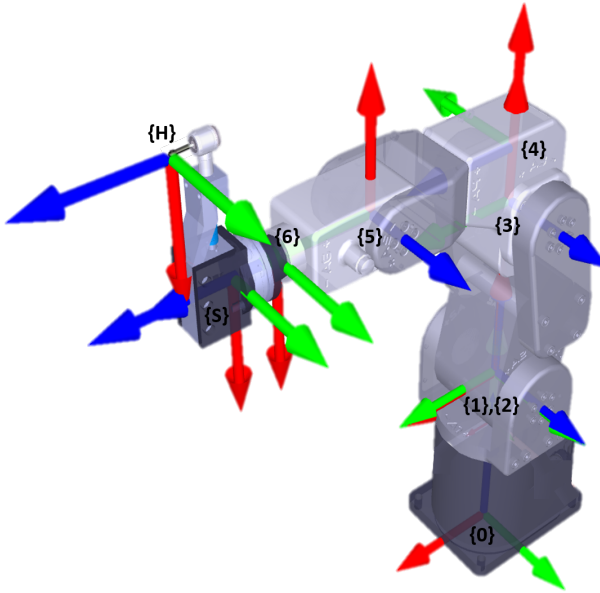


Figure 3.3: Coordinate definition of the DentiBot. Frame{0} to frame{6} represent each frame of axes of Meca500, frame{S} represents the frame of ATI-mini40 and frame{H} represents the frame of the handpiece tooltip frame.

Table 3.1: Denavit-Hartenberg parameters of Meca500

i (link number)	α_{i-1} (deg)	a_{i-1} (mm)	θ_i (deg)	d_i (mm)
1	0	0	θ_1	135
2	-90	0	$\theta_2 - 90$	0
3	0	135	θ_3	0
4	-90	38	θ_4	120
5	90	0	θ_5	0
6	-90	0	$\theta_6 + 180$	70

Forward and Inverse Kinematics

Denavit-Hartenberg parameters are shown as Table 3.1. Then, the forward kinematics of Meca500 is derived as

$${}^0\mathbf{T} = {}^0\mathbf{T} \cdot {}^1\mathbf{T} \cdot {}^2\mathbf{T} \cdot {}^3\mathbf{T} \cdot {}^4\mathbf{T} \cdot {}^5\mathbf{T} \cdot {}^6\mathbf{T} = \begin{bmatrix} {}^0\mathbf{R} & {}^0\mathbf{p}_{6\text{org}} \\ 0 & 1 \end{bmatrix} \quad (3.1)$$

where ${}^0\mathbf{R}$ is the rotation matrix from frame{6} to frame{0}, ${}^0\mathbf{p}_{6\text{org}}$ is the origin of the frame{6} observed from frame{0}. All detailed indexes of ${}^0\mathbf{T}$ are shown in Appendix 7.2

Incidentally, there is an alternative to calculate the transformation matrix ${}^0\mathbf{T}$ in real-time. We can use command "GetPose" to obtain $(x, y, z, \alpha, \beta, \gamma)$. (x, y, z) is exactly ${}^0\mathbf{p}_{6\text{org}}$ and (α, β, γ) are Euler angles. Hence, we can use these information

to derive the following equation.

$$\begin{aligned}
 {}_6^0\mathbf{T} &= \begin{bmatrix} & & & x \\ \mathbf{R}_x(\alpha) \cdot \mathbf{R}_y(\beta) \cdot \mathbf{R}_z(\gamma) & & & y \\ & & & z \\ 0 & & & 1 \end{bmatrix} \\
 &= \begin{bmatrix} c_\beta c_\gamma & -c_\beta s_\gamma & s_\beta & x \\ c_\alpha s_\gamma + s_\alpha s_\beta c_\gamma & c_\alpha c_\gamma - s_\alpha s_\beta s_\gamma & -s_\alpha c_\beta & y \\ s_\alpha s_\gamma - c_\alpha s_\beta c_\gamma & s_\alpha c_\gamma + c_\alpha s_\beta s_\gamma & c_\alpha c_\beta & z \\ 0 & 0 & 0 & 1 \end{bmatrix} \tag{3.2}
 \end{aligned}$$

where C_\star, S_\star denote $\cos(\star), \sin(\star)$; α, β, γ are in representation of Euler angle.

Jacobian matrix

Here we evaluate geometric Jacobian based on frame{0}, geometric Jacobian based on frame{6} and analytical Jacobian.

First, we should clarify the difference between geometric Jacobian and analytical Jacobian. They both use the same linear velocity but different angular velocity. The angular velocity which geometric Jacobian applies is relevant to the axis angles $(\theta_x, \theta_y, \theta_z)$. In contrast, the angular velocity which analytical Jacobian contemplates is related to the orientation (α, β, γ) of the end effector. Therefore, the geometric Jacobian has a clear physical meaning due to the differential $(\theta_x, \theta_y, \theta_z)$ is the angular velocity. Besides, because the geometric Jacobian can be considered in different frames, it is important to clearly understand and familiar with which

frame is our option.

Geometric Jacobian Based on Frame{0}

Before examining the geometric Jacobian matrix, it will be necessary to find the relationship between the position and joints' angles and the relationship between the axis angle and the joints' angles.

Based on the translation matrix in Equation 3.1, we obtain the relationship between the position and joints' angles.

$${}^0\mathbf{p}_{6\text{org}} = \begin{bmatrix} x \\ y \\ z \end{bmatrix} = \begin{bmatrix} x(\theta_1, \theta_2, \dots, \theta_6) \\ y(\theta_1, \theta_2, \dots, \theta_6) \\ z(\theta_1, \theta_2, \dots, \theta_6) \end{bmatrix} \quad (3.3)$$

Moreover, the relationship between the axis angle and joints' angles is

$$\begin{bmatrix} \theta_x \\ \theta_y \\ \theta_z \end{bmatrix} = {}^1\mathbf{R} \begin{bmatrix} 0 \\ 0 \\ \theta_1 \end{bmatrix} + {}^2\mathbf{R} \begin{bmatrix} 0 \\ 0 \\ \theta_2 \end{bmatrix} + {}^3\mathbf{R} \begin{bmatrix} 0 \\ 0 \\ \theta_3 \end{bmatrix} + {}^4\mathbf{R} \begin{bmatrix} 0 \\ 0 \\ \theta_4 \end{bmatrix} + {}^5\mathbf{R} \begin{bmatrix} 0 \\ 0 \\ \theta_5 \end{bmatrix} + {}^6\mathbf{R} \begin{bmatrix} 0 \\ 0 \\ \theta_6 \end{bmatrix} \quad (3.4)$$

Therefore, Jacobian matrices can be obtained by differentiating Equation 3.3 and

3.4.

$$\left\{ \begin{array}{l} \mathbf{v} = \begin{bmatrix} \dot{x} \\ \dot{y} \\ \dot{z} \end{bmatrix} = \mathbf{J}_{\text{gv}} \cdot \dot{\mathbf{q}} \\ \mathbf{w} = \begin{bmatrix} \dot{\theta}_x \\ \dot{\theta}_y \\ \dot{\theta}_z \end{bmatrix} = \mathbf{J}_{\text{gw}} \cdot \dot{\mathbf{q}} \end{array} \right. \quad (3.5)$$

where

$$\mathbf{J}_{\text{gv}} = \begin{bmatrix} \frac{\partial x}{\partial \theta_1} & \frac{\partial x}{\partial \theta_2} & \dots & \frac{\partial x}{\partial \theta_6} \\ \frac{\partial y}{\partial \theta_1} & \frac{\partial y}{\partial \theta_2} & \dots & \frac{\partial y}{\partial \theta_6} \\ \frac{\partial z}{\partial \theta_1} & \frac{\partial z}{\partial \theta_2} & \dots & \frac{\partial z}{\partial \theta_6} \end{bmatrix}, \quad \mathbf{J}_{\text{gw}} = \begin{bmatrix} \frac{\partial \theta_x}{\partial \theta_1} & \frac{\partial \theta_x}{\partial \theta_2} & \dots & \frac{\partial \theta_x}{\partial \theta_6} \\ \frac{\partial \theta_y}{\partial \theta_1} & \frac{\partial \theta_y}{\partial \theta_2} & \dots & \frac{\partial \theta_y}{\partial \theta_6} \\ \frac{\partial \theta_z}{\partial \theta_1} & \frac{\partial \theta_z}{\partial \theta_2} & \dots & \frac{\partial \theta_z}{\partial \theta_6} \end{bmatrix}, \quad \dot{\mathbf{q}} = \begin{bmatrix} \dot{\theta}_1 \\ \dot{\theta}_2 \\ \dot{\theta}_3 \\ \dot{\theta}_4 \\ \dot{\theta}_5 \\ \dot{\theta}_6 \end{bmatrix}$$

As a result, the geometric Jacobian matrix based on frame 0 ${}^0\mathbf{J}_g$ is derived as

$$\left\{ \begin{array}{l} \dot{\mathbf{x}} = {}^0\mathbf{J}_g \cdot \dot{\mathbf{q}} \\ \dot{\mathbf{q}} = {}^0\mathbf{J}_g^{-1} \cdot \dot{\mathbf{x}} \end{array} \right. \quad (3.6)$$

where

$$\dot{\mathbf{x}} = \begin{bmatrix} \dot{x} \\ \dot{y} \\ \dot{z} \\ \dot{\theta}_x \\ \dot{\theta}_y \\ \dot{\theta}_z \end{bmatrix}_{\{0\}}, \quad \dot{\mathbf{q}} = \begin{bmatrix} \dot{\theta}_1 \\ \dot{\theta}_2 \\ \dot{\theta}_3 \\ \dot{\theta}_4 \\ \dot{\theta}_5 \\ \dot{\theta}_6 \end{bmatrix}$$

By extension, in terms of the Jacobian matrix, the property between joint torque and force can be derived.

$$\boldsymbol{\tau} = {}^0\mathbf{J}_g^\top \cdot \mathbf{f} \Leftrightarrow \begin{bmatrix} \tau_{\theta_1} \\ \tau_{\theta_2} \\ \tau_{\theta_3} \\ \tau_{\theta_4} \\ \tau_{\theta_5} \\ \tau_{\theta_6} \end{bmatrix} = {}^0\mathbf{J}_g^\top \cdot \begin{bmatrix} f_x \\ f_y \\ f_z \\ \tau_x \\ \tau_y \\ \tau_z \end{bmatrix} \quad (3.7)$$

where $\boldsymbol{\tau}$ is the vector of joints' torques and \mathbf{f} is the vector composed of inertial forces and torques of the robot arm.

Geometric Jacobian Based on Frame{6}

Why we need geometric Jacobian based on frame{6} is that in section 4.3 we will apply admittance control and it will use F/T sensor mounted on frame{6}

instead of frame $\{0\}$ to detect forces and torques. To start with Equation 3.6

$$\begin{bmatrix} \dot{x} \\ \dot{y} \\ \dot{z} \\ \dot{\theta}_x \\ \dot{\theta}_y \\ \dot{\theta}_z \end{bmatrix}_{\{0\}} = {}^0\mathbf{J}_g \cdot \begin{bmatrix} \dot{\theta}_1 \\ \dot{\theta}_2 \\ \dot{\theta}_3 \\ \dot{\theta}_4 \\ \dot{\theta}_5 \\ \dot{\theta}_6 \end{bmatrix} \quad (3.8)$$

Then, left-multiply a matrix.

$$\begin{bmatrix} {}^0\mathbf{R} & 0_{3 \times 3} \\ 0_{3 \times 3} & {}^0\mathbf{R} \end{bmatrix} \begin{bmatrix} \dot{x} \\ \dot{y} \\ \dot{z} \\ \dot{\theta}_x \\ \dot{\theta}_y \\ \dot{\theta}_z \end{bmatrix}_{\{0\}} = \begin{bmatrix} {}^0\mathbf{R} & 0_{3 \times 3} \\ 0_{3 \times 3} & {}^0\mathbf{R} \end{bmatrix} {}^0\mathbf{J}_g \cdot \begin{bmatrix} \dot{\theta}_1 \\ \dot{\theta}_2 \\ \dot{\theta}_3 \\ \dot{\theta}_4 \\ \dot{\theta}_5 \\ \dot{\theta}_6 \end{bmatrix} \quad (3.9)$$

According to the transformation coordinate relationship between frame $\{0\}$ and frame $\{6\}$,

$$\begin{bmatrix} \dot{x} \\ \dot{y} \\ \dot{z} \\ \dot{\theta}_x \\ \dot{\theta}_y \\ \dot{\theta}_z \end{bmatrix}_{\{6\}} = \begin{bmatrix} {}^0\mathbf{R} & 0_{3 \times 3} \\ 0_{3 \times 3} & {}^0\mathbf{R} \end{bmatrix} \begin{bmatrix} \dot{x} \\ \dot{y} \\ \dot{z} \\ \dot{\theta}_x \\ \dot{\theta}_y \\ \dot{\theta}_z \end{bmatrix}_{\{0\}} \quad (3.10)$$

substitute it into Eq 3.9, we can observe an essential equation.

$${}^6\mathbf{J}_g = \begin{bmatrix} {}^0\mathbf{R} & 0_{3 \times 3} \\ 0_{3 \times 3} & {}^0\mathbf{R} \end{bmatrix} \cdot {}^0\mathbf{J}_g \quad (3.11)$$

Notably,

$$\begin{cases} \dot{\mathbf{x}} = {}^6\mathbf{J}_g \cdot \dot{\mathbf{q}} \\ \dot{\mathbf{q}} = {}^6\mathbf{J}_g^{-1} \cdot \dot{\mathbf{x}} \end{cases} \quad (3.12)$$

where

$$\dot{\mathbf{x}} = \begin{bmatrix} \dot{x} \\ \dot{y} \\ \dot{z} \\ \dot{\theta}_x \\ \dot{\theta}_y \\ \dot{\theta}_z \end{bmatrix}_{\{6\}}, \quad \dot{\mathbf{q}} = \begin{bmatrix} \dot{\theta}_1 \\ \dot{\theta}_2 \\ \dot{\theta}_3 \\ \dot{\theta}_4 \\ \dot{\theta}_5 \\ \dot{\theta}_6 \end{bmatrix}$$

Analytical Jacobian

The linear velocity of analytical Jacobian and geometric Jacobian is the same as shown in Eq 3.3. Nevertheless, as for angular velocity, analytical Jacobian takes the orientation (α, β, γ) of the end effector into consideration. First of all, we investigate the relationship between the axis angle and the orientation of the end

effector as following.

$$\begin{aligned} \begin{bmatrix} \theta_x \\ \theta_y \\ \theta_z \end{bmatrix} &= \begin{bmatrix} \alpha \\ 0 \\ 0 \end{bmatrix} + R_x(\alpha) \begin{bmatrix} 0 \\ \beta \\ 0 \end{bmatrix} + R_x(\alpha)R_y(\beta) \begin{bmatrix} 0 \\ 0 \\ \gamma \end{bmatrix} \\ &= \begin{bmatrix} 1 & 0 & S_\beta \\ 0 & C_\alpha & -S_\alpha C_\beta \\ 0 & S_\alpha & C_\alpha C_\beta \end{bmatrix} \begin{bmatrix} \alpha \\ \beta \\ \gamma \end{bmatrix} \end{aligned} \quad (3.13)$$

Then, utilize this generalized vector to get its Jacobian matrix \mathbf{J}_{we} .

$$\begin{bmatrix} \dot{\theta}_x \\ \dot{\theta}_y \\ \dot{\theta}_z \end{bmatrix} = \mathbf{J}_{\text{we}} \cdot \begin{bmatrix} \dot{\alpha} \\ \dot{\beta} \\ \dot{\gamma} \end{bmatrix} \quad (3.14)$$

where

$$\mathbf{J}_{\text{we}} = \begin{bmatrix} 1 & \gamma C_\beta & S_\beta \\ -\beta S_\alpha - \gamma C_\alpha C_\beta & C_\alpha + \gamma S_\alpha S_\beta & -C_\beta S_\alpha \\ \beta C_\alpha - \gamma C_\beta S_\alpha & S_\alpha - \gamma C_\alpha S_\beta & C_\alpha C_\beta \end{bmatrix}$$

Therefore,

$$\begin{bmatrix} \dot{x} \\ \dot{y} \\ \dot{z} \\ \dot{\theta}_x \\ \dot{\theta}_y \\ \dot{\theta}_z \end{bmatrix} = \begin{bmatrix} \mathbf{I}_{3 \times 3} & 0_{3 \times 3} \\ 0_{3 \times 3} & \mathbf{J}_{\text{we}} \end{bmatrix} \begin{bmatrix} \dot{x} \\ \dot{y} \\ \dot{z} \\ \dot{\alpha} \\ \dot{\beta} \\ \dot{\gamma} \end{bmatrix} \quad (3.15)$$

Finally, we obtain the relationship between geometric and analytical Jacobian.

$$\begin{cases} \mathbf{J}_g = \begin{bmatrix} \mathbf{I}_{3 \times 3} & \mathbf{0}_{3 \times 3} \\ \mathbf{0}_{3 \times 3} & \mathbf{J}_{we} \end{bmatrix} \mathbf{J}_a \\ \mathbf{J}_g = \begin{bmatrix} \mathbf{I}_{3 \times 3} & \mathbf{0}_{3 \times 3} \\ \mathbf{0}_{3 \times 3} & \mathbf{J}_{we}^{-1} \end{bmatrix} \mathbf{J}_a \end{cases} \quad (3.16)$$

3.4 Tool-tip Coordinate

So far, with the forward and inverse kinematics, the robot arm can translate and rotate around frame{6}. However, we do not see the origin of the frame{6} as an operating point. Because the F/T sensor and a detachable end effector will be both mounted on the wrist, the tooltip position is what we want. That means we should let the robot arm know how to translate and rotate in frame{T} instead of frame{6}. If we have translation and rotation information of the tooltip, there is an easy way to directly give the above information to the robot arm. SetTRF $(x, y, z, \alpha, \beta, \gamma)$ is the command of the robot arm, whose (x, y, z) is translation vector and (α, β, γ) is rotation vector in representation of Euler angle .

To obtain translation and rotation vector, we respectively introduce Tool Center Point in section 3.4 to find the translation vector and propose an approach in section 3.4 to find the rotation vector.

Translation Analysis - Tool Center Point

Tool Center Point (TCP) is a critical problem for robot arm control [24]. In the previous section, we have calculated the forward and inverse kinematics of the robot arm. By Calculating kinematics, we can keep track of the origin of the frame{6}, which is observed from the base frame. The robot arm has the capability to translate and rotate with the origin of the frame{6}. The overhead motions are like a remote center motion (RCM). We should find the position of the tooltip and make it be an RCM point. Nevertheless, it's inefficient to recalculate the transformation matrix via mechanism dimension when changing an end effector or a tool (endodontic file).

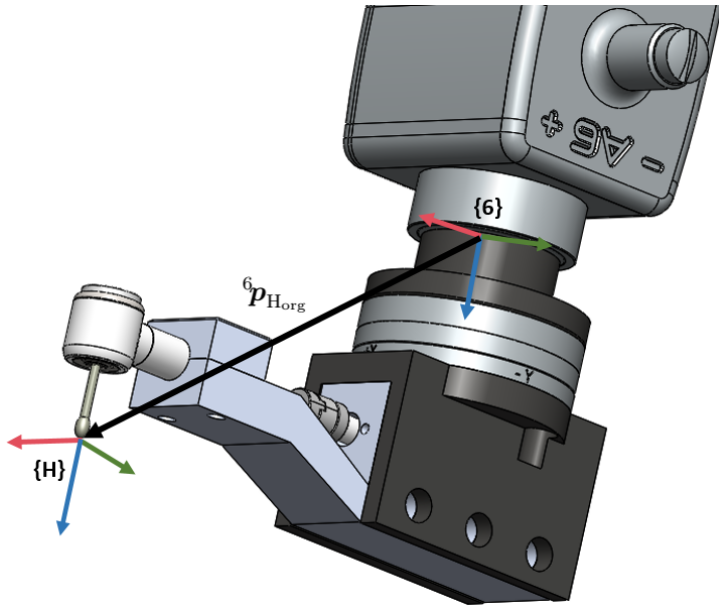


Figure 3.4: Schematic diagram for tool center point (TCP). The translation vector ${}^6p_{H_{org}}$ denotes the origin position relative to the frame{6}.

In order to overcome this problem, we interpret the four-points method to obtain the tooltip position, which is also the translation vector.

From Fig 3.3, the transformation matrix between the frame0 and frameH is evaluated as

$${}^0_H \mathbf{T} = {}^0_6 \mathbf{T} \cdot {}^6_H \mathbf{T} \quad (3.17)$$

and it can be rewritten as

$$\begin{aligned} \begin{bmatrix} {}^0_H \mathbf{R} & {}^0 \mathbf{p}_{H_{\text{org}}} \\ 0 & 1 \end{bmatrix} &= \begin{bmatrix} {}^0_6 \mathbf{R} & {}^0 \mathbf{p}_{6_{\text{org}}} \\ 0 & 1 \end{bmatrix} \begin{bmatrix} {}^6_H \mathbf{R} & {}^6 \mathbf{p}_{H_{\text{org}}} \\ 0 & 1 \end{bmatrix} \\ &= \begin{bmatrix} {}^0_6 \mathbf{R} \cdot {}^6_H \mathbf{R} & {}^0 \mathbf{p}_{6_{\text{org}}} + {}^0 \mathbf{p}_{H_{\text{org}}} \\ 0 & 1 \end{bmatrix} \end{aligned} \quad (3.18)$$

Consequently, we get a crucial equation:

$${}^0 \mathbf{p}_{H_{\text{org}}} = {}^0_6 \mathbf{R} \cdot {}^6 \mathbf{p}_{H_{\text{org}}} + {}^0 \mathbf{p}_{6_{\text{org}}} \quad (3.19)$$

Now, we move the tooltip to a fixed point with four different poses as shown in Fig 3.5, including position and orientation. Then, we will get four different rotation matrices and vectors in real-time.

$$\begin{aligned} {}^0 \mathbf{p}_{H_{\text{org}}} &= {}^0_F \mathbf{R}^1 \cdot {}^6 \mathbf{p}_{H_{\text{org}}} + {}^0 \mathbf{p}_{F_{\text{org}}}^1 \\ &= {}^0_F \mathbf{R}^2 \cdot {}^6 \mathbf{p}_{H_{\text{org}}} + {}^0 \mathbf{p}_{F_{\text{org}}}^2 \\ &= {}^0_F \mathbf{R}^3 \cdot {}^6 \mathbf{p}_{H_{\text{org}}} + {}^0 \mathbf{p}_{F_{\text{org}}}^3 \\ &= {}^0_F \mathbf{R}^4 \cdot {}^6 \mathbf{p}_{H_{\text{org}}} + {}^0 \mathbf{p}_{F_{\text{org}}}^4 \end{aligned} \quad (3.20)$$

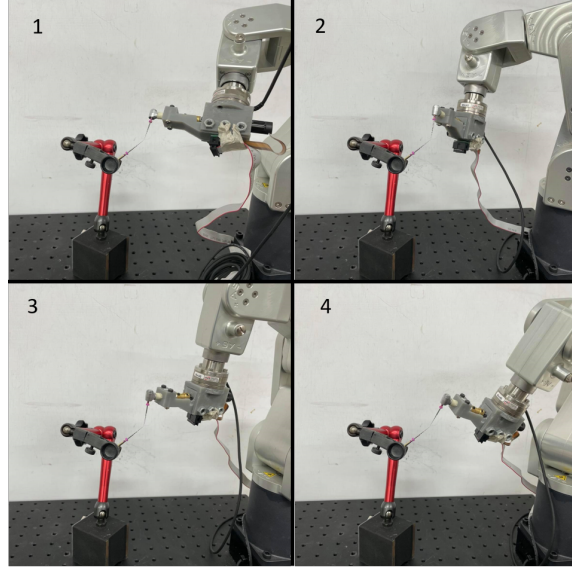


Figure 3.5: Four points method. Align a fixed point with four different poses.

In order to extract ${}^6\mathbf{p}_{H_{org}}$ from Equation 3.20, we subtract the second to forth equation from the first equation.

$$\begin{bmatrix} {}^0_6\mathbf{R}^1 - {}^0_6\mathbf{R}^2 \\ {}^0_6\mathbf{R}^1 - {}^0_6\mathbf{R}^3 \\ {}^0_6\mathbf{R}^1 - {}^0_6\mathbf{R}^4 \end{bmatrix} \cdot {}^6\mathbf{p}_{H_{org}} = \begin{bmatrix} {}^0\mathbf{p}_{6_{org}}^2 - {}^0\mathbf{p}_{6_{org}}^1 \\ {}^0\mathbf{p}_{6_{org}}^3 - {}^0\mathbf{p}_{6_{org}}^1 \\ {}^0\mathbf{p}_{6_{org}}^4 - {}^0\mathbf{p}_{6_{org}}^1 \end{bmatrix} \quad (3.21)$$

where we define

$$\mathbf{R} = \begin{bmatrix} {}^0_6\mathbf{R}^1 - {}^0_6\mathbf{R}^2 \\ {}^0_6\mathbf{R}^1 - {}^0_6\mathbf{R}^3 \\ {}^0_6\mathbf{R}^1 - {}^0_6\mathbf{R}^4 \end{bmatrix}_{9 \times 3}, \mathbf{p} = \begin{bmatrix} {}^0\mathbf{p}_{6_{org}}^2 - {}^0\mathbf{p}_{6_{org}}^1 \\ {}^0\mathbf{p}_{6_{org}}^3 - {}^0\mathbf{p}_{6_{org}}^1 \\ {}^0\mathbf{p}_{6_{org}}^4 - {}^0\mathbf{p}_{6_{org}}^1 \end{bmatrix}_{9 \times 1}$$

Therefore,

$$\begin{aligned} {}^6\mathbf{p}_{H_{org}} &= \mathbf{R}^\dagger \cdot \mathbf{p} \\ &= (\mathbf{R}^\top \mathbf{R})^{-1} \mathbf{R}^\top \cdot \mathbf{p} \end{aligned}$$

As a result, we can utilize the four-points method to obtain the translation vector.

Rotation Analysis

We are turning now to the discussion about the rotation vector. Above all, we have to find the vector of tool insertion direction t . We can obtain the translation vector from the origin of frame $\{6\}$ to the tooltip through the TCP method. Accordingly, we use two root canal files with different lengths and apply the TCP method to separately obtain two vectors illustrated as Fig 3.6. Hence,

$$\mathbf{t} = {}^6\mathbf{p}_{H_{org,long}} - {}^6\mathbf{p}_{H_{org,short}} \quad (3.22)$$

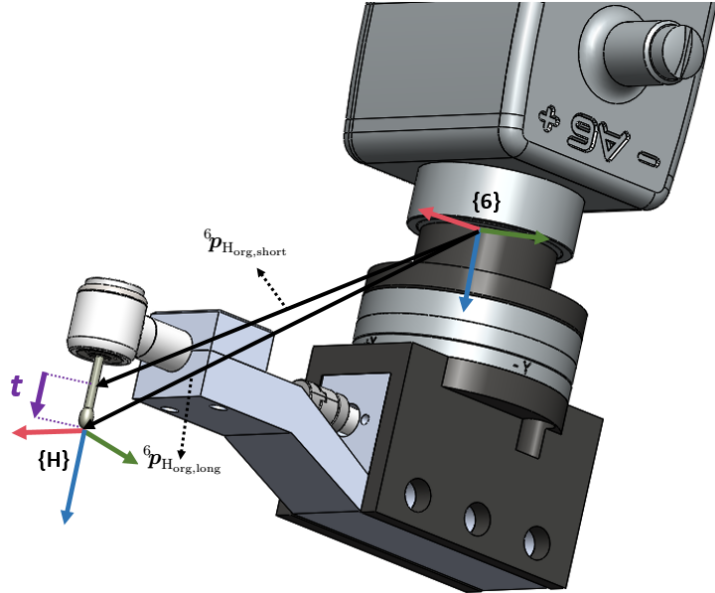


Figure 3.6: Schematic diagram for obtaining the tool vector.

For analyzing it easily, we depict it in Fig 3.7. Note that here we only discuss rotation, so we assume that we have done translation and matched the frame $\{S\}$

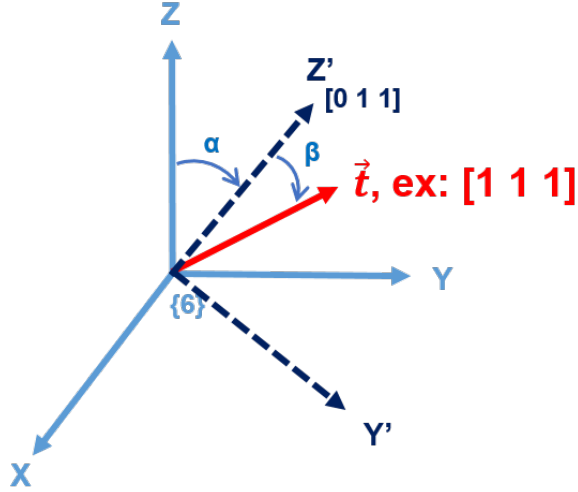


Figure 3.7: Illustration of finding the rotation matrix with the tool vector

with frame{6}. Because we hope to send a Z-axis command to achieve tool insertion, we should align the original Z-axis to the target vector. Nevertheless, Z-axis alignment without other restrictions will produce many solutions. We choose one of the solutions to align Z-axis to the target vector. According to the figure, we assume the target vector t is $[x, y, z]$, whose projection to yz-plane $\text{proj}_{(y-z)}t$ is $[0, y, z]$. Initially, we rotate α degree around X-axis to make original Z-axis align the projection $[0, y, z]$. Next, we rotate β degree around Y' axis and finally align the original Z-axis to the target vector $[1, 1, 1]$. The following equation

$${}^T_6 \mathbf{R} = \mathbf{R}_x(\alpha) \cdot \mathbf{R}_y(\beta) \quad (3.23)$$

where

$$\begin{aligned}\alpha &= -\text{sign}(t_y) \cdot \cos^{-1} \left(\frac{\hat{k} \cdot \text{proj}_{(y-z)} \mathbf{t}}{\|\hat{k}\| \cdot \|\text{proj}_{(y-z)} \mathbf{t}\|} \right) \\ \beta &= \text{sign}(t_x) \cdot \cos^{-1} \left(\frac{\mathbf{t} \cdot \text{proj}_{(y-z)} \mathbf{t}}{\|\mathbf{t}\| \cdot \|\text{proj}_{(y-z)} \mathbf{t}\|} \right)\end{aligned}\quad (3.24)$$

Assume $\mathbf{t} = [x, y, z]$,

$$\begin{aligned}\alpha &= -\text{sign}(y) \cdot \cos^{-1} \left(\frac{z^2}{\sqrt{y^2 + z^2}} \right) \text{ rad} \\ \beta &= \text{sign}(x) \cdot \cos^{-1} \left(\frac{y^2 + z^2}{\sqrt{x^2 + y^2 + z^2} \sqrt{x^2 + y^2 + z^2}} \right) \text{ rad}\end{aligned}\quad (3.25)$$

α and β are Euler angles, which meet the command demand.

In this section, we have demonstrated two key aspects of reference frame changing of the robot arm. It's easy to input the results of section 3.4 and section 3.4 via the command setTRF, the robot arm can recognize frame{T} and translate and orientate along with frame{T}. Having discussed how to combine a robot arm with an end effector, the next section addresses ways of combining an F/T sensor.

Chapter 4

Force-Guided Robot Alignment

This chapter follows from the previous issue about integration. We continue to demonstrate some technical solutions for system integration. On top of that, the Forces and Torques (F/T) sensor will be included to discuss. Therefore, you can see the chapter as an operating manual when you simultaneously own a robot arm, an F/T sensor, and an end effector. First of all, we will explain why we need to use the F/T sensor in our project in section 4.1. Furthermore, we will introduce how to compensate the gravity affection while moving the robot in section 4.2. Admittance control based on F/T sensor will be described in section 4.3. Coordinate transformation of F/T sensor will be interpreted in section 4.4. Last but not least, we will discuss affection of setting admittance control parameters in section 4.5.

4.1 Problem Definition and the Proposed method

In modern robot-assisted surgery, to simulate the eyes of doctors, image processing is often considered. With the image's information, the surgeon can obtain real-time data that humans can not observe clearly. Surgeons use the image process to do many things, such as tracking whether the patient is moving, positioning an

incision point, and navigating an insertion path. As for root canal treatment, the endodontist checks the number of root canals with computed tomography. Before starting to clean the pulp, the endodontist tries to insert root files into root canals. Then the endodontist takes the patient to have computed tomography(CT). CT scan can clearly show the tooth with the root files. With the preoperative image, the endodontist can check whether all root canals are all found and determine all root canals' lengths. However, the above image application is preoperative. The endodontist can only use the preoperative image to guess the direction of the insertion. The intraoperative image processing is absent due to the dimension restriction of a tooth. It is difficult to get a real-time image when the dentist inserts a root file into the opened tooth because it will obstacle the observation. Besides, the diameter of a root canal is 1 mm and is smaller than a root file. It is impossible to get the image from any shooting angle.

To solve the first problem - without image processing, we propose a method based on force-guided. We surveyed the peg-in-hole based on F/T sensor feedback [25] because the cleaning procedure is similar to it. On the other hand, we provide two operating modes - "Dragging Mode" and "Self-Alignment Mode" to cooperate with a dentist. In "Dragging Mode", we can hold the handpiece to the desired position and orientation. We hope to use this mode to let the dentist move the handpiece to the injured tooth. In "Self-Alignment Mode", the handpiece can automatically align the root canal direction even though there are many complicated conditions with different teeth.

4.2 Integration of F/T sensor

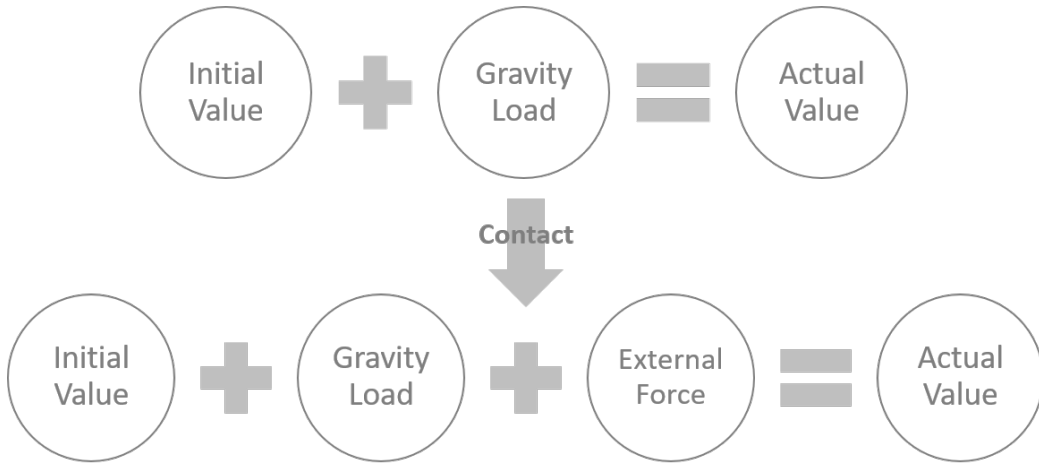


Figure 4.1: Data analysis of F/T sensor.

Gravity compensation is a critical technical issue when combining an F/T sensor with a robot arm and an end effector [26]. Fundamentally, we should receive stable data when a static F/T sensor bears the same load or force. Nevertheless, our F/T sensor is installed on the robot arm and move with the pose of the robot arm. On account of its mobility, the gravity of the end effector will significantly affect the actual value we received. Moreover, starting without resetting the F/T sensor to zero would lead to an initial value. If we could not analyze the actual value to an initial value and a gravity load, we would obtain an unstable actual value, not to mention the external force caused by contact force.

Therefore, we illustrate a method, which is to analyze the actual value of the F/T sensor to an initial value and gravity load in real-time. It's worth noting that

with this approach, we can get the installation angle between the F/T sensor and the robot arm, including assembly error, and we no longer need to reset the F/T sensor to zero every time.

The Centroid Position of End Effector

To start with the first equation in Figure 4.1,

$$\text{Initial value} + \text{Gravity Load} = \text{Actual Value}$$

$$\Rightarrow \begin{cases} \mathbf{f}_0 + \mathbf{f}_g = \mathbf{f} \\ \boldsymbol{\tau}_0 + \boldsymbol{\tau}_g = \boldsymbol{\tau} \end{cases} \Rightarrow \begin{cases} f_{0x} + f_{gx} = f_x \\ f_{0y} + f_{gy} = f_y \\ f_{0z} + f_{gz} = f_z \\ \tau_{0x} + \tau_{gx} = \tau_x \\ \tau_{0y} + \tau_{gy} = \tau_y \\ \tau_{0z} + \tau_{gz} = \tau_z \end{cases} \quad (4.1)$$

where \mathbf{f} and $\boldsymbol{\tau}$ are force and torque vector respectively.

And, by terms of moment arm formula,

$$\therefore \boldsymbol{\tau}_g = \mathbf{r} \times \mathbf{f}_g \quad (4.2)$$

where \mathbf{r} denotes the centroid position of the end effector in the sensor frame.

$$\begin{aligned} \therefore \boldsymbol{\tau} &= \boldsymbol{\tau}_0 + \boldsymbol{\tau}_g \\ &= \boldsymbol{\tau}_0 + \mathbf{r} \times \mathbf{f}_g \end{aligned} \quad (4.3)$$

Then, Substitute the first line of Equation 4.1 into the above equation, we will obtain

$$\boldsymbol{\tau} = \boldsymbol{\tau}_0 + \mathbf{p} \times (\mathbf{f} - \mathbf{f}_0) \quad (4.4)$$

, which could be extended as

$$\begin{cases} \tau_x = \tau_{0x} + (f_z - f_{0z}) \cdot y - (f_y - f_{0y}) \cdot z \\ \tau_y = \tau_{0y} + (f_x - f_{0x}) \cdot z - (f_z - f_{0z}) \cdot x \\ \tau_z = \tau_{0z} + (f_y - f_{0y}) \cdot x - (f_x - f_{0x}) \cdot y \end{cases} \quad (4.5)$$

and be overwritten as

$$\begin{bmatrix} \tau_x \\ \tau_y \\ \tau_z \end{bmatrix} = \begin{bmatrix} 0 & f_z & -f_y & 1 & 0 & 0 \\ -f_z & 0 & f_x & 0 & 1 & 0 \\ f_y & -f_x & 0 & 0 & 0 & 1 \end{bmatrix} \begin{bmatrix} x \\ y \\ z \\ k_1 \\ k_2 \\ k_3 \end{bmatrix} \quad (4.6)$$

where

$$\begin{cases} k_1 = \tau_{0x} - (f_{0z} \cdot y + f_{0y} \cdot z) \\ k_2 = \tau_{0y} - (f_{0x} \cdot z + f_{0z} \cdot x) \quad \text{are all constant} \\ k_3 = \tau_{0z} - (f_{0y} \cdot x + f_{0x} \cdot y) \end{cases} \quad (4.7)$$

With extracting $[x, y, z, k_1, k_2, k_3]$ in mind, we move the robot arm to n ($n \geq 3$) positions with different poses. By recording n torque vectors and corresponding n

force vectors from F/T sensor, we can expand Equation 4.6 as

$$\begin{bmatrix} \tau_x^1 \\ \tau_y^1 \\ \tau_z^1 \\ \tau_x^2 \\ \tau_y^2 \\ \tau_z^2 \\ \vdots \\ \tau_x^n \\ \tau_y^n \\ \tau_z^n \end{bmatrix} = \begin{bmatrix} 0 & f_z^1 & -f_y^1 & 1 & 0 & 0 \\ -f_z^1 & 0 & f_x^1 & 0 & 1 & 0 \\ f_y^1 & -f_x^1 & 0 & 0 & 0 & 1 \\ 0 & f_z^2 & -f_y^2 & 1 & 0 & 0 \\ -f_z^2 & 0 & f_x^2 & 0 & 1 & 0 \\ f_y^2 & -f_x^2 & 0 & 0 & 0 & 1 \\ \vdots & & \vdots & & & \\ 0 & f_z^3 & -f_y^3 & 1 & 0 & 0 \\ -f_z^3 & 0 & f_x^3 & 0 & 1 & 0 \\ f_y^3 & -f_x^3 & 0 & 0 & 0 & 1 \end{bmatrix} \begin{bmatrix} x \\ y \\ z \\ k_1 \\ k_2 \\ k_3 \end{bmatrix} \quad (4.8)$$

, which is defined as

$$\mathbf{m}_{(3n \times 1)} = \mathbf{F}_{(3n \times 6)} \cdot \mathbf{p}_{(6 \times 1)} \quad (4.9)$$

As a consequence of the full column rank of \mathbf{F} , we can apply Moore-Penrose pseudoinverse. Then,

$$\begin{aligned} \mathbf{p} &= \mathbf{F}^\dagger \cdot \mathbf{m} \\ &= (\mathbf{F}^\top \mathbf{F})^{-1} \mathbf{F}^\top \cdot \mathbf{m} \end{aligned}$$

From now on, we have already known the centroid position of end effector in the sensor frame and values of the constants k_1, k_2, k_3 .

Gravity Compensation and Initial Value Reset

Next, let us return to the first equation in Figure 4.1. We continue to use this formula and contemplate it from the perspective of coordinate transformation relation. Here we hypothesize that the end effector weighs g kilograms relative to the frame{0} which is also the world frame. That means the gravity vector of the end effector ${}^0\mathbf{g}$ is $[0, 0, -g]$ in the frame{0}. Then, we can derive it as following.

$$\begin{aligned} \text{Initial value} + \text{Gravity Load} &= \text{Actual Value} \\ \Rightarrow \mathbf{f}_0 + {}^S_6\mathbf{R} \cdot {}^6_0\mathbf{R} \cdot {}^0\mathbf{g} &= \mathbf{f} \end{aligned} \quad (4.10)$$

which is relative to frame {6}. Hence, we assume an installation angle θ including assembly error.

$${}^S_6\mathbf{R} = \begin{bmatrix} \cos(\theta) & \sin(\theta) & 0 \\ -\sin(\theta) & \cos(\theta) & 0 \\ 0 & 0 & 1 \end{bmatrix} \quad (4.11)$$

Besides, we can easily calculate ${}^6_0\mathbf{R}$ from Equation 3.1.

$$\begin{aligned} {}^6_0\mathbf{R} &= {}^0_6\mathbf{R}^\top \\ &:= \begin{bmatrix} r_{11} & r_{12} & r_{13} \\ r_{21} & r_{22} & r_{23} \\ r_{31} & r_{32} & r_{33} \end{bmatrix} \end{aligned} \quad (4.12)$$

Therefore,

$$\begin{bmatrix} f_{0x} \\ f_{0y} \\ f_{0z} \end{bmatrix} + \begin{bmatrix} \cos(\theta) & \sin(\theta) & 0 \\ -\sin(\theta) & \cos(\theta) & 0 \\ 0 & 0 & 1 \end{bmatrix} \begin{bmatrix} r_{11} & r_{12} & r_{13} \\ r_{21} & r_{22} & r_{23} \\ r_{31} & r_{32} & r_{33} \end{bmatrix} \begin{bmatrix} 0 \\ 0 \\ -g \end{bmatrix} = \begin{bmatrix} f_x \\ f_y \\ f_z \end{bmatrix} \quad (4.13)$$

Further, we rewrite it as

$$\begin{bmatrix} -r_{13} & -r_{23} & 0 & 1 & 0 & 0 \\ -r_{23} & r_{13} & 0 & 0 & 1 & 0 \\ 0 & 0 & -r_{33} & 0 & 0 & 1 \end{bmatrix} \begin{bmatrix} g \cos(\theta) \\ g \sin(\theta) \\ g \\ f_{0x} \\ f_{0y} \\ f_{0z} \end{bmatrix} = \begin{bmatrix} f_x \\ f_y \\ f_z \end{bmatrix} \quad (4.14)$$

In the same way as Equation 4.6, we can extract $[g \cos(\theta), g \sin(\theta), g, f_{0x}, f_{0y}, f_{0z}]$ by the least square solution. Note that, we can simultaneously record these data when using the method in Equation 4.6. By recording $n(n \geq 3)$ third columns of rotation matrices and corresponding n force vectors from F/T sensor, we can expand Equation 4.14 as

$$\begin{bmatrix} -r_{13}^1 & -r_{23}^1 & 0 & 1 & 0 & 0 \\ -r_{23}^1 & r_{13}^1 & 0 & 0 & 1 & 0 \\ 0 & 0 & -r_{33}^1 & 0 & 0 & 1 \\ -r_{13}^2 & -r_{23}^2 & 0 & 1 & 0 & 0 \\ -r_{23}^2 & r_{13}^2 & 0 & 0 & 1 & 0 \\ 0 & 0 & -r_{33}^2 & 0 & 0 & 1 \\ \vdots & & & & & \\ -r_{13}^n & -r_{23}^n & 0 & 1 & 0 & 0 \\ -r_{23}^n & r_{13}^n & 0 & 0 & 1 & 0 \\ 0 & 0 & -r_{33}^n & 0 & 0 & 1 \end{bmatrix} \begin{bmatrix} g \cos(\theta) \\ g \sin(\theta) \\ g \\ f_{0x} \\ f_{0y} \\ f_{0z} \end{bmatrix} = \begin{bmatrix} f_{0x}^1 \\ f_{0y}^1 \\ f_{0z}^1 \\ f_{0x}^2 \\ f_{0y}^2 \\ f_{0z}^2 \\ \vdots \\ f_{0x}^n \\ f_{0y}^n \\ f_{0z}^n \end{bmatrix} \quad (4.15)$$

, which is defined as

$$\mathbf{M}_{(3n \times 6)} \cdot \mathbf{p}_{(6 \times 1)} = \mathbf{f}_{(3n \times 1)} \quad (4.16)$$

As a consequence of the full column rank of \mathbf{M} , we can apply Moore-Penrose pseudoinverse. Then,

$$\begin{aligned} \mathbf{p} &= \mathbf{M}^\dagger \cdot \mathbf{f} \\ &= (\mathbf{M}^\top \mathbf{M})^{-1} \mathbf{M}^\top \cdot \mathbf{f} \end{aligned}$$

Apparently, we can directly obtain $g, f_{0x}, f_{0y}, f_{0z}$. Afterwards, we substitute them into Equation 4.7 to calculate

$$\begin{cases} \tau_{0x} = k_1 + (f_{0z} \cdot y + f_{0y} \cdot z) \\ \tau_{0y} = k_2 + (f_{0x} \cdot z + f_{0z} \cdot x) \\ \tau_{0z} = k_3 + (f_{0y} \cdot x + f_{0x} \cdot y) \end{cases} \quad (4.17)$$

Finally, we successfully obtain the weight of the end effector g , the initial value of the F/T sensor $[f_{0x}, f_{0y}, f_{0z}, \tau_{0x}, \tau_{0y}, \tau_{0z}]$.

As for installation angle θ including assembly error, there is an further discussion. Undoubtedly, we can derive it as

$$\theta = \cos^{-1} \left(\frac{g \cos(\theta)}{g} \right) \text{ or } \sin^{-1} \left(\frac{g \sin(\theta)}{g} \right) \quad (4.18)$$

In theory, By either the arccos function or arcsin function, we can derive the same value. However, we estimate $[g \cos(\theta), g \sin(\theta), g, f_{0x}, f_{0y}, f_{0z}]$ by using the least square solution which produce a approximated answer rather than the correct answer. A subtle bias caused by the least square solution will be enlarged through

the arc function. Thankfully, we originally designed an adapter to connect the robot arm and F/T sensor, and the installation angle is exactly zero degrees. Therefore, here we only need to concern about the subtle bias result from assembly errors.

Here we take the same bias and compare arccos to arcsin. Obviously, if we

Table 4.1: Comparison of arc-functions

bias n (rad)	$\sin^{-1}(n)$ (degree)	$\cos^{-1}(1 - n)$ (degree)
0	0	0
0.001	0.057	2.56
0.01	0.57	8.11
0.1	5.7	25.84

separately give the same bias (0.1 rad) into the arccos and arcsin function, the arccos function will enlarge the bias significantly larger than the arcsin function.

Hence we should use

$$\theta = \sin^{-1} \left(\frac{g \sin(\theta)}{g} \right) \quad (4.19)$$

Notably, as a result of the zero installation angle we initially designed from Table 4.1, we could infer using the arcsin function. In contrast, if the installation angle is not zero, the above assumption will be invalid.

Ultimately, we have successfully dissected the actual value of the F/T sensor into the initial value of the F/T sensor and the gravity of the end effector.

External Force Evaluation

Next, we continue to review the second equation in Figure 4.1.

$$\text{Initial value} + \text{Gravity Load} + \text{External Force} = \text{Actual Value}$$

$$\Rightarrow \begin{cases} f_0 + f_g + f_e = f \\ \tau_0 + \tau_g + \tau_e = \tau \end{cases} \quad (4.20)$$

Therefore,

$$\begin{aligned} f_e &= f - f_0 - f_g \\ &= f - f_0 - {}^S_6\mathbf{R} \cdot {}^6_0\mathbf{R} \cdot {}^0g \end{aligned} \quad (4.21)$$

$$\tau_e = \tau - \tau_0 - \tau_g$$

$$= \tau - \tau_0 - \mathbf{r} \times f_g$$

$$\Rightarrow \begin{cases} f_{ex} = f_x - f_{0x} + g \cos(\theta)r_{13} + g \sin(\theta)r_{23} \\ f_{ey} = f_y - f_{0y} - g \sin(\theta)r_{13} + g \cos(\theta)r_{23} \\ f_{ez} = f_z - f_{0z} + gr_{33} \\ \tau_{ex} = f_x - \tau_{0x} - (g_z \cdot y - g_y \cdot z) \\ \tau_{ey} = f_y - \tau_{0y} - (g_x \cdot z - g_z \cdot x) \\ \tau_{ez} = f_z - \tau_{0z} - (g_y \cdot x - g_x \cdot y) \end{cases}$$

4.3 Dragging Mode

In the hope that dentist could drag our system to an infected tooth by holding the end effector, we usher in admittance control based on F/T sensor.

Admittance Control based on F/T sensor

Control Scheme

Admittance control makes the robot move like a spring-mass-damper system. Forces and torques can be mapped into the movements such as position or velocity. Most importantly, admittance control enables a robot arm to cooperate with humans in a safe work environment. Since Meca500 is an industrial robot arm without admittance control, we subsequently combine the robot arm with the F/T sensor to adopt admittance control. With force and torque feedback, the F/T sensor makes Meca500 be like a collaborative robot arm. Therefore, we propose a control scheme depicted as Figure 4.2. It's worth noting that in this approach, the admittance control function is triggered by the end effector mounted on the F/T sensor instead of detecting each wrist torque of the robot arm.

A standard equation of admittance control is represented as Equation 4.22.

The values we obtain from the F/T sensor are $[f_x, f_y, f_z, \tau_x, \tau_y, \tau_z]$, whose forces $[f_x, f_y, f_z]$ are related to the translations $[x, y, z]$ and torques $[\tau_x, \tau_y, \tau_z]$ are related

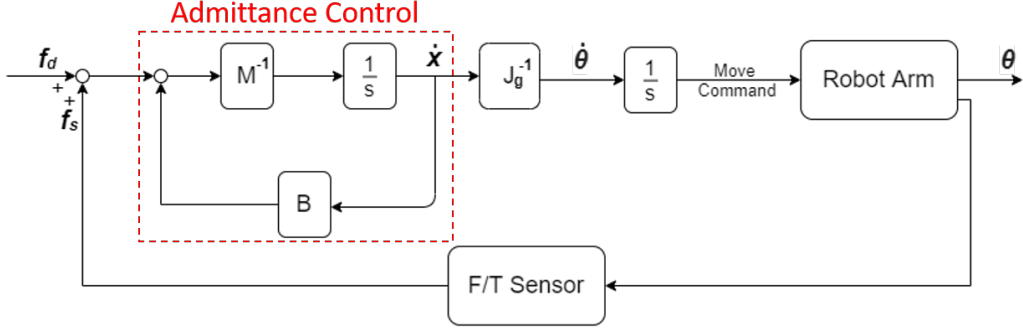


Figure 4.2: Control scheme. f_d denotes the desired forces and torques vector.

f_s denotes the real value detected by F/T sensor and is also a forces and torques vector. \dot{x} denotes $[\dot{x}, \dot{y}, \dot{z}, \dot{\theta}_x, \dot{\theta}_y, \dot{\theta}_z]$. J_g denotes the geometric Jacobian matrix. $\dot{\theta}$ denotes $[\dot{\theta}_1, \dot{\theta}_2, \dot{\theta}_3, \dot{\theta}_4, \dot{\theta}_5, \dot{\theta}_6]$. θ denotes $[\theta_1, \theta_2, \theta_3, \theta_4, \theta_5, \theta_6]$.

to the axis angle $[\theta_x, \theta_y, \theta_z]$.

$$\begin{bmatrix} x \\ y \\ z \\ \theta_x \\ \theta_y \\ \theta_z \end{bmatrix} = \frac{1}{\mathbf{M}s^2 + \mathbf{B}s + \mathbf{K}} \begin{bmatrix} f_x \\ f_y \\ f_z \\ \tau_x \\ \tau_y \\ \tau_z \end{bmatrix} \quad (4.22)$$

Selection of Admittance Control Model

In our proposed approach, we omit parameter \mathbf{K} which is relevant to spring stiffness, considering that it's not necessary to bounce such as a spring. Therefore,

our system should behave like a mass-damper system as following.

$$\begin{bmatrix} x \\ y \\ z \\ \theta_x \\ \theta_y \\ \theta_z \end{bmatrix} = \frac{1}{Ms^2 + Bs} \begin{bmatrix} f_x \\ f_y \\ f_z \\ \tau_x \\ \tau_y \\ \tau_z \end{bmatrix} \quad (4.23)$$

where M , B , K are diagonal positive definite matrices. Affections of these parameters will be discussed in section 4.5.

Robot Command Decision

After determining our admittance control model, we should select a corresponding command to move the robot. However, there are many commands of moving the robot arm, as shown in Table 4.2.

Table 4.2: Moving commands in Meca500

Types	Commands	Input parameters
Position	MoveJoints	$\theta_1, \theta_2, \theta_3, \theta_4, \theta_5, \theta_6$
	MovePose	$x, y, z, \alpha, \beta, \gamma$
Velocity	MoveJointsVel	$\dot{\theta}_1, \dot{\theta}_2, \dot{\theta}_3, \dot{\theta}_4, \dot{\theta}_5, \dot{\theta}_6$
	MoveLinVelTRF	$\dot{x}, \dot{y}, \dot{z}, \dot{\theta}_x, \dot{\theta}_y, \dot{\theta}_z$

Position commands is better than velocity commands because Meca500 has a default time-out value to ensure its safety. Even though we could set this value

from 0.001 to 2 seconds, Meca500 is still restricted to move with this value. For example, the value of time-out is set 0.1 sec. While the robot receives a command, the robot move for 0.1 sec then immediately stops. It's not easy to control via velocity command due to this default property.

Therefore, there are two suitable ways to command robot - MovePose and MoveJoints. Implementation of MovePose $(x, y, z, \alpha, \beta, \gamma)$ is easier than MoveJoints because MovePose is considered in tool frame. That means it will move $(x, y, z, \alpha, \beta, \gamma)$ based on the current tool frame. (x, y, z) can be obtained by multiplying an integrator with $(\dot{x}, \dot{y}, \dot{z})$. As for (α, β, γ) , $(\dot{\alpha}, \dot{\beta}, \dot{\gamma})$ can be obtained by multiplying the inverse matrix of analytical jacobian which was mentioned in Equation 3.3 with $\dot{\theta}_x, \dot{\theta}_y, \dot{\theta}_z$, and then (α, β, γ) can be obtained by multiplying an integrator with $(\dot{\alpha}, \dot{\beta}, \dot{\gamma})$.

However, considering that the singularity problem is an imperative subject in robotics, we intend to use MoveJoints to set the axes' angles directly. Despite that it's easier to implement admittance control via other commands, the system would touch the singularity point at any time. It undoubtedly exposes patients to danger because of the uncertainty of the system. In our case, we could detect whether it is a singularity or not before commanding the robot. Therefore, position command - MoveJoints and velocity command - MoveJointsVel is our option.

Finally, we designate MoveJoints $\theta_1, \theta_2, \theta_3, \theta_4, \theta_5, \theta_6$ as our main command. Thanks to the property of Jacobian matrix shown in Equation 3.12, we can transform \dot{x} into \dot{q} . Then we multiply it an integrator $\frac{1}{S}$ to obtain q . Note that, because

F/T sensor is mounted on the frame{6}, we should use Equation 3.12 rather than Equation 3.6.

Implementation in Discrete Time

To implement it in practice, we use the bilinear transformation, also known as Tustin method, to control it in discrete time.

$$\begin{aligned} \frac{\mathbf{v}(s)}{\mathbf{f}(s)} &= (\mathbf{M}s + \mathbf{B})^{-1} \\ \Rightarrow \frac{\mathbf{v}(z)}{\mathbf{f}(z)} &= \frac{T(1 + z^{-1})}{(T \cdot \mathbf{B} + 2\mathbf{M}) + (T\mathbf{B} - 2\mathbf{M}) \cdot z^{-1}} \end{aligned} \quad (4.24)$$

and,

$$\begin{aligned} \frac{\boldsymbol{\theta}(s)}{\mathbf{w}(s)} &= \frac{\mathbf{K}}{s} \\ \Rightarrow \frac{\boldsymbol{\theta}(z)}{\mathbf{w}(z)} &= \frac{TK}{2} \frac{1 + z^{-1}}{1 - z^{-1}} \end{aligned} \quad (4.25)$$

Therefore,

$$\begin{aligned} \mathbf{v}[k+1] &= \frac{T}{TB + 2M} \cdot (\mathbf{f}[k+1] + \mathbf{f}[k]) - \frac{TB - 2M}{TB + 2M} \cdot \mathbf{v}[k] \\ \boldsymbol{\theta}[k+1] &= \boldsymbol{\theta}[k] + \frac{TK}{2} (\mathbf{w}[k+1] + \mathbf{w}[k]) \end{aligned} \quad (4.26)$$

where T is the sampling time.

4.4 Self-Alignment Mode

This section aims to develop a framework for robot self-alignment regarding the position and orientation of the root canal, which is one of the main contributions of the thesis. This function assists endodontists in operating the cleaning procedure

automatically and ensures a postoperative recovery for patients. The main idea is to amend the direction of insertion by itself to lower the contact resistance.

We propose a complete robotic procedure. First and foremost, the prominent role of this procedure is the root canal reamer. We rotate the root canal reamer to clean a pulp, move it to do reciprocation and self-alignment. So, we care about the root canal, such as its position, orientation, rotation speed, and contact force. Nevertheless, the robot arm and the F/T sensor have their coordinates initially. They originally recognize its own coordinates rather than the root canal reamer's frame, so they do their work respectively. Therefore, we need to let them understand the tool frame. Thanks to section 3.4, we have demonstrated how to change the reference frame of the robot arm. After that, we can identify the translation and rotation information of the root canal reamer and subsequently obtain the transformation matrix from the robot arm to the tool. As for the F/T sensor, we have explained how to do gravity compensation in section 4.2, we will interpret how to change its fiducial to the tooltip in section 4.4. Besides, we will advance motion planning in accordance with the dentist's motion and standard surgical solution in section 4.4

Coordinate Transformation of F/T sensor

Similar to Coordinate transformation of F/T sensor in section 3.4. The F/T sensor originally recognizes its coordinate rather than the root canal reamer's frame. Namely, the F/T sensor receives unmatched data when the tool contacts an obstacle

due to the wrong reference frame. Hence, here we illustrate how to obtain the coordinate transformation of the F/T sensor to decouple the force and torque from frame $\{S\}$ to the frame $\{T\}$. We analyze it from two perspectives - reference frame changing and measurement point changing.

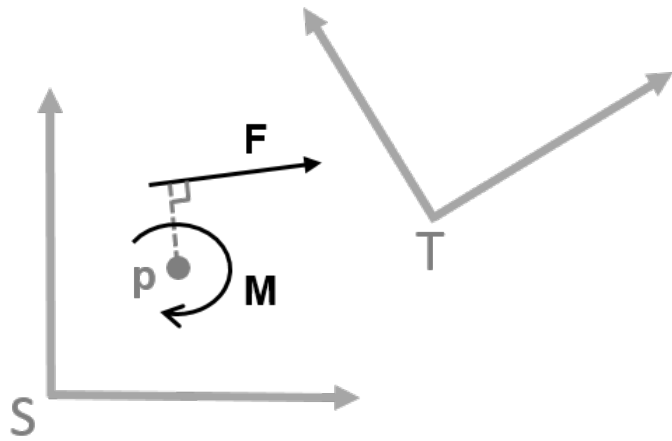


Figure 4.3: Illustration of changing reference frame from $\{S\}$ to $\{T\}$. f and m respectively denote a force and a moment measured at point p.

In view of reference frame changing in Figure 4.3, we can derive the following equation.

$$\begin{bmatrix} f_p \\ m_p \end{bmatrix}_{\{T\}} = \begin{bmatrix} {}^T_S R & 0 \\ 0 & {}^S_T R \end{bmatrix} \begin{bmatrix} f_p \\ m_p \end{bmatrix}_{\{S\}} \quad (4.27)$$

On the other hand, in Figure 4.4 we describe a force and a torque observed in the

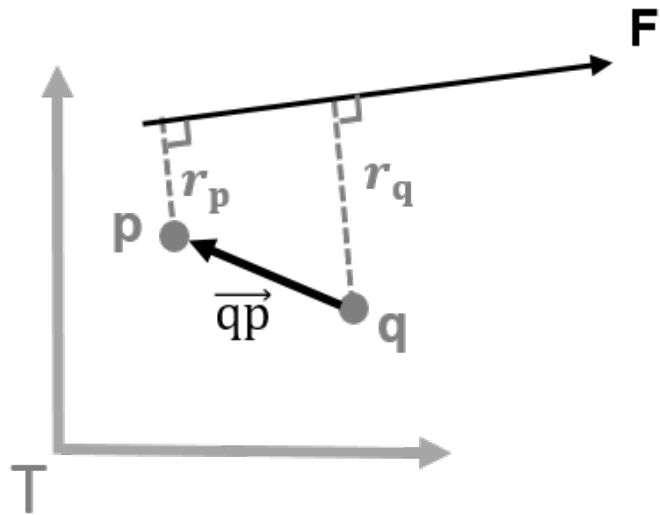


Figure 4.4: Illustration of changing reference frame from $\{S\}$ to $\{T\}$.

same frame but at a different point.

$$\begin{aligned}
 \mathbf{f} &= \mathbf{f}_p = \mathbf{f}_q \\
 \mathbf{m}_q &= \mathbf{r}_q \cdot \mathbf{f} \\
 &= \mathbf{r}_p \cdot \mathbf{f} + \overrightarrow{qp} \times \mathbf{f}_p \\
 &= \mathbf{m}_p + \overrightarrow{qp} \times \mathbf{f}_p
 \end{aligned} \tag{4.28}$$

Assume

$$\overrightarrow{qp} = \begin{bmatrix} u_1 \\ u_2 \\ u_3 \end{bmatrix}$$

then

$$\vec{qp} \times \mathbf{f}_p = \begin{bmatrix} 0 & -u_3 & u_2 \\ u_3 & 0 & -u_1 \\ -u_2 & u_1 & 0 \end{bmatrix} \begin{bmatrix} f_1 \\ f_2 \\ f_3 \end{bmatrix} \quad (4.29)$$

As a result, we consider reference frame changing and measurement point changing, and then we can obtain the following essential equation.

$$\begin{bmatrix} \mathbf{f}_q \\ \mathbf{m}_q \end{bmatrix}_{\{T\}} = \begin{bmatrix} \mathbf{I}_{3 \times 3} & \mathbf{0} \\ 0 & -u_3 & u_2 \\ u_3 & 0 & -u_1 & \mathbf{I}_{3 \times 3} \\ -u_2 & u_1 & 0 \end{bmatrix} \begin{bmatrix} {}^T_S \mathbf{R} & \mathbf{0} \\ \mathbf{0} & {}^T_S \mathbf{R} \end{bmatrix} \begin{bmatrix} \mathbf{f}_p \\ \mathbf{m}_p \end{bmatrix}_{\{S\}} \quad (4.30)$$

Motion Planning: Based on Admittance Control

Here we plan a series of motions to simulate the cleaning procedure of the root canal treatment. Endodontist uses their professional experience to determine how many force to apply and when to reverse the file to release the torque caused by the contact force. Because the root canal resembles a cone. The profundity of the file is larger, then the resultant force composed of contact forces is more significant. Namely, the endodontist will apply more and more pressure in the insertion direction during the surgery. To simulate this series of motions, we could directly command the robot arm to move with the series of actions. However, commanding the robot arm is a dilemma because we have already used admittance control which also commands the robot arm to move. Therefore, to solve the

conflict, we continue to utilize admittance control and propose a method based on admittance control to simulate the series of motions. Because we know the tool frame from section 3.4, we can regulate F_{des} to make the robot move. That means if we want to insert along with the tool direction, we could set $[00F_z000]$. While F_z is larger, the robot moves faster.

4.5 Parameter Selection

Because our system is similar to a mass-damper system, we focus on the performance of the velocity \dot{x} whereby the system could be considered as

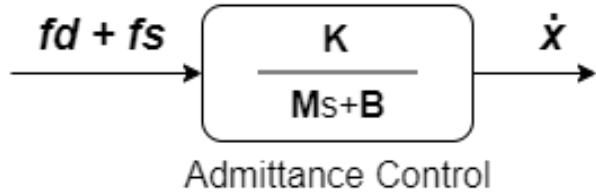


Figure 4.5: Control scheme. M , B , K are all diagonal positive definite matrices, whose diagonal indexes are respectively related to $x, y, z, \theta_x, \theta_y, \theta_z$. M, B are related to the inertial and damping respectively, and K is a proportional gain.

It is a first-order control system and its step response is

$$\begin{aligned}
 \mathcal{L}^{-1} \left[\frac{1}{S} \cdot \frac{K}{MS + B} \right] &= \mathcal{L}^{-1} \left[\frac{K}{B} \left(\frac{1}{S} - \frac{1}{S + \frac{B}{M}} \right) \right] \\
 &= \frac{K}{B} \left(1 - e^{-\frac{B}{M}t} \right)
 \end{aligned} \tag{4.31}$$

From the above derivation, we can know

$$\begin{aligned} \text{time constant } \tau &= \frac{M}{B} \\ \text{gain} &= \frac{K}{B} \end{aligned} \quad (4.32)$$

Hence, the transient response can be derived as

$$\begin{aligned} \text{Rise time} &= 2.3\tau = \frac{2.3M}{B} \\ \text{Settling time} &= 4\tau = \frac{4M}{B} \end{aligned} \quad (4.33)$$

In theory, when τ is larger, the pole is farther from the origin in S domain, the system is more stable. Besides, when τ is larger, the response speed is faster. Furthermore, when the gain $\frac{K}{B}$ is larger, the robot arm moves more. Therefore, we coarse-tune parameter K to adjust the whole gain of the system and determine the mode of the system is "Dragging Mode" or "Self-Alignment Mode". Last but not least, we fine-tune diagonal parameters of B separately because the inertial and spring properties of each axis are discrepant.

In practice, we implement it in discrete time. From Equation 4.24, we can further derive the final value in discrete time shown as

$$\text{gain} = \lim_{z \rightarrow 1} (z - 1) \cdot \frac{TK(z + 1)}{(TB + 2M)z + TB - 2M} \cdot \frac{1}{\frac{2}{T} \frac{z-1}{z+1}} = \frac{KT}{B} \quad (4.34)$$

Compared to the gain in continuous time, the sampling time in discrete time also effect the gain. Because the sampling time we set is 0.002s, we set ($m_i : b_i = 1 : 500$) to make ($\tau_i = \frac{m_i}{b_i} = 0.002$), then the system will rise up to 98% after 0.004 second. Further, we can alter K to easily regulate the gain. In Table 4.3, we show detailed parameters with "Dragging Mode" and "Self-Alignment Mode".

Table 4.3: Parameters setting of Admittance control.

Parameter	Dragging Mode	Self-Alignment Mode
k	60	10
b_1	80	80
b_2	80	80
b_3	80	80
b_4	160	80
b_5	160	80
b_6	160	80

$$\mathbf{K} = \text{diag}(k, k, k, k, k, k), \quad \mathbf{B} = \text{diag}(b_1, b_2, b_3, b_4, b_5, b_6)$$

Note that we change the different sensor frames with "Dragging Mode" and "Self-Alignment Mode". As shown in Fig 4.6, Point A and B are two origins of the sensor frame. In "Dragging Mode", we transform the sensor frame to the point A, and the operator can hold the point G_1 and G_2 to move the entire handpiece. On the other hand, in "Self-Alignment Mode" we set the point B as the new sensor frame because we focus on forces and torques the file bears. Due to different level arms, the forces we apply in each axis will be different. There are same level arms (\overline{AO} and \overline{OG}_2 both are 13.2 mm) if we set the point A as the sensor frame and grasp G_1 and G_2 to move the entire handpiec. Therefore, to provide users a good experience, we should regulate parameters of B in "Dragging mode" with suitable values. With these values, the users can smoothly move the robot arm to

the desired position and orientation. We set the first three variables relative to the linear velocity as the same values. Besides, We set the last three variables relative to the angular velocity as the other same values.

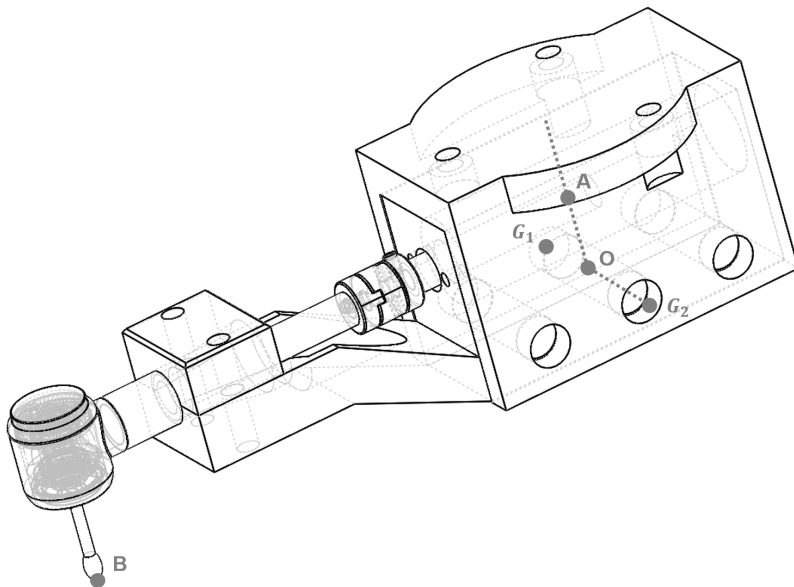


Figure 4.6: Reference point A in Dragging Mode. Reference point B and holding points G_1, G_2 in Self-Alignment Mode.

Chapter 5

File Feedrate Control

5.1 Problem Definition and the Proposed Method

Problem Definition

Instrument fracture is a potential crisis for endodontic treatment. If a dentist improperly operates an endodontic file, it will increase the possibility of instrument fracture. Most largely, the instrument fracture will happen while a file is inserted into the one-third place far from the root apex. It is barely possible to take out in a small root canal. Removal of broken files is technically tricky, so it is critical to reducing the probability of the instrument fracture.

There is a technical solution to detect a status of a file. When a file suffers a force, it will lead to the crystalline phase transformation. However, it can only be observed from a microscope. It is impracticable to usually monitor it during the surgery. Previous literature shows there are two main causes of fractured files are torsional fracture and flexural fatigue, which account for 55.7% and 44.3% separately[8]. Therefore, we can reduce the torque a file bears to prevent the instrument fracture.

File Property

To protect the endodontic file from fracturing, we need to be familiar with its physical property and its correct operations. We delve into the physical properties of an endodontic file. A file is made of alloys of Nickel and Titanium, which is a superelastic material. The Ni-Ti file has significantly more elastic and incorruptible properties. This feature allows it to bend when inserted into a curve root canal and thereby reduces the possibility of stuck.

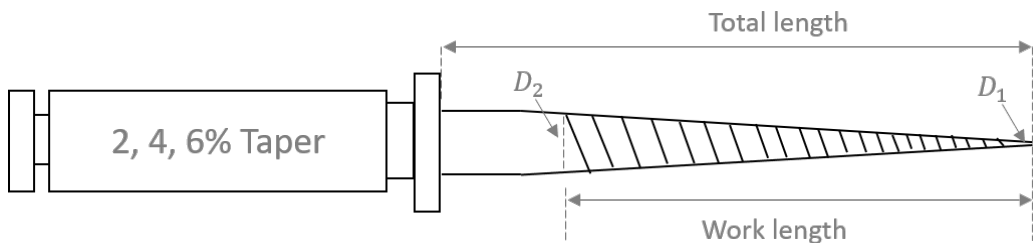


Figure 5.1: The illustration of an endodontic file

In Fig 5.1, an endodontic file is illustrated. There are four types of total length - 21, 25, 28, and 31 mm. They all have the same work length - 16 mm. Each file has their own number such as #15, #20, #25, ..., #40 shown as Fig 5.2, which represent the diameter of files. Take a #15 file with 2% taper for example, the diameter of the tooltip D_1 is

$$15/100 = 0.15 \text{ (mm)}$$

and the diameter at the end of the work length D_2 is

$$0.15 + 16 \cdot 6\% = 1.11 \text{ (mm)}$$

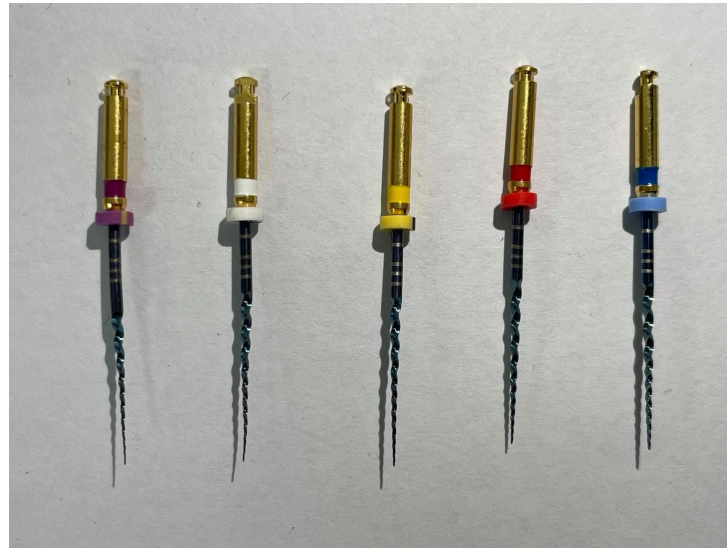


Figure 5.2: Endodontic files with different diameters

The Proposed Method

In order to protect an endodontic file from fracturing, we need to reduce the file torque. The easiest and most effective way to solve this issue would be monitoring the torque which the file is enduring. Therefore, we implement a torque monitoring system on DentiBot. We utilize current feedback to keep track of the torque. An increase in the current of the motor is indicative of the contact resistance of the file. Also, We propose two approaches to release the file torque. One is inverse rotation control discussed in section 5.2 and the other is feed control discussed in section 5.3, they are both efficient ways to release the file torque. Once the torque of the file is in excess of a threshold, it will inversely rotate or decline the feedrate to release torque.

How to measure the file torque

There are two approaches to measure the file torque. One is detecting the current of motor which drives the file rotation to estimate the file torque. The other is directly obtained from the F/T sensor after changing the reference frame to the tool frame.

Here we delves into the first method - detecting the current of motor to estimate the file torque. A motor can be modelled as an RL circuit. In this way, we can get the following formula

$$V = R \cdot I + L \cdot \frac{dI}{dt} + \varepsilon \quad (5.1)$$

where V represents the input voltage, I represents the input current, and ε represents the back EMF produced by the motor motion.

Since the value of the inductance of DC motor is small, we ignore the inductance term L . After transposition, we can get the following relation between the current and the back EMF.

$$I = \frac{V - \varepsilon}{R} \quad (5.2)$$

The back EMF produced by the motor is dependent upon the motor constant K , shown as the following equation.

$$\varepsilon = K \cdot \frac{d\theta(t)}{dt} = K \cdot \omega(t) \quad (5.3)$$

When the file encounters resistance during the drilling procedure, the rotating speed of the motor would slow down. With the Equation 5.2 and 5.3 we can infer

that the back EMF would decrease, and the current would increase. Also, we have the relation between the current and torque

$$T_m = K_m \cdot I \quad (5.4)$$

where k_m represent the torque constant of a motor.

The maximum torque a root canal file can bear is 6.20 Ncm (62.0 mNm) [27]. Therefore, we can derive the following inequality.

$$T_m \cdot GR < 62 \text{ (mNm)} \quad (5.5)$$

where GR is gear ratio of gearbox mounted on a motor.

Hence, we can set a current threshold based on the following condition.

$$I_{max} < \frac{62}{GR \cdot K_m} \quad (5.6)$$

In realistic implementation, GR is 67 and K_m is 16mNm/A

5.2 Inverse Rotation Control

This proposed approach is an effective way to protect endodontic file from fracturing. Also, it can remove root debris cut by file and prevent file from getting stuck in root. Once the current of the file exceeds the specific threshold, it will inversely rotate for 90 degrees to release torque and then continue drilling in the original direction. Before designing the DentiBot, we have validated this function with the prototype of DentiBot shown as Fig 5.3. This prototype is a drilling system

mounted on a magnetic stand. The modified handpiece, a hand-held dental electric device, with a single axis mechanism can validate the inverse rotation control.

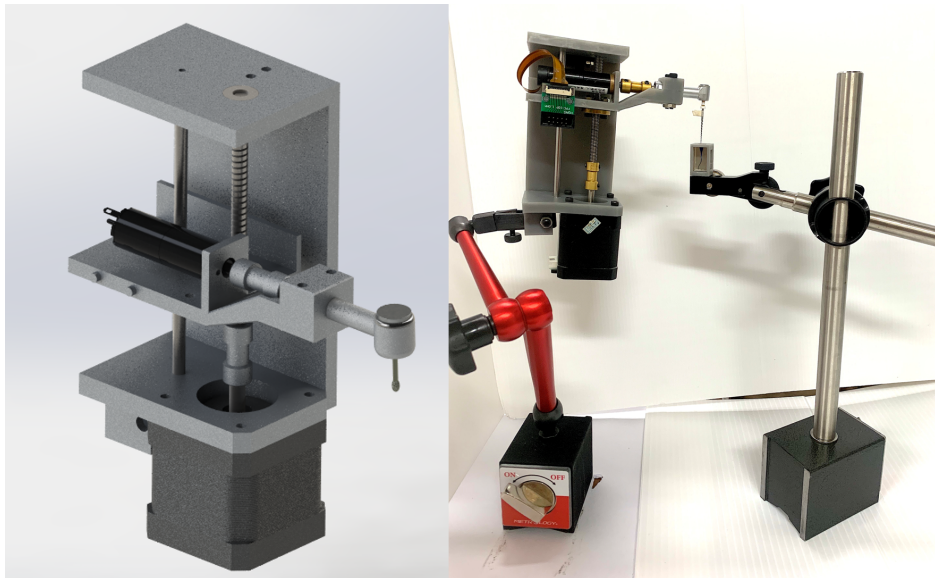


Figure 5.3: The prototype of DentiBot. A single z-axis manipulator with a modified handpiece

In Fig 5.4, a motion planning is designed to perform the drilling procedure. The root canal is divided into several sections to be cleaned. In the beginning, the robot moves to the start point and then repetitively drills one section back and forth at least ten times until the current feedback decrease under the specific threshold. If the torque exceeds the threshold, the endodontic file will inversely rotate for 90 degrees to release the torque and then drill the same section again. After one section is cleaned thoroughly, the drilling file will move to the next section. Every section will be cleaned for at least 10 rounds. If there is reverse rotation, it will be more than 10 rounds. When to finish is contingent on whether the endodontic file

reaches the final section.

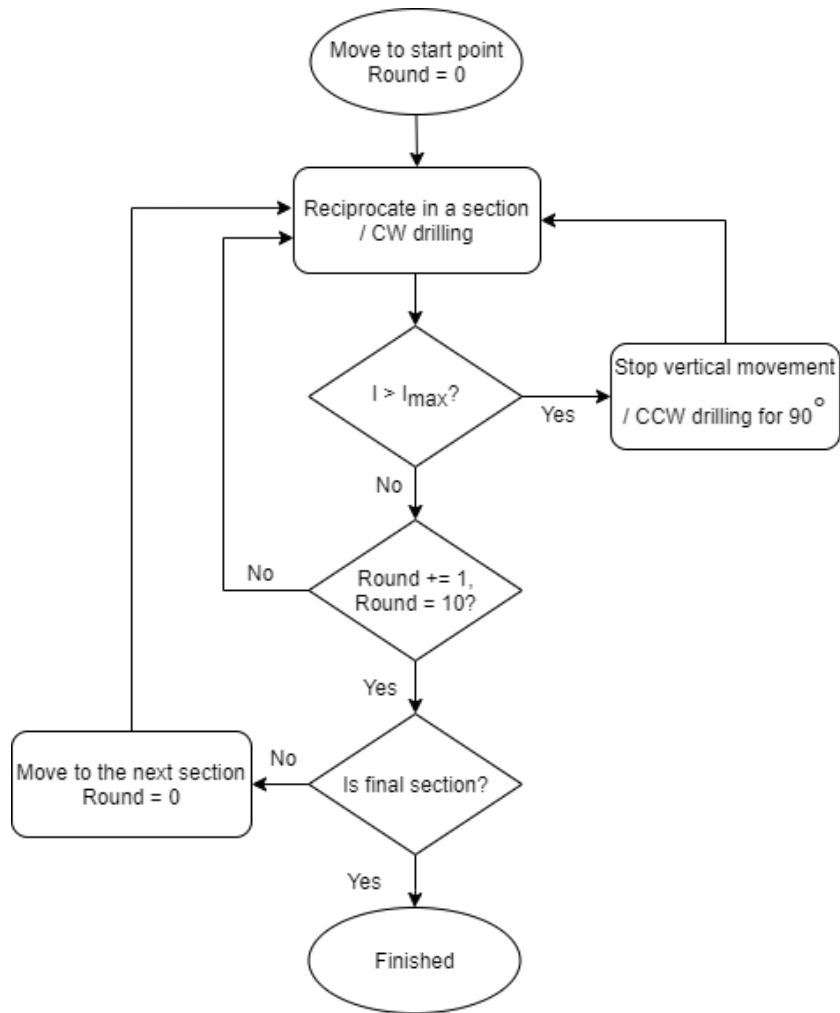


Figure 5.4: Motion planning of Inverse Rotation Control with the prototype of DentiBot.

In conclusion, by the preliminary experiment with the prototype of DentiBot, it has been proved that the inverse control rotation is an effective approach to reduce the torque. Therefore, we can detect the current to estimate the torque and inversely rotate the motor if the current exceeds the threshold current.

5.3 Feedrate Control

As mentioned above, we have validated the inverse rotation control with the prototype. However, inverse rotation control is just mimicking a dentist to perform endodontic treatment. It is still time-consuming. Hence, the other method - feed control is proposed to improve this problem. Note that this method can only be valid with DentiBot instead of its prototype because admittance control will be involved. Previous literature which dedicate to a form drilling with torque control is similar to our root drilling [27]. Regulating the feedrate to control the torque is an effective way to reduce time.

$$Vf = f \cdot N$$

where Vf denotes feedrate. f denotes feed per revolution. N denotes spindle speed (rpm).

As the above equation, regulating the feed and spindle can both affect feedrate. Refer to the previous literature, we set the spindle speed a constant (60 rpm) and the feed a variable. Therefore, we regulate the feed instead of the spindle speed to determine the feedrate. A similar control scheme for our root drilling is proposed and shown as Fig ??.

The input is T_{des} and the feedback is T . f_z^* will be determined by the difference of T_{des} and T via a PD controller. Here we use a minimum and maximum saturation to bound f_z^* and then output f_z . f_z is the input of admittance control and is relevant to the feed of z-axis. With the admittance control of DentiBot, DentiBot can

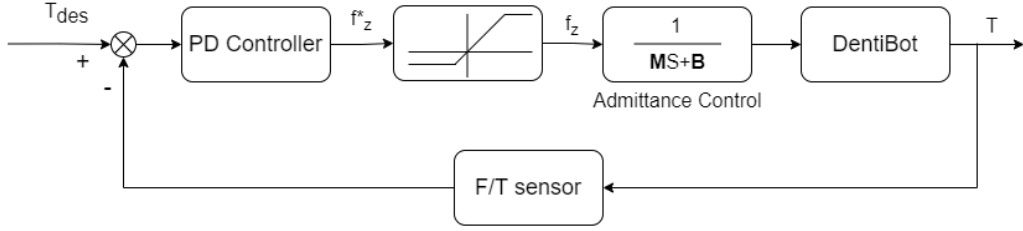


Figure 5.5: Control scheme of Feedrate Control with the DentiBot.

move along with the tool because f_z is related to the moving direction, which is exactly the insertion of tool. In conclusion, the feedrate can be regulated by the torque. When the file torque increases , DentiBot will decrease its moving velocity to control the increase rate of file torque. It is worth noting that we combine admittance control into this approach. This feature not only provides the moving direction, but also tracks the root path and patient moving. Once the F/T sensor detects the extra value different from $[0 \ 0 \ f_z \ 0 \ 0 \ 0]$, the DentiBot will move to the correspond position and orientation. Moreover, because the z-orientation should be only acted by the file rotation driven by the motor, it is important to turn off z-orientation of admittance control by setting the parameter b_6 of admittance control as a large value.

Entire flow chart is shown in Fig 5.6. Considering the realistic condition, Dentibot judges whether patient moving happens by checking whether $\|(f_x, f_y, f_z)\|$ is larger than 1.5 N. File rotation will stop and f_z will be zero to stop moving when the value is more than 1.5 N, then Dentibot can keep track of the patient moving. If not, Dentibot will continue drilling with feedrate control until the tooltip reaches

the apex of root. The feasibility is proven in experiment 1-3.

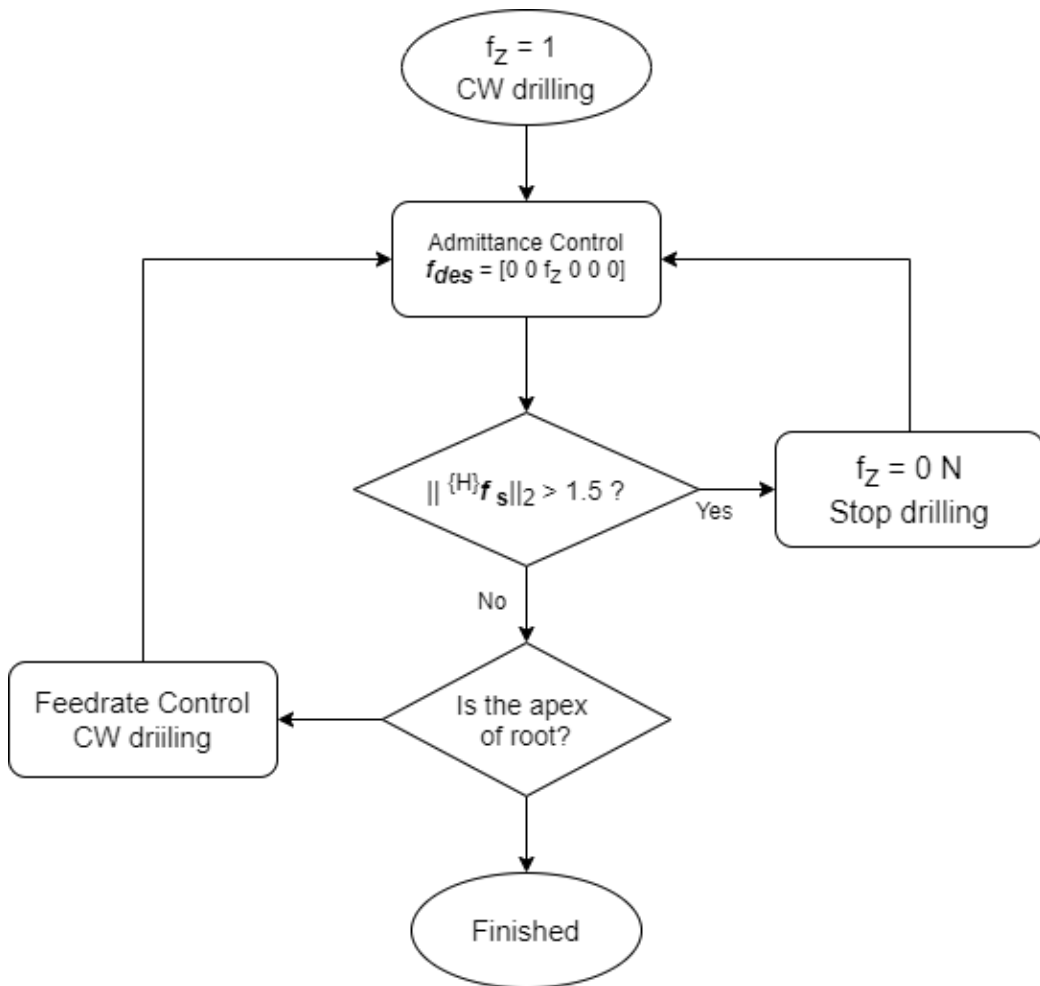


Figure 5.6: Flow chart of Feedrate Control with the DentiBot. f represents force vector

5.4 Automated Endodontic Treatment

After pre-clinical evaluation, we found that cleaning root only with force-guided alignment and feedrate control is impracticable. The endodontic file is easy to get

stuck in the root due to root debris. The stuck precipitates a dramatic increase of the file torque. File feedrate control can not handle the dramatic increase. The effective way to solve this problem is to rotate inverse the file. Because it is essential to withdraw to get rid of root debris cut by file. The new idea that combines for-guided alignment, inverse rotation control, and file feedrate control is proposed.

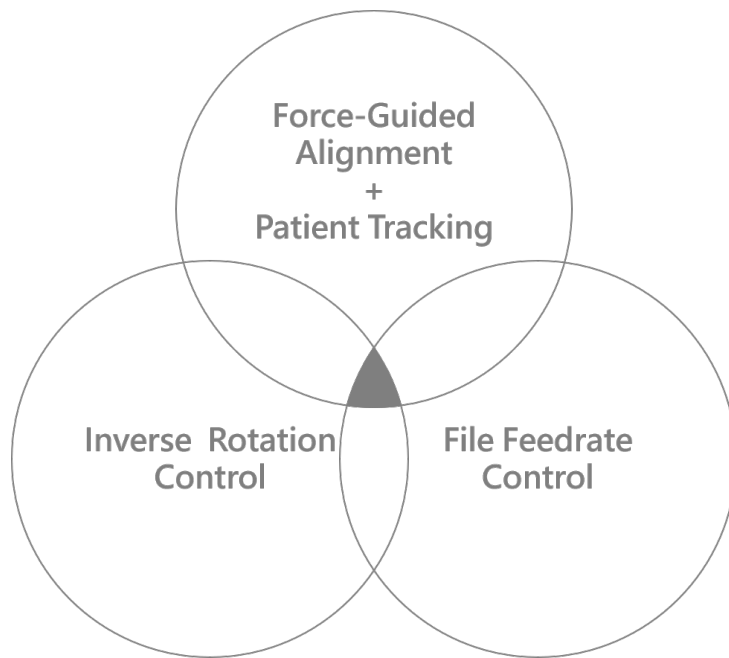


Figure 5.7: Methods of Automated Endodontic Treatment

In view of this, a new algorithm for automated endodontic treatment that combines for-guided alignment, inverse rotation control, and file feedrate control is proposed as shown in Fig 5.8.

Based on the flow chart of feedrate control in Fig 5.6, inverse rotation control is involved as shown in the left part. The minimum and maximum saturation is from -0.5 to 0.5. When the file torque exceeds the desired torque, Feedrate control will

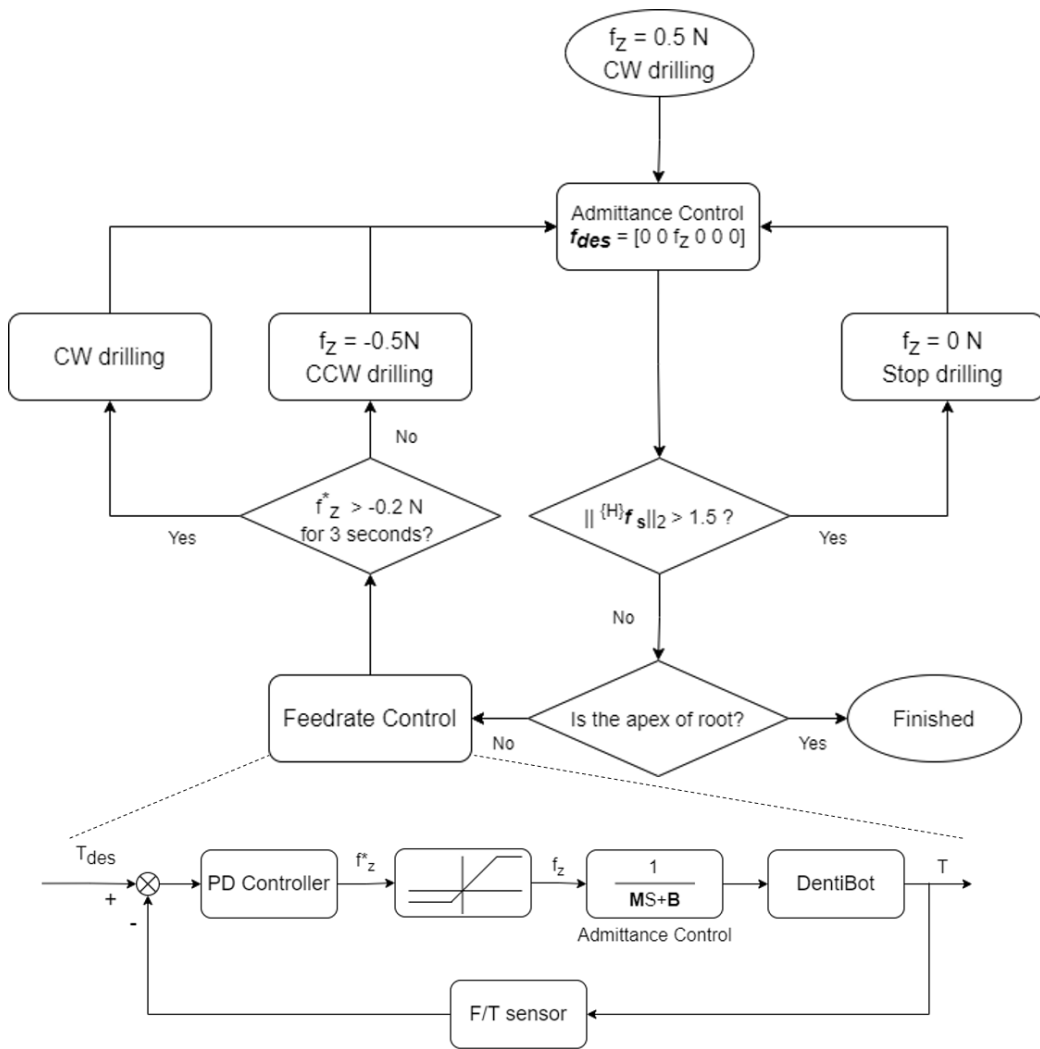


Figure 5.8: Algorithm for robot-assisted endodontic treatment

slow down the feed by output f_z^* with a negative value. If the file torque exceeds a little and f_z^* does not reach -0.2 , the file will keep clockwise drilling. The above function is essential because it provides the feedrate control a feasibility to regulate the torque. On the contrary, once the file torque exceeds much and f_z^* is smaller than -0.2 , it will trigger the inverse rotation control. That means the file torque increases dramatically so that the feedrate control can not handle with.

Chapter 6

Experiment Results

For checking and validating the proposed method, we set up experiments from technical and pre-clinical perspective. In technical perspective, admittance control, force-guided alignment, and file feedrate control were conducted and verified. On the other hand, in pre-clinical evaluation, acrylic root models before and after performing endodontic treatment with DentiBot were also compared in this chapter.

6.1 Experimental Setup

Software and Firmware Setup

To control and communicate with all devices in low latency, and high speed, a communication protocol - Ethernet for Control Automation Technology (EtherCAT) and a real-time operating system (RTOS) are interfaced. EtherCAT is constructed on EtherNET and utilizes "processing on the fly" technology. Therefore, it provides a short cycle time (less than 100 μ s) and a low jitter [23]. Besides, EtherCAT supports every type of network topologies such as daisy chain, star, and ring. All devices are connected in Daisy-chain with EtherCAT as shown in Fig 6.1. Graph user interface (GUI) and fundamental framework are constructed to reduce and eliminate future developing problems as shown in Fig 6.2.

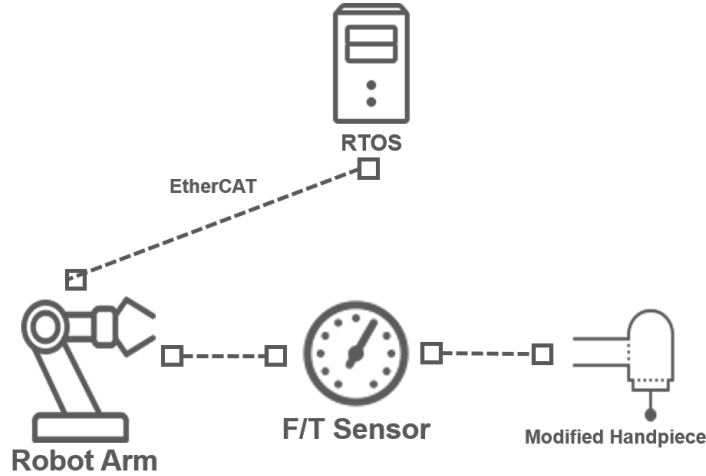


Figure 6.1: Communication protocol – EtherCAT. Master device is RT-target and slave devices are robot arm, F/T sensor and modified handpiece.

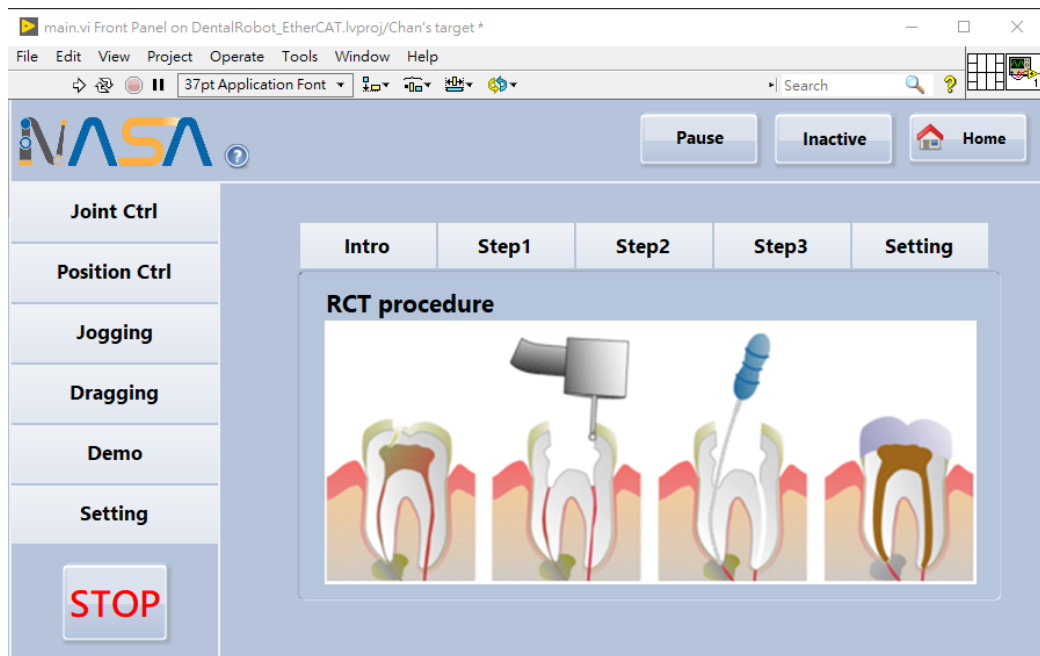


Figure 6.2: Graph user interface with LabVIEW 2018

Hardware Setup

In Fig 6.3, a motion capture system is incorporated to obtain the handpiece and root positions [28]. There were four cameras with high resolution sensor around the robot and their resolutions are around 1 mm. The motion capture system can capture LEDs and calculate their Cartesian position for 960 frames per second. Moreover, a Stewart platform on which a root acrylic model is mounted is set up to simulate a small patient moving.



Figure 6.3: Experimental setup with Dentibot, a motion capture system, and a Stewart platform

To record the handpiece and root positions, a LED marker is located on the driller and the other three LED markers forming a equilateral triangle are seated on the Stewart platform. Therefore, the handpiece position is directly obtained and the root position is calculated as following equation

$$p_{root} = \frac{p_1 + p_2 + p_3}{3}$$

where p_{root} denotes the root position and p_i denote the positions of LEDs obtained from the motion capture system.

Also, the positions related to the motion capture system frame are transformed to the Stewart platform frame. Note that there is an original offset of around 55 mm in the vertical direction between the root and handpiece in this setup. This original offset magnifies the relative distance on the X-axis and Y-axis. Also, An inaccurate 3-D print support used to stick three LEDs and acrylic roots lead to wrong centroid point and position biases. The flexible property of endodontic files absorbs contact forces and delays respond time. The root acrylic model has drilled thoroughly by a file and forms a cone shape in advance. Therefore, there is an another bias between the root and the endodontic file. Besides, if the motion capture system captures a LED with less than three cameras, the position information will be incorrect. To obtain stable data, four cameras are set up around the DentiBot and the Stewart platform. Therefore, there are many factors to affect the position result and should be in afterward discussion.

The specifications of the hardware and software environment set in the experiments are listed in Table 6.1. The detail specifications of the robot arm and F/T sensor are shown in Table 6.2 and Table 6.3.

Table 6.1: Specifications of the hardware and software environments

Item	Specification
Development Environment	LabVIEW 2018
Real-Time Operating System	National Instrument-RT target CPU: Intel Core 8
Communication Protocol	EtherCAT
Robot Arm	Mecademic-Meca500
F/T Sensor	ATI-Mini40
Handpiece Motor	Maxon - servo motor Gear ratio: 67
Motion Capture System	PhaseSpace-Impulse X2E Resolution: 1mm
Stewart Platform	Actuoanix - Linear Actuator

Table 6.2: Technical specifications of the robot arm - meca500

Payload	0.5 kg
Repeatability	0.005 mm
Reach (at wrist center)	260 mm
Total weight	4.5 kg
Joint range	joint 1: -175° to $+175^\circ$ joint 2: -70° to $+90^\circ$ joint 3: -135° to $+70^\circ$ joint 4: -170° to $+170^\circ$ joint 5: -115° to $+115^\circ$ joint 6: ± 100 revolutions
Speed of joints 1–6	150, 150, 180, 300, 300, 500 °/s
Brakes	On joints 1, 2 and 3
Robot mounting	Any orientation
Safety module	Category 3, PL d
Power supply	90-264 VAC, 50-60 Hz (in) / 24 VDC (out)
Communication	TCP/IP, EtherCAT, Ethernet/IP
Controller	Embedded in robot base
Protection rating	IP 40

Table 6.3: Technical specifications of the F/T sensor - mini40

Weight	0.0499 kg
Diameter	40 mm
Height	12.2 mm
Sensing range	Fx,Fy: 20 N Fz: 60 N Tx,Ty: 1 Nm Tz: 1 Nm
Resolution	Fx,Fy: 1/100 N Fz: 1/50 N Tx,Ty: 1/4000 Nm Tz: 1/4000 Nm
Single-axis overload	Fxy: ± 810 N Fz ± 2400 N Txy ± 19 Nm Tz ± 20 Nm
Stiffness (calculated)	X-axis & Y-axis forces (Kx, Ky): 1.1×10^7 N/m Z-axis force (Kz): 2.0×10^7 N/m X-axis & Y-axis torque (Ktx, Kty): 2.8×10^3 Nm/rad Z-axis torque (Ktz): 4.0×10^3 Nm/rad
Resonant Frequency	Fx, Fy, Tz: 3200 Hz Fz, Tx, Ty: 4900 Hz

6.2 Force-Guided Alignment

The aim of this experiment was to validate the feasibility of force-guided alignment and patient tracking while drilling, we set up three experiments with different scenarios. The metric was to check whether it was possible that the DentiBot inserted an endodontic file into a small root and confronted a patient moving at the same time.

Three experiment were designed with more and more functions listed below and shown in Fig 6.4.

1.1 Inserting without file rotation

1.2 Inserting with file rotation

1.3 Inserting with file rotation and file feedrate control

To simulate a patient moving, a Stewart platform with six degrees of freedom was incorporated. When the patient moved to a point, our system should move to the same place. Therefore, the target and handpiece positions would be compared to check if our system tracked the patient or not. PhaseSpace - Impulse X2E, a motion capture system, was involved in obtaining the above positions in real-time.

The Stewart platform was scheduled for motion planning. It would move to $(0, 0, 0)$, $(15, 0, 0)$, $(15, 0, 15)$, $(0, 0, 15)$ related to Stewart frame. These points formed a $15 * 15$ mm square composed of two horizontal and two vertical lines. The command position trajectory is illustrated in Fig 6.5. The Stewart platform

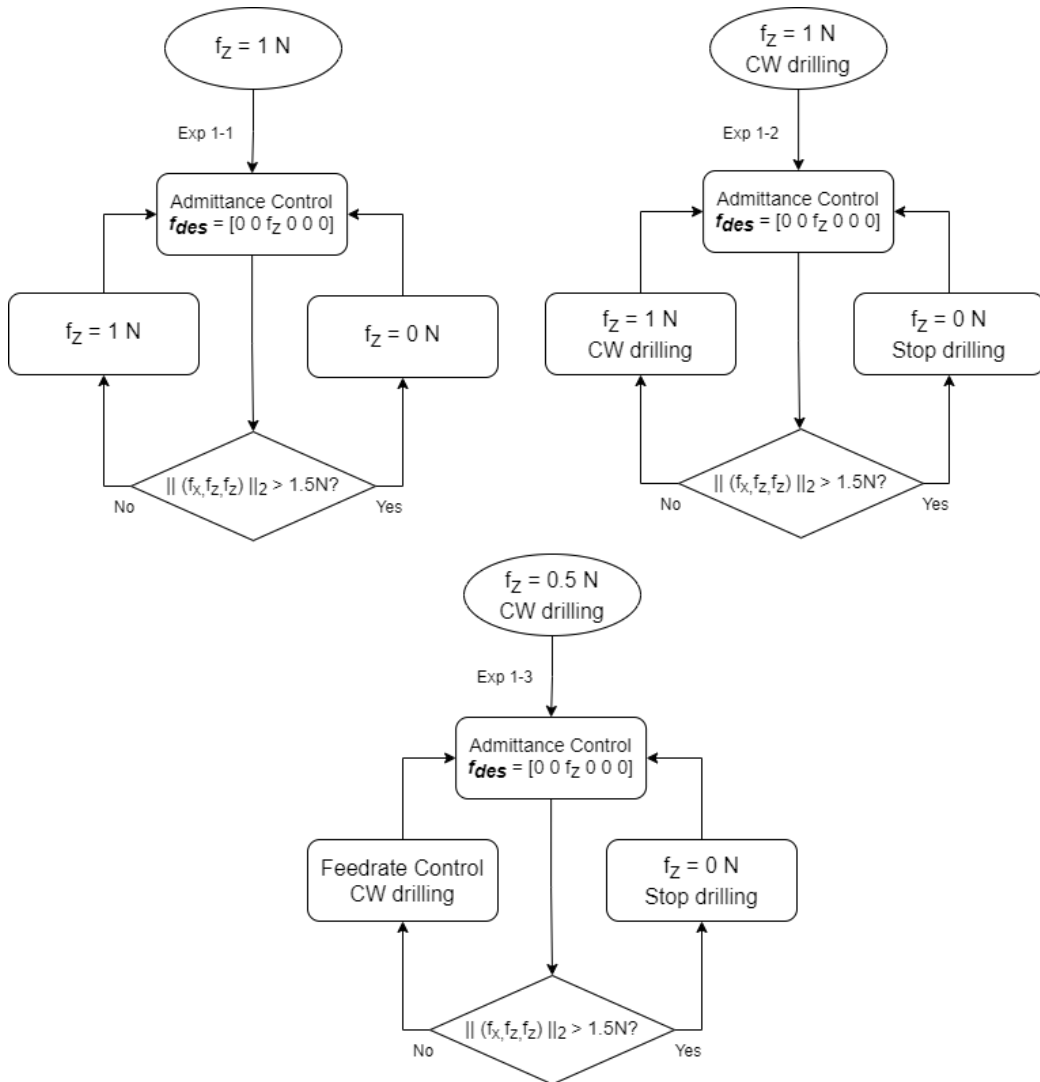


Figure 6.4: Flow charts for force-guided alignment experiment. The left and top figure is inserting without file rotation. The right and top figure is inserting with file rotation. The bottom figure is inserting with file rotation and file feedrate control.

is planned to go along with a square at 3 mm/s first, then stop for 10 seconds, then go along with a square at a faster velocity, and so on. The velocities of four rounds are 3 mm/s, 4 mm/s, 5 mm/s, and 6 mm/s. Each cycle took 20, 15, 12, 10 seconds separately and total experiment time was 87 seconds. Note that in reality linear interpolation was implemented to command the Stewart platform. The motion of the Stewart platform was received 4×100 steps and executed at an equally distributed time. Even though these 4 points were cut to 400 points and then calculated by inverse kinematics. The X-axis motion had an apparent distortion due to the hardware.

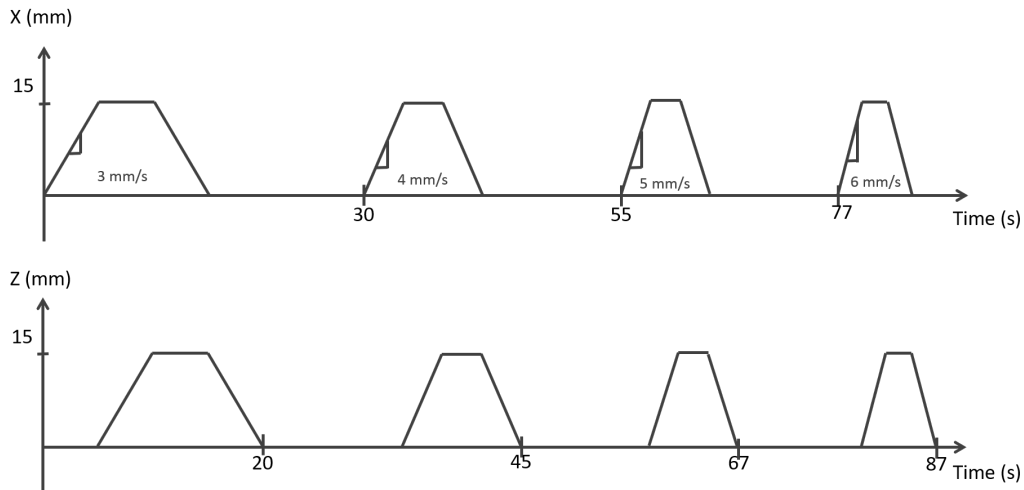


Figure 6.5: Position command of Stewart platform for force-guided alignment experiment

Parameters setting of admittance control in Experiment 1 is shown in Table 6.4. The parameter diagonal matrix \mathbf{K} is proportional to the gain and \mathbf{B} is inversely proportional to the gain. Therefore, the same values is set in all experiment except

b_6 . b_6 is relevant to the rotation along with Z-axis. The rotation along with Z-axis driven by the robot arm should be deactivated in Exp 1-2 and 1-3 because the file rotation is driven by the motor. If the rotation along with z-axis is on duty and the file is drilling, the robot arm would rotate along with Z-axis in opposite direction. Hence, b_6 is set a infinite value to deactivate the rotation along with Z-axis. Exp 1-3 is the last technical experiment and is designed as pre-clinical task, but the metrics are still same as the previous experiment. Because a slow inserting is required when performing the endodontic treatment. Therefore, the maximum value of f_z was set 0.5 in Exp 1-3 to limit the the highest velocity.

Table 6.4: Parameters setting of admittance control in Experiment 1.

Parameter	Exp 1-1	Exp 1-2	Exp 1-3
k	500	500	500
f_z	1	1	$-0.2 \sim 0.5$
b_1	80	80	80
b_2	80	80	80
b_3	80	80	80
b_4	80	80	80
b_5	80	80	80
b_6	80	∞	∞

$$\mathbf{K} = \text{diag}(k, k, k, k, k, k), \mathbf{B} = \text{diag}(b_1, b_2, b_3, b_4, b_5, b_6)$$

Results

There were three metric types of figures to show the results of Exp 1-1, 1-2, and 1-3 listed as following.

1. The position of handpiece and root and their relative distance
2. The force vs the velocity
3. The force vs the handpiece position

An imperative metric was whether the robot could move as the root moved. Therefore, the first figure was the position information. The position of handpiece and root were compared with and the relative distance between them was evaluated. The left blue axis of the first figure was for the position of hadndpiece and root and the right red one was for the relative distance. Second, the input of admittance control was force vector and output was velocity vector. Hence, the force and the velocity were compared in the second figure. The left blue axis of the second figure was for the force and the right red one was for the command velocity and real velocity. Last, the force and the position of robot were compared in the third figure. The left blue axis of the third figure was for the force, and the right red one was for the position of robot. Note that the real position and velocity data were transformed from the PhaseSpace frame to the Stewart platform frame. The force information were also transformed to the Stewart platform frame from the handpiece frame. Therefore, all data were all considered in the Stewart frame.

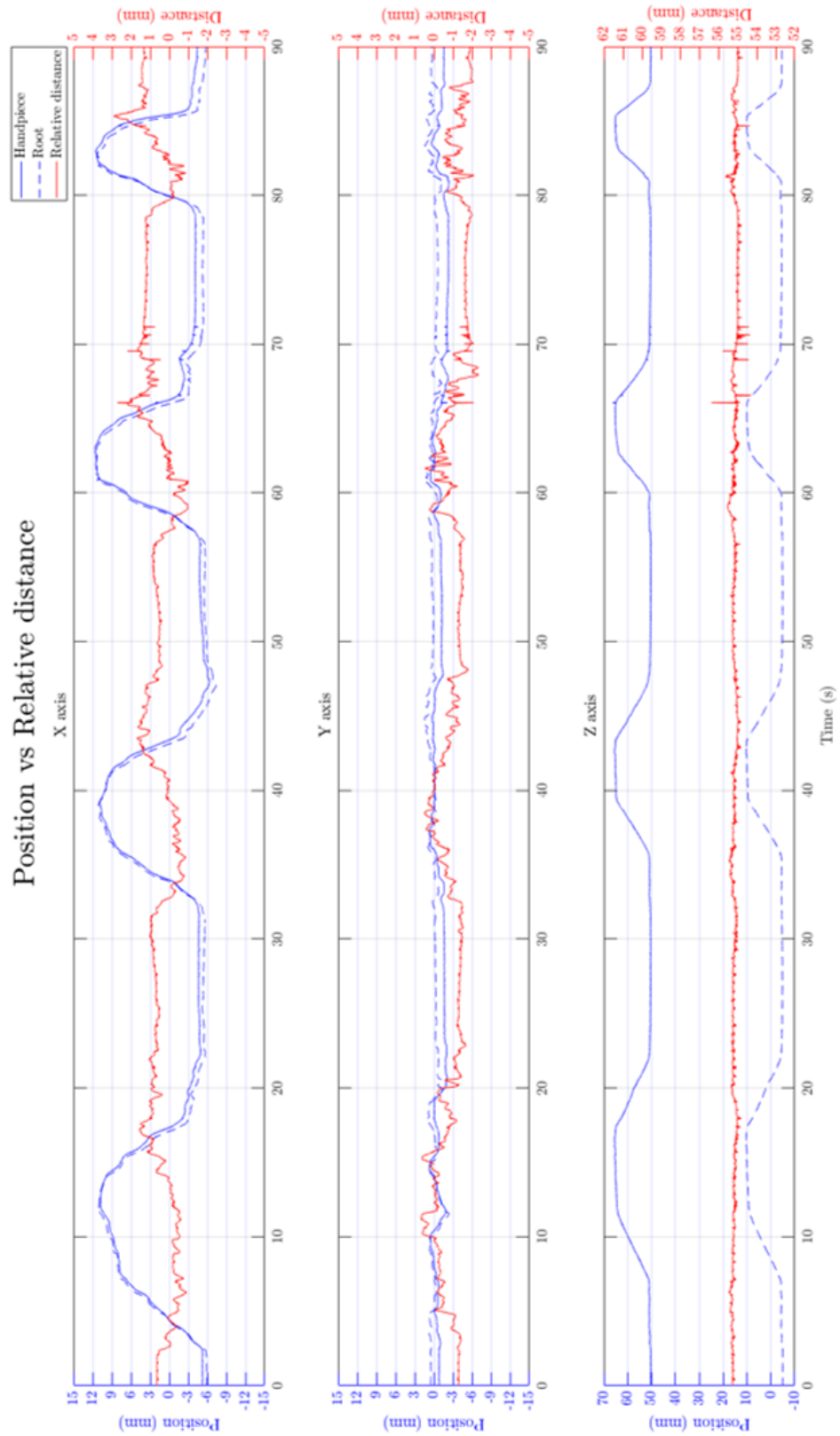


Figure 6.6: Exp 1-1: The position of handpiece and root and their relative distance

6. Experiment Results

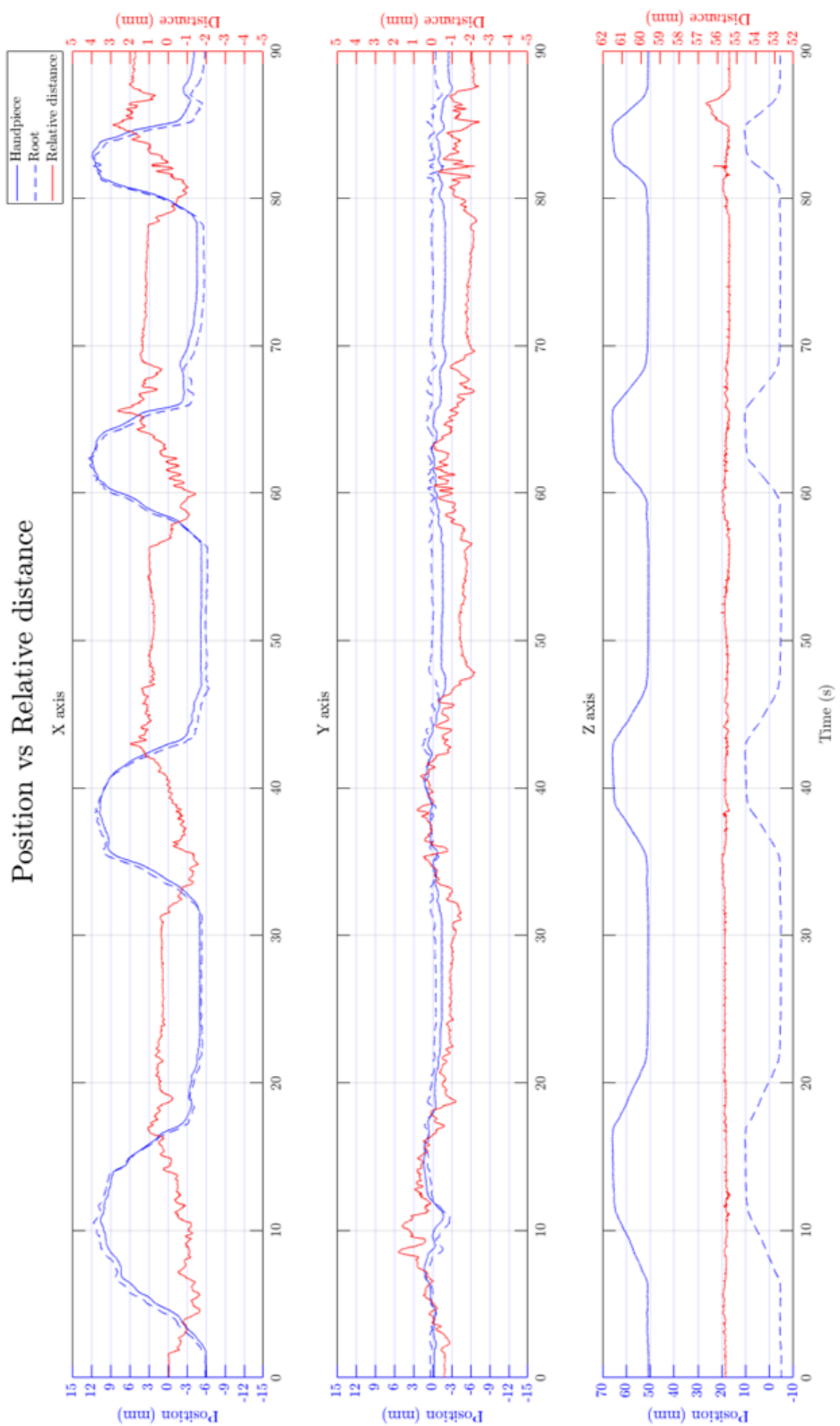


Figure 6.7: Exp 1-2: The position of handpiece and root and their relative distance

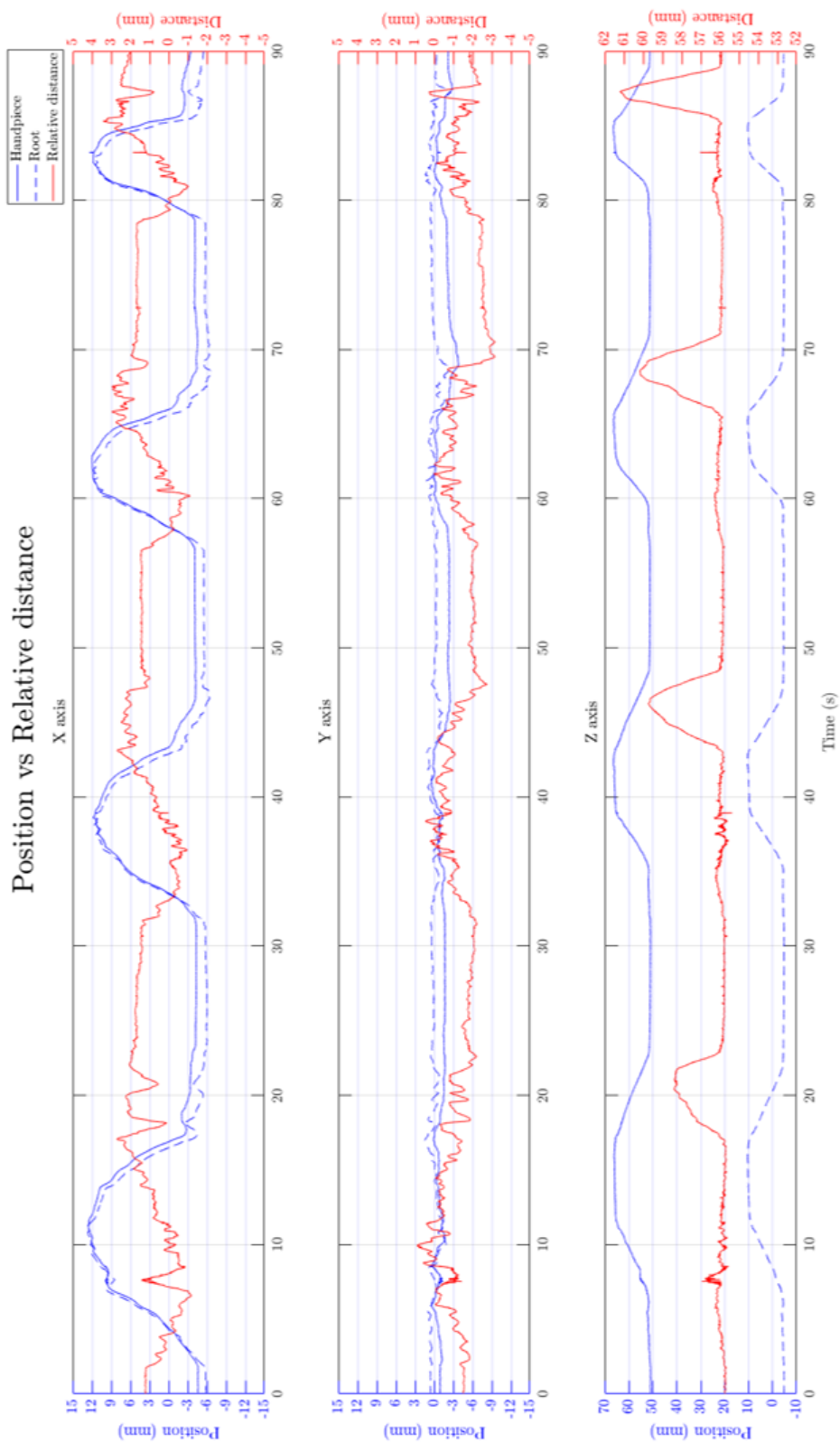


Figure 6.8: Exp 1-3: The position of handpiece and root and their relative distance

The first metric type of figure is the position of handpiece and root and their relative distance. Exp 1-1 , 1-2, and 1-3 were plotted in Fig 6.6, Fig 6.7, and Fig 6.8 and were discussed together here. First, the trajectory of the Stewart platform was analyzed. Distortion of platform moving occurred and led to difference to the position command of Stewart platform shown in Fig 6.5. Fig 6.9 shows the real platform moving simulated by the Stewart platform.

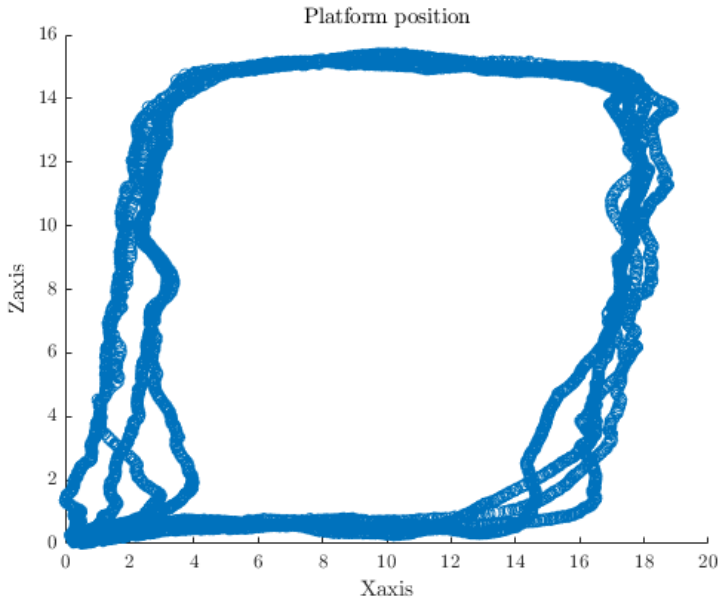


Figure 6.9: Patient moving simulated by the Stewart platform

There was a apparent distortion around 3 mm on X-axis when the platform was moving along with Z-axis. This distortion led to the fact that each cycle in the position plot on X-axis is not a trapezoid. The Stewart platform moving along with X-axis was smooth, so the position plot on Z-axis is a typical trapezoid. Therefore, the relative distance was calculated and became the most essential metric .

On X-axis we could find that there is a phase difference between the root position and the handpiece position. The main reason is that the file property is superelastic and delays the response time when the file bears a contact force.

Compared all X-axes and Y-axes from Exp 1-1 to 1-3, the maximum relative distance are all around 3 mm. This relative distance is acceptable because it came from many errors such as the motion capture system, the 3-D print support, and the flexible property of the endodontic file. On Z-axis, the maximum relative distance in Exp 1-1 approximately retains at 55 mm; in Exp 1-2, there is a ripple at around 87th second. It is due to the file leaving out of the root when the platform was moving down along with Z-axis. The file chased the root because f_z made DentiBot insert and the relative distance went back to the original offset after a few seconds. Why the file is easy to leave out of the root in Exp 1-2 and not in Exp 1-1 is the file rotation. As for Z-axis of Exp 1-3, ripples were expected because the maximum f_z was half of the previous. With the velocity is increasing, ripples are getting bigger. At 6 mm/s velocity, the maximum relative distance is around 5 mm. After around 5 seconds, it could go back to the original offset.

In conclusion, from Exp 1-1 to Exp 1-3, the maximum relative distances were all retained in an acceptable error. Despite that Exp 1-3 had a significant detachment between the endodontic file and the root, the file could track and go back to the original offset. It is worth noting that there is a distortion when the Stewart platform moves along with Z-axis, which means the force-guided alignment could track and compensate the surgical path in real-time with high performance.

6. Experiment Results

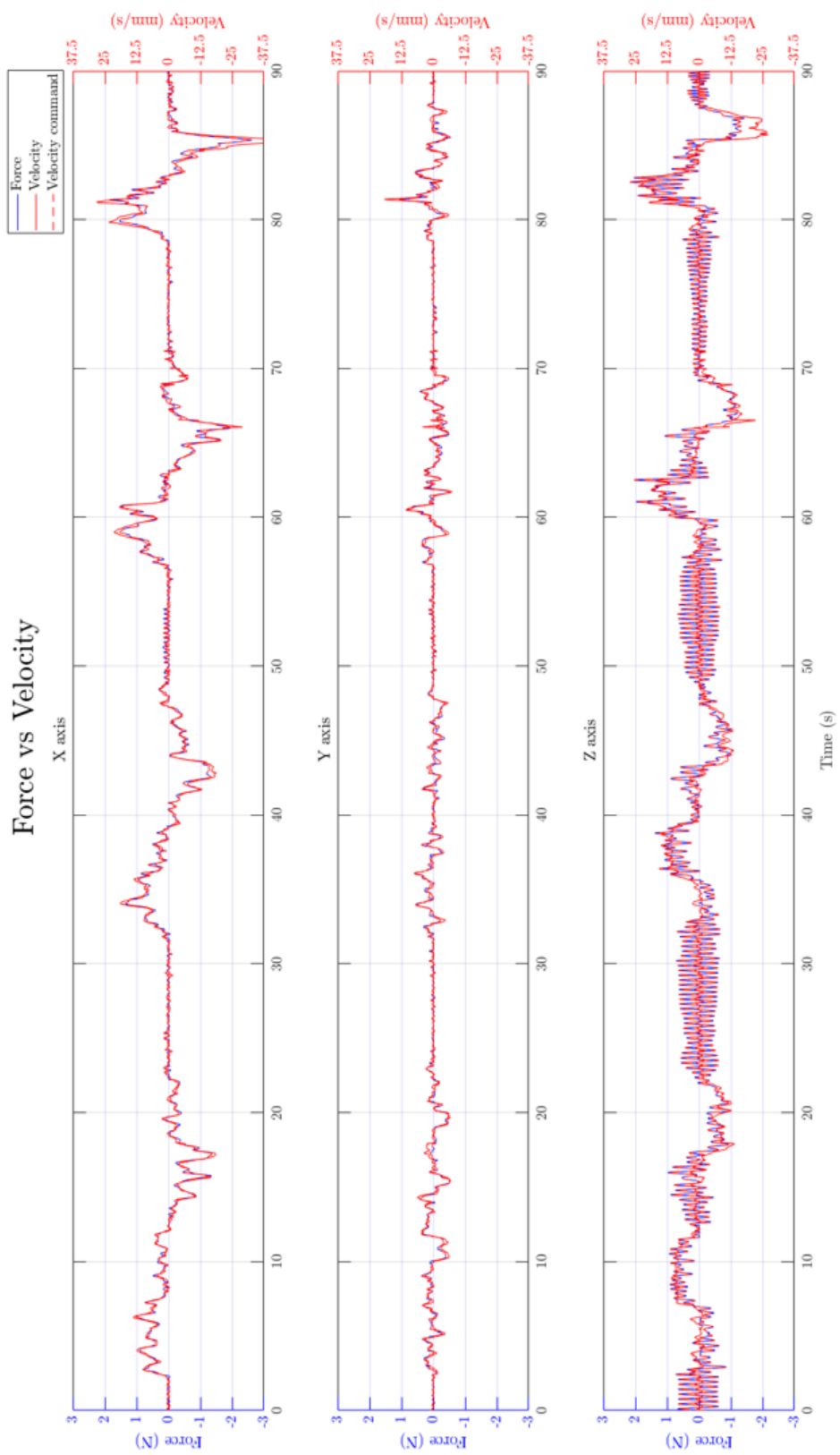


Figure 6.10: Exp 1-1: The force vs the velocity

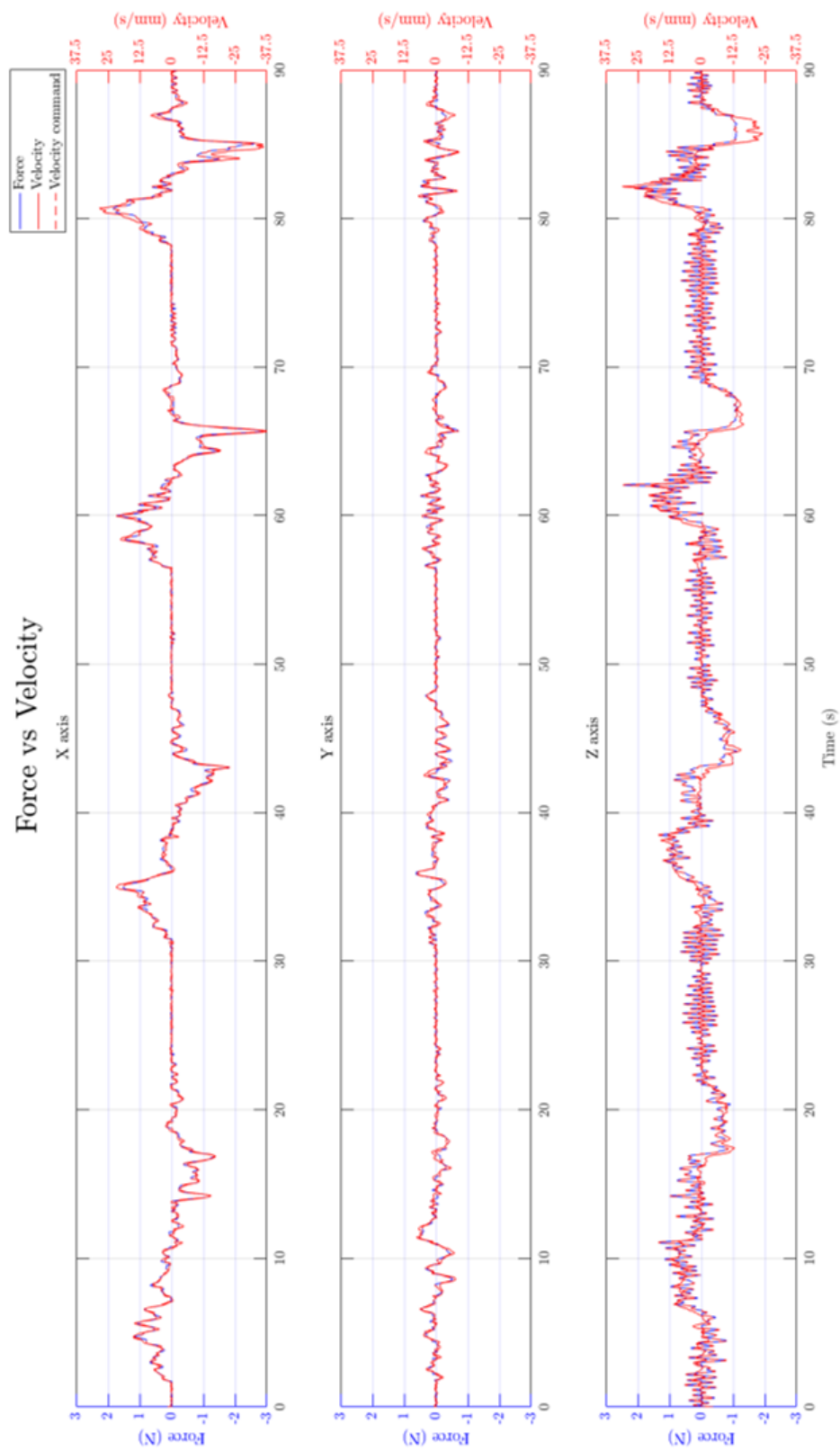


Figure 6.11: Exp 1-1: The force vs the velocity

6. Experiment Results

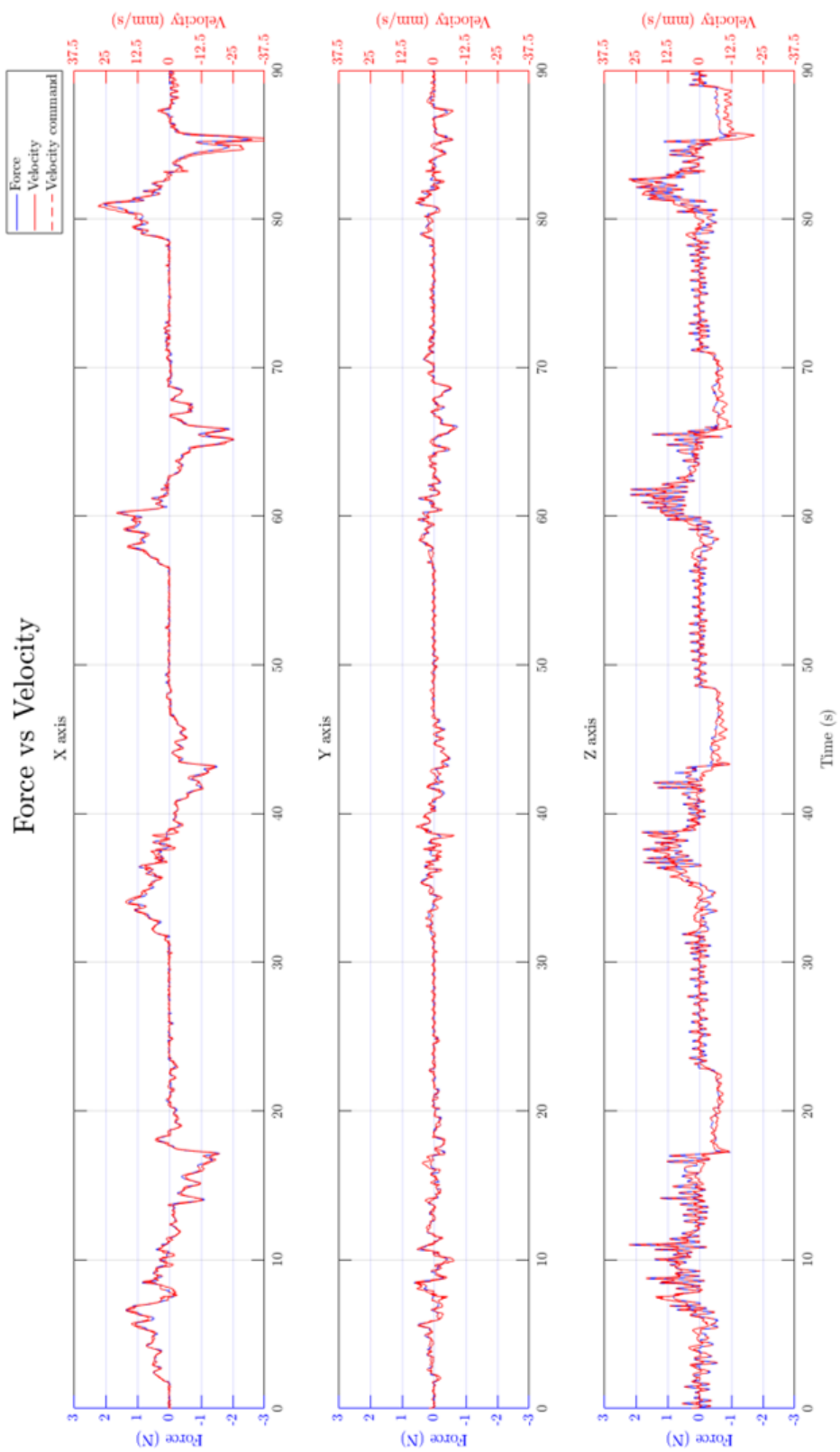


Figure 6.12: Exp 1-1: The force vs the velocity

The second metric type of figure is comparing the detected force with the command velocity and the real velocity. Exp 1-1 , 1-2, and 1-3 were plotted in Fig 6.10, Fig 6.11, and Fig 6.12 and were discussed together here. In theory, the force should match the command velocity and have a highly positive correlation to the real velocity. From Exp 1 to Exp 3, three plots are similar, overall the results compared to the theory are all correct. However, two phenomena occurred on Z-axis. The first phenomenon is that there is oscillation due to excessive velocity caused by a large value of f_z . Too fast velocity would produce excessive force than the desired force when the file contacts the root bottom and lead to an opposite move. The other phenomenon is zoomed in and shown in Fig 6.13. The difference between the command and real velocity is caused by the detachment between root and file.

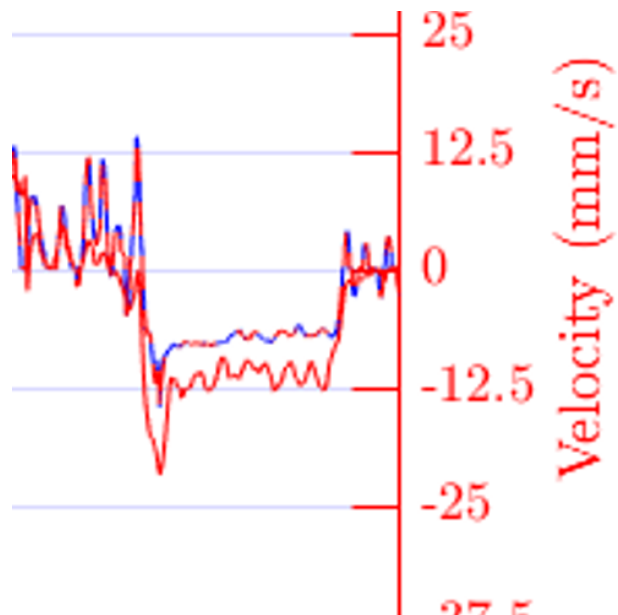


Figure 6.13: Zoom-in of Force vs Velocity on Z-axis from 80th to 90th second

6. Experiment Results

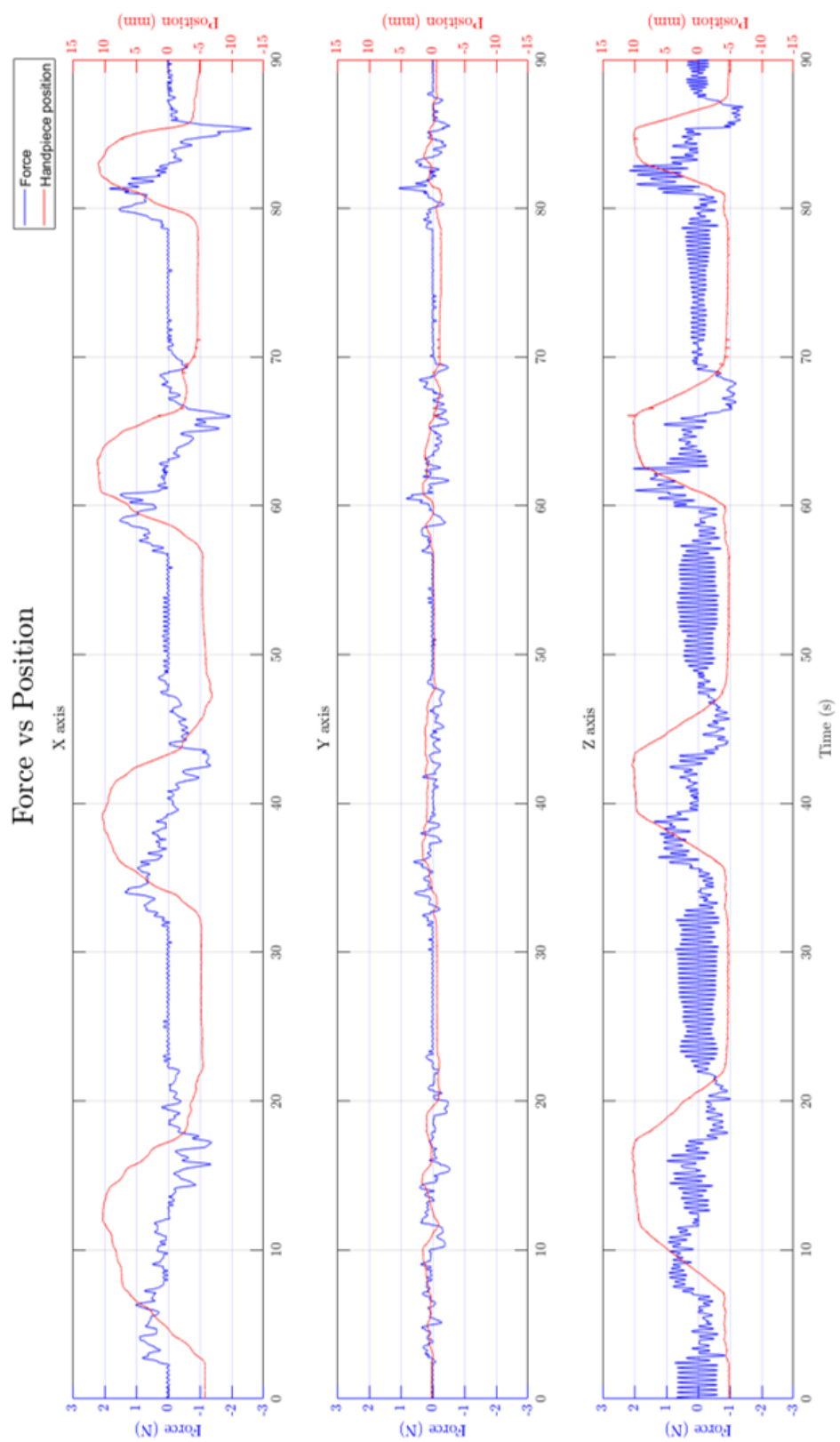


Figure 6.14: Exp 1-2: The force vs the handpiece position

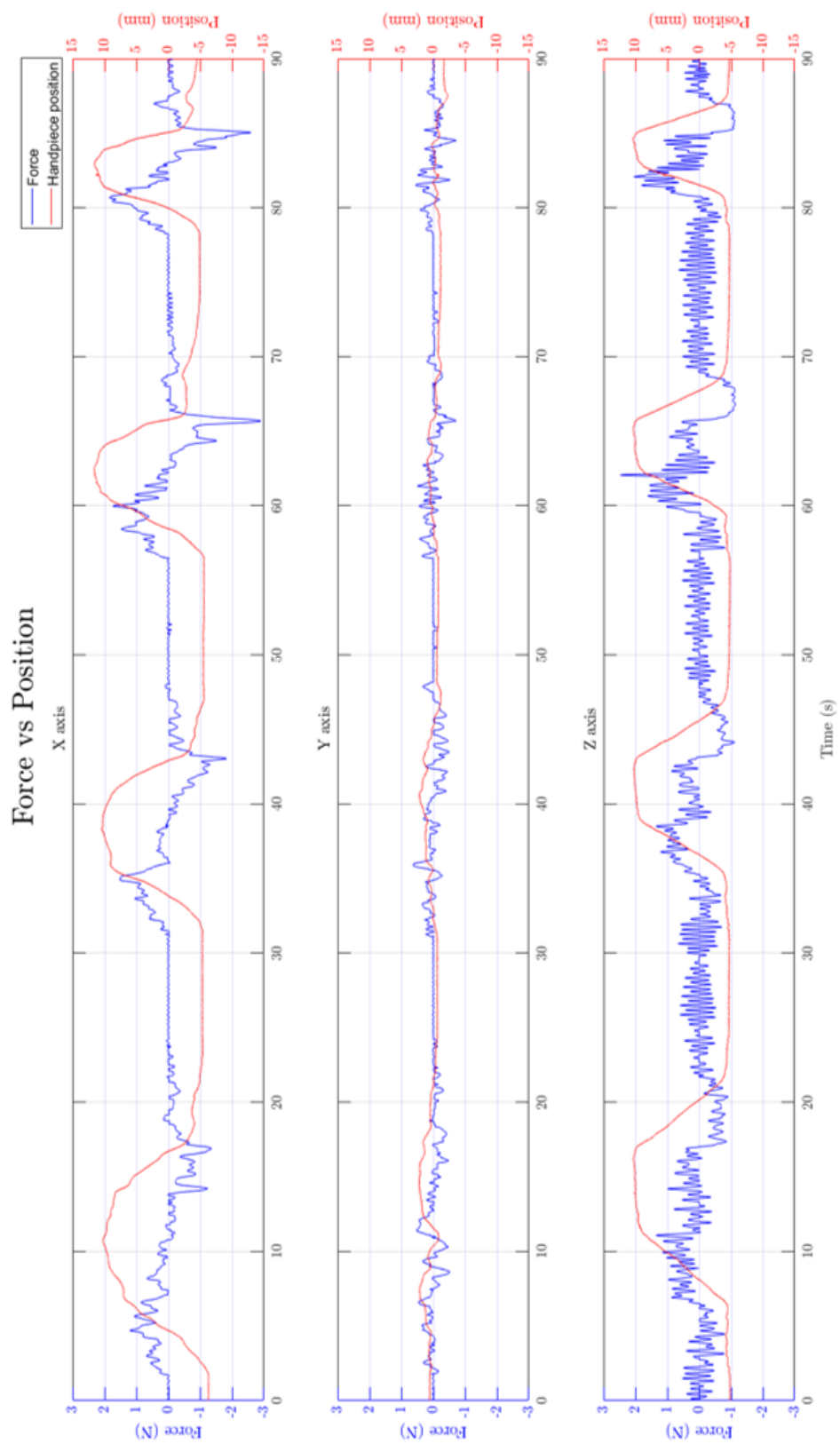


Figure 6.15: Exp 1-2: The force vs the handpiece position

6. Experiment Results

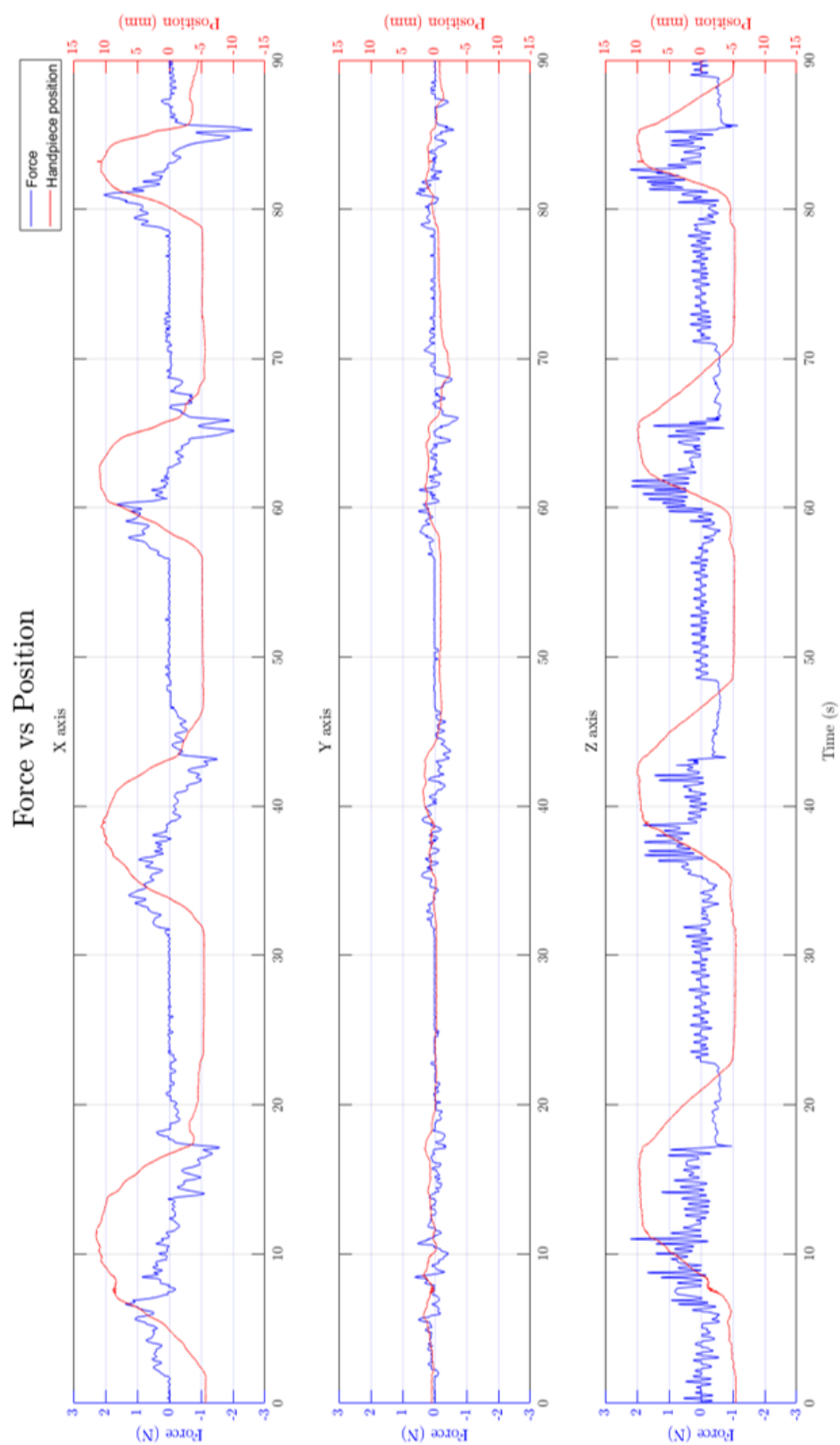


Figure 6.16: Exp 1-2: The force vs the handpiece position

The third metric type of figure is comparing the detected force with the hand-piece position. Exp 1-1 , 1-2, and 1-3 were plotted in Fig 6.14, Fig 6.15, and Fig 6.16 and were discussed together here. An oscillation occurred on Z-axis is due to excessive velocity caused by a large value of f_z . A large value of f_z means a faster inserting velocity. Once the file contacts the bottom of root, the opposite force is produced and detected by the F/T sensor. The contact velocity is faster, then the opposite force is larger. Therefore, if the opposite force is larger than the desired force, the DentiBot will move to the opposite direction. However, the opposite move will decrease the detected force and then make the DentiBot move forward again. That is why the oscillation occurs.

Conclusion of Force-Guided Alignment Experiment

To conclude the first experiment 1, the maximum relative distances on X-axis and Y-axis were all retained within 3 mm. 3 mm was an acceptable error because it could be the result of the inaccurate 3-D print support, the flexible property of endodontic files, and the motion capture system error. Despite that Exp 1-3 had a significant detachment between the endodontic file and the root, the file could track and go back to the original offset. Patient moving within 15 mm is proved to be allowed because the force-guided alignment could track and compensate the surgical path in real-time with low error. Therefore, the experiment result has proved the feasibility of combining force-guided alignment, file feedrate control and patient tracking.

6.3 Pre-Clinical Evaluation

We have verified the feasibility of combining force-guided alignment, file feedrate control. In what follows, an algorithm that combines all functions including force-guided alignment, patient tracking, inverse rotation control, and feed control were implemented in the pre-clinical trial as shown in Fig 6.17.

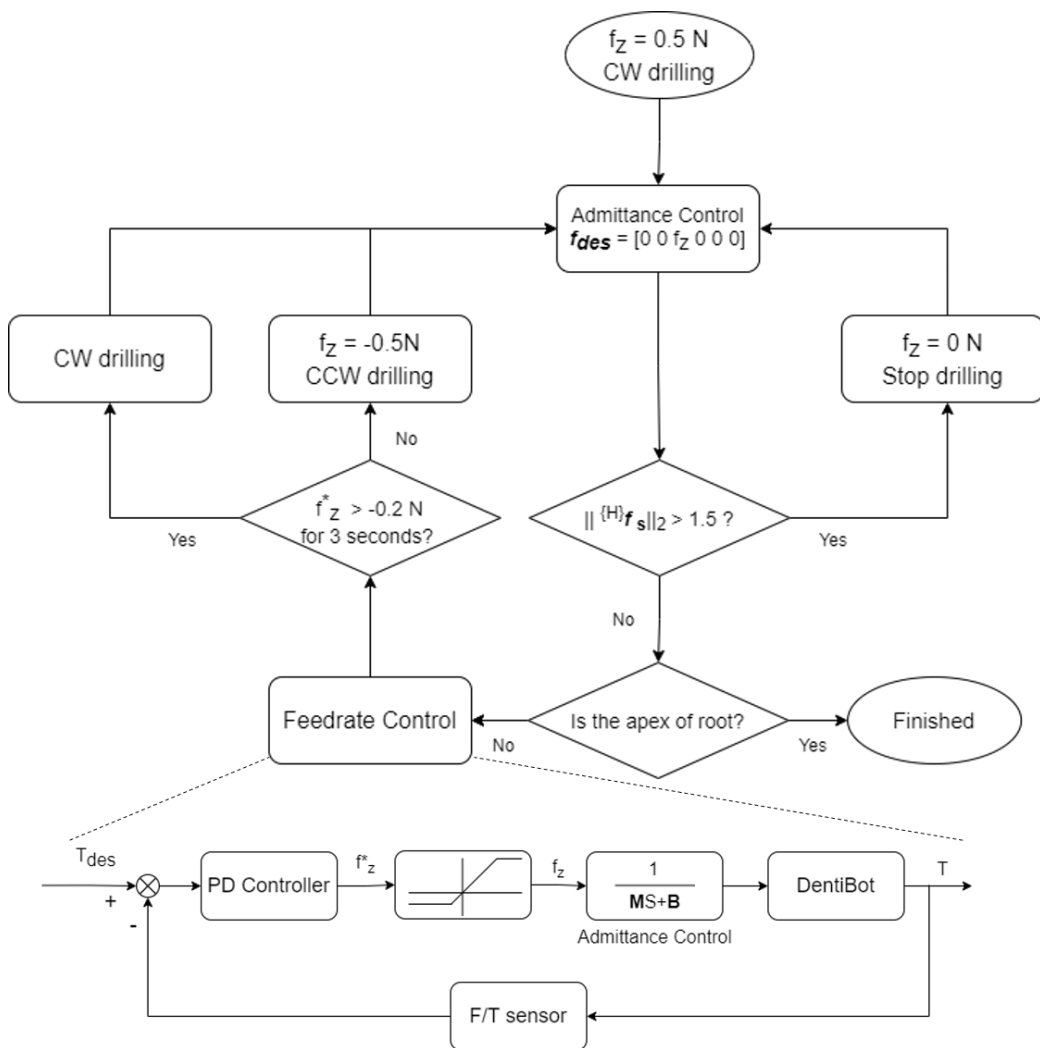


Figure 6.17: Algorithm for robot-assisted endodontic treatment

The metrics of the pre-clinical trial were completeness of root preparation and whether instrument fracture happened. To compare the completeness before and after the surgery, acrylic root phantoms were involved. The acrylic root phantoms were widely used in the operative technique classroom to simulate the clinical situations. Intern dentists practised the endodontic techniques with acrylic root phantoms. To simulate and visualize the pulp in roots, red pigment was filled with roots shown in Fig 6.18. The top of the model is a cone shape and is not included to calculate the completeness because the cone area is not the drilling area. Therefore, the red line depicted in the figure is the calculated length.

Hence, completeness is defined as

$$\text{Completeness} = \frac{R_b - R_a}{R_b} \times 100\% \quad (6.1)$$

where R_b denotes the red area before the treatment. R_a denotes the remained red area after the treatment.

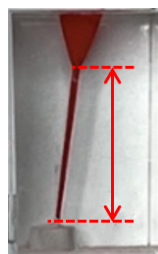


Figure 6.18: Acrylic root phantom used in operative technique practice

Note that the acrylic root phantoms were all different due to manufacture process. Conditions of the acrylic root phantoms might be straight, titled, or even curve.

Six root models, A to F, were divided into two groups. The desired torque T_{des} in file feedrate control was set 40 and implemented in A, B, and C. On the other hand, T_{des} was set 50 in D, E, and F. Each model was treated for two times. The first round took 300 seconds and the second round took 200 seconds.

Result

In Fig 6.19, six root models before and after treatment are compared. There is few remained red pigment within roots. Besides, the roots were all shaped to cone shapes without ledging. Ledging is an irregular platform caused by an inappropriate operation such as too much force while drilling. Once ledging happens, it would impede the endodontic files to the apex. The results without ledging proved that force-guided alignment was effective to adjust the surgical path in real-time.

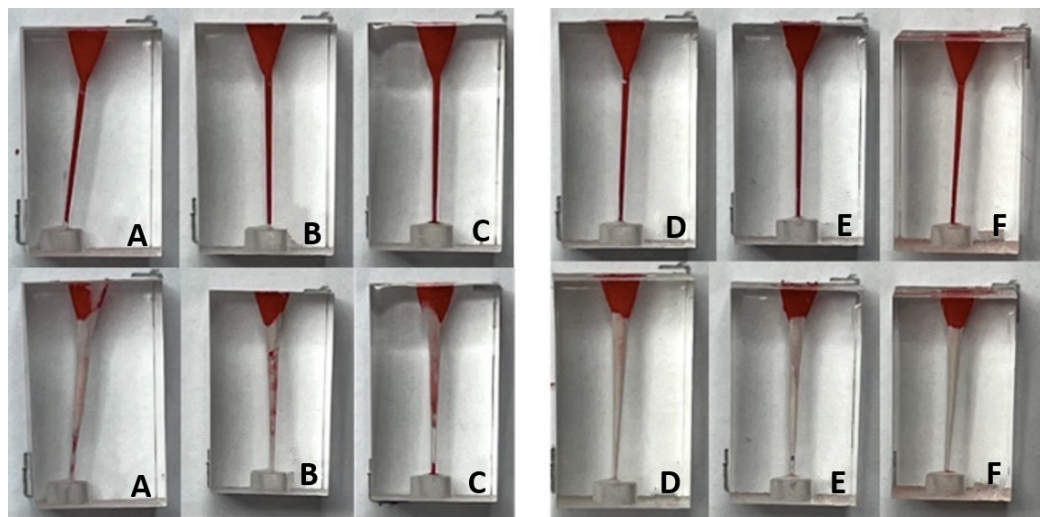


Figure 6.19: Exp 2: Roots before and after drilling for two times. T_{des} were set 40 in A,B,C and 50 in D,E,F

To dissect the completeness, the root images were evaluated by image processing and shown in Table 6.5. The average completeness of A, B, C is 88.41% and the average completeness of D, E, FC is 99.2%. It means that T_{des} 50 below the maximum file bearing torque 62 had higher completeness than T_{des} 40. However, no matter T_{des} was 40 or 50, it could both achieve high performance in root preparation and prevent instrument fracture.

Table 6.5: Results of pre-clinical evaluation

Number	Preoperative	Postoperative	Completeness	Instrument
	Red Area (pixel)	Red Area (pixel)		Fracture
A	15652	795	94.92%	No
B	17316	2418	86.04%	No
C	17403	2738	84.27%	No
D	16114	53	99.67%	No
E	17047	185	98.91%	No
F	18482	180	99.03%	No

Conclusion of pre-clinical evaluation

In this experiment, the performance of root preparation using our robot was demonstrated. No ledging in all postoperative acrylic root phantoms proved that force-guided alignment could adjust the surgical path in real-time. Preoperative and Postoperative root models were evaluated their completeness and compared. The results verified the feasibility of robot-assisted endodontic treatment.

Chapter 7

Conclusions and Future works

An endodontic treatment is a challenging surgery for dentists due to complex conditions of teeth. Therefore, building a robot-assisted system for the endodontic robot requires comprehensive consideration on whole surgery procedures. Review the section 1.4, we advocated the four parts of the project prospect. We highlight two main parts of the prospect and have proved the feasibility of our proposed approaches. The whole work of the thesis is concluded in this chapter.

7.1 Conclusions

Nowadays, despite that there are more and more dental robots springing up, there are still few teams specific to endodontic treatment. In view of this, our team has built the robot-assisted system, Dentibot, composed of a 6-DoF robot arm, a 6-DoF F/T sensor, and a modified handpiece. System integration solutions between the above devices are reviewed. The DentiBot can assist dentists in performing endodontic treatment as a consequence of the following functions.

Moreover, admittance control is implemented to enable the dentist to move the DentiBot above an infected tooth. Also, a framework based on admittance control for robot alignment regarding the position and orientation of the root

canal is presented. "Dragging Mode" and "Self-Alignment Mode" are separately implemented for the above functions.

Lastly, instrument fracture is a serious problem for dentists. It will even lead to a medical dispute. With the torque monitoring system, file feedrate control is applied to reduce the possibility of instrument fracture.

Experiments indicated that the above functions had good performances on force-guided alignment and file feedrate control. It has proven the feasibility in technical and clinical perspectives. Undoubtedly, the DentiBot can help dentists perform better clinical results.

7.2 Discussion and Future Works

The thesis is the pioneer of the endodontic project. Despite that the thesis develops the DentiBot and presents the above functions, there are undoubtedly some remained works and rooms for improvement on the modified hardware and functions. The modified handpiece made by 3D-print is not durable for time-consuming endodontic treatment. It is necessary to do machining for more stable results.

In the thesis, we hypothesize that a dentist moves the DentiBot above the root, then the DentiBot does the "Cleaning" procedure. However, sometimes there is not only one root in the tooth. For instance, there are three to four roots in a molar. Therefore, we wish that the DentiBot will have the ability to search all root canals after the dentist moves the DentiBot above the infected tooth.

On top of that, we proposed the alignment method while the DentiBot does drilling. It not only aligns with the root path but also with patient moving. However, the patient tracking belongs to a minor range movement. Therefore, the DentiBot is expected to be applied to patient tracking with large movement via string potentiometers in the future.

Appendix

Appendix A Forward Kinematics

$${}^0\mathbf{T} = {}^0\mathbf{T} \cdot {}^1_2\mathbf{T} \cdot {}^2_3\mathbf{T} \cdot {}^3_4\mathbf{T} \cdot {}^4_5\mathbf{T} \cdot {}^5_6\mathbf{T} = \begin{bmatrix} {}^0\mathbf{R}_{3 \times 3} & {}^0\mathbf{p}_{6_{\text{org}}} \\ 0_{1 \times 3} & 1 \end{bmatrix} = \begin{bmatrix} t_{11} & t_{12} & t_{13} & t_{14} \\ t_{21} & t_{22} & t_{23} & t_{24} \\ t_{31} & t_{32} & t_{33} & t_{34} \\ 0 & 0 & 0 & 1 \end{bmatrix}$$

$$t_{11} = -S_6(C_4S_1 + S_4(C_1S_3 - C_2 - C_1C_3S_2)) - C_6(C_5(S_1S_4 - C_4(C_1S_3 - C_2 - C_1C_3S_2)))$$

$$-C_6(C_5(S_1S_4 - C_4(C_1S_3 - C_2 - C_1C_3S_2)) - S_5(C_1C_3 - C_2 + C_1S_2S_3))$$

$$t_{12} = S_6(C_5(S_1S_4 - C_4(C_1S_3 - C_2 - C_1C_3S_2)) - S_5(C_1C_3 - C_2 + C_1S_2S_3))$$

$$-C_6(C_4S_1 + S_4(C_1S_3 - C_2 - C_1C_3S_2))$$

$$t_{13} = -S_5(S_1S_4 - C_4(C_1S_3 - C_2 - C_1C_3S_2)) - C_5(C_1C_3 - C_2 + C_1S_2S_3)$$

$$t_{14} = 135C_1S_2 - 70S_5(S_1S_4 - C_4(C_1S_3 - C_2 - C_1C_3S_2)) - 70C_5(C_1C_3 - C_2$$

$$+ C_1S_2S_3) - 120C_1C_3 - C_2 - 120C_1S_2S_3 - 38C_1S_3 - C_2 + 38C_1C_3S_2$$

$$t_{21} = S_6(C_1C_4 + S_4(C_3S_2S_1 - S_1S_3 - C_2)) + C_6(C_5(C_1S_4 - C_4(C_3S_2S_1$$

$$- S_1S_3 - C_2)) + S_5(C_3S_1 - C_2 + S_2S_1S_3))$$

$$t_{22} = C_6(C_1C_4 + S_4(C_3S_2S_1 - S_1S_3 - C_2)) - S_6(C_5(C_1S_4 - C_4(C_3S_2S_1$$

$$- S_1S_3 - C_2)) + S_5(C_3S_1 - C_2 + S_2S_1S_3))$$

$$t_{23} = S_5(C_1S_4 - C_4(C_3S_2S_1 - S_1S_3 - C_2)) - C_5(C_3S_1 - C_2 + S_2S_1S_3)$$

$$t_{24} = 135S_2S_1 + 70S_5(C_1S_4 - C_4(C_3S_2S_1 - S_1S_3 - C_2)) - 70C_5(C_3S_1 - C_2$$

$$+ S_2 S_1 S_3) + 38 C_3 S_2 S_1 - 120 C_3 S_1 - C_2 - 120 S_2 S_1 S_3 - 38 S_1 S_3 - C_2$$

$$\begin{aligned} t_{31} = & \ C_6(S_5(C_3 S_2 - S_3 - C_2) + C_4 C_5(C_3 - C_2 + S_2 S_3)) - S_4 S_6(C_3 - C_2 \\ & + S_2 S_3) \end{aligned}$$

$$\begin{aligned} t_{32} = & \ -S_6(S_5(C_3 S_2 - S_3 - C_2) + C_4 C_5(C_3 - C_2 + S_2 S_3)) - C_6 S_4(C_3 - C_2 \\ & + S_2 S_3) \end{aligned}$$

$$t_{33} = C_4 S_5(C_3 - C_2 + S_2 S_3) - C_5(C_3 S_2 - S_3 - C_2)$$

$$\begin{aligned} t_{34} = & \ 120 S_3 - C_2 - 120 C_3 S_2 - 38 C_3 - C_2 - 38 S_2 S_3 - 135 - C_2 \\ & - 70 C_5(C_3 S_2 - S_3 - C_2) + 70 C_4 S_5(C_3 - C_2 + S_2 S_3) + 135 \end{aligned}$$

Appendix B Jacobian Matrix

Jg0

$$j_{g0,21} = 135 C_1 S_2 - 120 C_1 S_2 S_3 - 70 S_1 S_4 S_5 + 120 C_1 C_2 C_3 + 38 C_1 C_2 S_3$$

$$+ 38 C_1 C_3 S_2 + 70 C_1 C_2 C_3 C_5 - 70 C_1 C_5 S_2 S_3 - 70 C_1 C_2 C_4 S_3 S_5$$

$$- 70 C_1 C_3 C_4 S_2 S_5$$

$$j_{g0,22} = -S_1(120 C_2 S_3 - 38 C_2 C_3 - 135 C_2 + 120 C_3 S_2 + 38 S_2 S_3 + 70 C_2 C_5 S_3$$

$$+ 70 C_3 C_5 S_2 + 70 C_2 C_3 C_4 S_5 - 70 C_4 S_2 S_3 S_5)$$

$$j_{g0,23} = -2 S_1(60 C_2 S_3 - 19 C_2 C_3 + 60 C_3 S_2 + 19 S_2 S_3 + 35 C_2 C_5 S_3$$

$$+ 35 C_3 C_5 S_2 + 35 C_2 C_3 C_4 S_5 - 35 C_4 S_2 S_3 S_5)$$

$$j_{g0,24} = 70 S_5(C_1 C_4 + C_2 S_1 S_3 S_4 + C_3 S_1 S_2 S_4)$$

$$j_{g0,25} = -70 C_5(C_2 C_4 S_1 S_3 - C_1 S_4 + C_3 C_4 S_1 S_2) - 70 C_{34} S_1 S_5$$

$$j_{g0,26} = 0$$

$$j_{g0,31} = 0$$

$$j_{g0,32} = 120S_2S_3 - 120C_2C_3 - 38C_2S_3 - 38C_3S_2 - 135S_2 + 70C_5S_2S_3$$

$$- 70C_2C_3C_5 + 70C_2C_4S_3S_5 + 70C_3C_4S_2S_5$$

$$j_{g0,33} = 120S_2S_3 - 38C_2S_3 - 38C_3S_2 - 120C_2C_3 + 70C_5S_2S_3 - 70C_2C_3C_5$$

$$+ 70C_2C_4S_3S_5 + 70C_3C_4S_2S_5$$

$$j_{g0,34} = 70C_{34}S_4S_5$$

$$j_{g0,35} = 70S_{34}S_5 - 70C_{34}C_4C_5$$

$$j_{g0,36} = 0$$

$$j_{g0,41} = \theta_4S_1S_2S_3 - \theta_3C_1 - \theta_5C_1C_4 - \theta_4C_2C_3S_1 - \theta_6C_1S_4S_5 - \theta_2C_1$$

$$- \theta_6C_2C_3C_5S_1 - \theta_5C_2S_1S_3S_4 - \theta_5C_3S_1S_2S_4 + \theta_6C_5S_1S_2S_3$$

$$\theta_6C_2C_4S_1S_3S_5 + \theta_6C_3C_4S_1S_2S_5$$

$$j_{g0,42} = \theta_5C_1C_2C_3S_4 - \theta_4C_1C_2S_3 - \theta_4C_1C_3S_2 - S_1 - \theta_6C_1C_2C_5S_3$$

$$- \theta_6C_1C_3C_5S_2 - \theta_5C_1S_2S_3S_4 - \theta_6C_1C_2C_3C_4S_5 + \theta_6C_1C_4S_2S_3S_5$$

$$j_{g0,43} = \theta_5C_1C_2C_3S_4 - \theta_4C_1C_2S_3 - \theta_4C_1C_3S_2 - S_1 - \theta_6C_1C_2C_5S_3$$

$$- \theta_6C_1C_3C_5S_2 - \theta_5C_1S_2S_3S_4 - \theta_6C_1C_2C_3C_4S_5 + \theta_6C_1C_4S_2S_3S_5$$

$$j_{g0,44} = \theta_5(S_1S_4 + C_1C_2C_4S_3 + C_1C_3C_4S_2) - C_1S_2S_3 + C_1C_2C_3$$

$$+ \theta_6S_5(C_1C_2S_3S_4 - C_4S_1 + C_1C_3S_2S_4)$$

$$j_{g0,45} = -C_4S_1 - \theta_6(C_5(S_1S_4 - C_4(C_1S_3 - C_2 - C_1C_3S_2)) - S_5(C_1C_3$$

$$- C_2 + C_1S_2S_3)) - S_4(C_1S_3 - C_2 - C_1C_3S_2)$$

$$j_{g0,46} = C_{34}C_1C_5 - S_5(S_1S_4 + C_1C_2C_4S_3 + C_1C_3C_4S_2)$$

$$j_{g0,51} = \theta_4C_1C_2C_3 - \theta_3S_1 - \theta_5C_4S_1 - \text{theta2}S_1 - \theta_4C_1S_2S_3 - \theta_6S_1S_4S_5$$

$$+ \theta_6C_1C_2C_3C_5 + \theta_5C_1C_2S_3S_4 + \theta_5C_1C_3S_2S_4 - \theta_6C_1C_5S_2S_3$$

$$-\theta_6 C_1 C_2 C_4 S_3 S_5 - \theta_6 C_1 C_3 C_4 S_2 S_5$$

$$j_{g0,52} = C_1 - \theta_4 C_2 S_1 S_3 - \theta_4 C_3 S_1 S_2 + \theta_5 C_2 C_3 S_1 S_4 - \theta_6 C_2 C_5 S_1 S_3$$

$$-\theta_6 C_3 C_5 S_1 S_2 - \theta_5 S_1 S_2 S_3 S_4 - \theta_6 C_2 C_3 C_4 S_1 S_5 + \theta_6 C_4 S_1 S_2 S_3 S_5$$

$$j_{g0,53} = C_1 - \theta_4 C_2 S_1 S_3 - \theta_4 C_3 S_1 S_2 + \theta_5 C_2 C_3 S_1 S_4 - \theta_6 C_2 C_5 S_1 S_3$$

$$-\theta_6 C_3 C_5 S_1 S_2 - \theta_5 S_1 S_2 S_3 S_4 - \theta_6 C_2 C_3 C_4 S_1 S_5 + \theta_6 C_4 S_1 S_2 S_3 S_5$$

$$j_{g0,54} = \theta_5 (C_2 C_4 S_1 S_3 - C_1 S_4 + C_3 C_4 S_1 S_2) + \theta_6 S_5 (C_1 C_4 + C_2 S_1 S_3 S_4$$

$$+ C_3 S_1 S_2 S_4) - S_1 S_2 S_3 + C_2 C_3 S_1$$

$$j_{g0,55} = C_1 C_4 + S_{34} S_1 S_4 - \theta_6 C_{34} S_1 S_5 + \theta_6 C_1 C_5 S_4 - \theta_6 C_2 C_4 C_5 S_1 S_3$$

$$-\theta_6 C_3 C_4 C_5 S_1 S_2$$

$$j_{g0,56} = C_{34} C_5 S_1 - S_5 (C_2 C_4 S_1 S_3 - C_1 S_4 + C_3 C_4 S_1 S_2)$$

$$j_{g0,61} = 1$$

$$j_{g0,62} = \theta_6 S_{34} C_4 S_5 - \theta_6 C_{34} C_5 - \theta_5 S_{34} S_4 - \theta_4 C_{34}$$

$$j_{g0,63} = \theta_6 S_{34} C_4 S_5 - \theta_6 C_{34} C_5 - \theta_5 S_{34} S_4 - \theta_4 C_{34}$$

$$j_{g0,64} = \theta_5 C_2 C_3 C_4 - C_3 S_2 - C_2 S_3 - \theta_5 C_4 S_2 S_3 + \theta_6 C_2 C_3 S_4 S_5 - \theta_6 S_2 S_3 S_4 S_5$$

$$j_{g0,65} = \theta_6 (S_{34} S_5 - C_{34} C_4 C_5) + C_{34} S_4$$

$$j_{g0,66} = -S_{34} C_5 - C_{34} C_4 S_5$$

Jg6

$$j_{g6,11} = 135 C_4 S_2 S_6 + 120 C_2 C_3 C_4 S_6 + 70 C_2 C_3 C_6 S_4 + 38 C_2 C_4 S_3 S_6$$

$$+ 38 C_3 C_4 S_2 S_6 + 135 C_5 C_6 S_2 S_4 - 120 C_4 S_2 S_3 S_6 - 70 C_6 S_2 S_3 S_4$$

$$- 70 C_2 S_3 S_5 S_6 - 70 C_3 S_2 S_5 S_6 + 70 C_2 C_3 C_4 C_5 S_6 + 120 C_2 C_3 C_5 C_6 S_4$$

$$+ 38C_2C_5C_6S_3S_4 + 38C_3C_5C_6S_2S_4 - 70C_4C_5S_2S_3S_6$$

$$- 120C_5C_6S_2S_3S_4$$

$$j_{g6,12} = 70C_4C_6 - 38C_6S_5 - 120S_4S_6 - 70C_5S_4S_6 + 135S_3S_4S_6 + 120C_4C_5C_6$$

$$- 135C_3C_6S_5 - 135C_4C_5C_6S_3$$

$$j_{g6,13} = 70C_4C_6 - 38C_6S_5 - 120S_4S_6 - 70C_5S_4S_6 + 120C_4C_5C_6$$

$$j_{g6,14} = 70S_5S_6$$

$$j_{g6,15} = 70C_6$$

$$j_{g6,16} = 0$$

$$j_{g6,21} = 135C_4C_6S_2 + 120C_2C_3C_4C_6 + 38C_2C_4C_6S_3 + 38C_3C_4C_6S_2$$

$$- 70C_2C_3S_4S_6 - 120C_4C_6S_2S_3 - 70C_2C_6S_3S_5 - 70C_3C_6S_2S_5$$

$$- 135C_5S_2S_4S_6 + 70S_2S_3S_4S_6 + 70C_2C_3C_4C_5C_6 - 120C_2C_3C_5S_4S_6$$

$$- 70C_4C_5C_6S_2S_3 - 38C_2C_5S_3S_4S_6 - 38C_3C_5S_2S_4S_6$$

$$+ 120C_5S_2S_3S_4S_6$$

$$j_{g6,22} = 38S_5S_6 - 120C_6S_4 - 70C_4S_6 + 135C_6S_3S_4 + 135C_3S_5S_6$$

$$- 120C_4C_5S_6 - 70C_5C_6S_4 + 135C_4C_5S_3S_6$$

$$j_{g6,23} = 38S_5S_6 - 120C_6S_4 - 70C_4S_6 - 120C_4C_5S_6 - 70C_5C_6S_4$$

$$j_{g6,24} = 70C_6S_5$$

$$j_{g6,25} = -70S_6$$

$$j_{g6,26} = 0$$

Reference

- [1] “The ministry of health and welfare,” 2018, <https://dep.mohw.gov.tw/dos/cp-1735-3245-113.html>. 1
- [2] “The acadamy of endodontology,” 2021, <http://www.aeroc.org.tw/about/>. 1
- [3] “Root canal procedure, tower endodontics,” 2020, <https://www.towerendodontics.com/find-out-more-about-our-services/introduction/>. 3
- [4] G. Kim, H. Seo, S. Im, D. Kang, and S. Jeong, “A study on simulator of human-robot cooperative manipulator for dental implant surgery,” *2009 IEEE International Symposium on Industrial Electronics*, pp. 2159–2164, 2009. 4, 12, 13
- [5] J. Li, Z. Shen, W. Xu, W. Y. Lam, R. T. C. Hsung, E. H. Pow, K. Kosuge, and Z. Wang, “A compact dental robotic system using soft bracing technique,” *IEEE Robotics and Automation Letters*, vol. 4, pp. 1271–1278, 2019. 4, 11, 12
- [6] “Yomi, neocis,” 2017, <https://www.neocis.com/>. 4, 15
- [7] J. Dong, S. Hong, and G. Hesselgren, “Wip: a study on the development of endodontic micro robot,” in *Proceedings of the 2006 IJME-INTERTECH Conference*. Citeseer, 2006. 4, 16, 17, 18

- [8] B. Sattapan, G. J. Nervo, J. E. Palamara, and H. H. Messer, “Defects in rotary nickel-titanium files after clinical use,” *Journal of Endodontics*, vol. 26, no. 3, pp. 161–165, 2000. [5](#), [65](#)
- [9] M. Rawtiya, K. Verma, P. Sethi, and K. Loomba, “Application of robotics in dentistry,” *Indian J Dent Adv*, vol. 6, no. 4, pp. 1700–1706, 2014. [11](#)
- [10] P. Ahmad, M. K. Alam, A. Aldajani, A. Alahmari, A. Alanazi, M. Stoddart, and M. G. Sghaireen, “Dental robotics: A disruptive technology,” *Sensors*, vol. 21, no. 10, 2021. [11](#)
- [11] B. D. Bhat, S. Bhandary, R. Naik, D. Shetty *et al.*, “Robotics in dentistry: Fiction or reality,” *Journal of Dental Research and Review*, vol. 4, no. 3, p. 67, 2017. [11](#)
- [12] Z. Haidar, “Autonomous robotics: A fresh era of implant dentistry... is a reality!” *Journal of Oral Research*, vol. 6, no. 9, pp. 230–231, 2017. [11](#)
- [13] Y. Wu, F. Wang, S. Fan, and J. K.-F. Chow, “Robotics in dental implantology,” *Oral and Maxillofacial Surgery Clinics*, vol. 31, no. 3, pp. 513–518, 2019. [11](#)
- [14] T. Iijima, T. Matsunaga, T. Shimono, K. Ohnishi, S. Usuda, and H. Kawana, “Development of a multi dof haptic robot for dentistry and oral surgery,” in *2020 IEEE/SICE International Symposium on System Integration (SII)*, 2020, pp. 52–57. [12](#), [13](#)

- [15] S. L. Bolding and U. N. Reebye, “Accuracy of haptic robotic guidance of dental implant surgery for completely edentulous arches,” *The Journal of prosthetic dentistry*, 2021. 13
- [16] ——, “Accuracy of haptic robotic guidance of dental implant surgery for completely edentulous arches,” *The Journal of Prosthetic Dentistry*, 2021. 13
- [17] “Implant surgery with robotic guidance – digital workflows for patient care,” 2019, <https://www.oralhealthgroup.com/features/implant-surgery-with-robotic-guidance-digital-workflows-for-patient-care/>. 14, 15
- [18] H. Everett, “Feasibility study of single-axis microrobot for endodontic treatment,” Ph.D. dissertation, University of Cincinnati. College of Engineering and Applied Science, 2014. 16
- [19] J. Dong and S. Y. Hong, “Design of z axis actuator and quick tool change assembly for an endodontic micro robot,” in *ASME International Mechanical Engineering Congress and Exposition*, vol. 44472, 2010, pp. 507–511. 16, 19
- [20] M.-K. Wu, D. Barkis, A. Roris, and P. Wesselink, “Does the first file to bind correspond to the diameter of the canal in the apical region?” *International Endodontic Journal*, vol. 35, no. 3, pp. 264–267, 2002. 21

- [21] J. Agrawal, P. K. Shenai, L. Chatra, P. Y. Kumar *et al.*, “Evaluation of normal range of mouth opening using three finger index: South india perspective study,” *Indian Journal of Dental Research*, vol. 26, no. 4, p. 361, 2015. 21
- [22] “Meca500, mecademic,” 2021, <https://www.mecademic.com/>. 22
- [23] “Mini40, ati industrial automation, inc.” 2021, <https://www.ati-ia.com/index.aspx>. 23, 79
- [24] C. Yang, J. Wang, L. Mi, X. Liu, Y. Xia, Y. Li, S. Ma, and Q. Teng, “A four-point measurement model for evaluating the pose of industrial robot and its influence factor analysis,” *Industrial Robot: An International Journal*, 2017. 35
- [25] T. Tang, H. Lin, Yu Zhao, Wenjie Chen, and M. Tomizuka, “Autonomous alignment of peg and hole by force/torque measurement for robotic assembly,” in *2016 IEEE International Conference on Automation Science and Engineering (CASE)*, 2016, pp. 162–167. 42
- [26] P. Zou, Q. Zhu, J. Wu, and J. Jin, “An approach for peg-in-hole assembling based on force feedback control,” in *2019 Chinese Automation Congress (CAC)*, 2019, pp. 3269–3273. 43
- [27] C. Boessler, F. Paque, and O. A. Peters, “The effect of electropolishing on torque and force during simulated root canal preparation with protaper

shaping files,” *Journal of Endodontics*, vol. 35, no. 1, pp. 102–106, 2009. 69,

72

[28] “Motion capture system - impulse x2e, phasespace,” 2021, [https://www.](https://www.phasespace.com/)

[phasespace.com/](https://www.phasespace.com/). 81